JETP Letters, Vol. 71, No. 2, 2000, pp. 43–47. Translated from Pis'ma v Zhurnal Éksperimental'noĭ i Teoreticheskoĭ Fiziki, Vol. 71, No. 2, 2000, pp. 65–70.

SU(2) Gluodynamics above the Deconfinement Temperature

N. O. Agasian

Institute of Theoretical and Experimental Physics, Bol'shaya Cheremushkinskaya ul. 25, Moscow, 117218 Russia

e-mail: agasyan@heron.itep.ru

Received December 14, 1999

Abstract—A physical model for describing *SU*(2) gluodynamics above the deconfinement temperature is developed on the basis of the operator-product-expansion method. The properties of the nonperturbative vacuum are parametrized in terms of gauge-invariant gluomagnetic correlation functions. The free energy of the system is calculated for $T > T_c$. The results obtained within the proposed model for the thermal properties of gluons (energy density, nonideality) are shown to agree with data coming from lattice calculations. © *2000 MAIK "Nauka/Interperiodica"*.

PACS numbers: 12.38.Lg; 11.10.Wx

1. The thermodynamics of quarks and gluons for $T > T_c$ (that is, in the deconfined phase) is the subject of intensive lattice investigations [1, 2]. Here, a calculation of thermodynamic quantities well defined on a lattice—such as the pressure p, the energy density ε, and the nonideality $\Delta(T) = (\varepsilon - 3p)/T^4$—as functions of temperature T is a conventional method of analysis. In recent years, the use of new supercomputers and improvements in computational codes have enabled a calculation of thermodynamic parameters like T_c and $\Delta(T_c)$ and of quantities like $p(T)$, $\varepsilon(T)$, and $\Delta(T)$ to within a few percent. At the same time, a consistent theoretical model that could describe existing data, on one hand, and provide deeper insights into phenomena occurring in the deconfined phase, on the other hand, has yet to be developed.

At temperatures below the critical point, $T < T_c$, the dynamics of the system is essentially nonperturbative and is characterized by confinement and a spontaneous breakdown of chiral invariance. Microscopically, this can be described by strong chromoelectric and chromomagnetic fields in a vacuum, which contribute to a nonperturbative shift of the free energy through the anomaly in the trace of the energy–momentum tensor [3]. Nonperturbative fields can be parametrized in terms of gluon condensates, as is done in QCD sum rules [3]. A more detailed picture emerges from the method of vacuum correlation functions [4], which describes the properties of the nonperturbative vacuum by using gauge-invariant correlation functions of the electric and magnetic types [5–7]. At temperatures above the critical point, $T > T_c$, the situation changes drastically (there is no color confinement there, and chiral symmetry is restored), but the nonperturbative effect of gluon fields on the dynamics of the system is of fundamental importance in this case as well. It was shown in [5–7] that, in the deconfined phase, a large piece of the chromoelectric correlation function vanishes; at the same time, the chromomagnetic condensate survives, changing only slightly with increasing temperature {the scale of this dependence is related to the dilaton mass of $M(0^{++}) = (1.6–1.8)$ GeV, which suppresses severely thermal excitations of gluons through the Boltzmann factor $\exp[-M(0^{++})T]$}. By taking into account the presence of nonzero vacuum correlations of the magnetic field, Simonov [7] was able to explain the area law for spatial Wilson loops, which was observed in lattice calculations [8]. The behavior of correlation functions of the electric and magnetic types in the two temperature phases that was described theoretically in [5–7] and which was confirmed by lattice calculations in [9] is commonly accepted at present.

In this study, a physical model for describing the properties of *SU*(2) gluodynamics above the deconfinement temperature is proposed on the basis of the operator-product-expansion (OPE) method. The quantities $\varepsilon(T)/T^4$ and $\Delta(T)$ as computed within this model are compared with lattice data. Nonperturbative dynamics at temperatures above the critical point, $T > T_c$, is associated with the gluon sector of QCD; in investigating the physics behind phenomena like strong deviations of the properties of the system from those of an ideal gas—this was observed in lattice experiments at temperatures between T_c and $(2–3)T_c$—it is therefore natural to address first the *SU*(2) model.

2. Let us represent the gluon field A_μ in the form

$$A_\mu = B_\mu + a_\mu, \tag{1}$$

where B_μ is a nonperturbative background field, while a_μ is the field of quantum fluctuations. By using the

t'Hooft identity, we can then write the partition function of $SU(2)$ gluodynamics as

$$\begin{aligned} Z &= \int [DA_\mu] e^{-S[A]} \\ &= \frac{1}{N}\int [DB_\mu]\eta(B)\int [Da_\mu]\exp(-S[B+a]), \end{aligned} \tag{2}$$

where $S(A)$ is the Euclidean action functional, $\eta(B)$ is a statistical weight fixing correlation functions for the fields B, and $N = \int [DB_\mu]\eta(B)$ is a normalization factor. For $T > 0$, the fields in question satisfy the periodic boundary conditions

$$\begin{aligned} B_\mu(\mathbf{x}, x_4) &= B_\mu(\mathbf{x}, x_4 + n\beta), \\ a_\mu(\mathbf{x}, x_4) &= a_\mu(\mathbf{x}, x_4 + n\beta), \end{aligned} \tag{3}$$

where $\beta = 1/T$ and $n = 0, \pm 1, \ldots$. The partition function (2) can be recast into the form

$$Z(V, T) = \langle Z(V, T, B)\rangle, \tag{4}$$

where angular brackets denote the eventual averaging of thermodynamic quantities over the ensemble of the fields B and

$$\begin{aligned} Z(V, T, B) &= \exp\{-V\beta F(T, B)\} \\ &= \int [Da_\mu^a][D\bar{\chi}][D\chi]\exp\left\{-\int_0^\beta dx_4 \int_V d^3x L(B, a, \bar{\chi}, \chi)\right\} \end{aligned} \tag{5}$$

with

$$L = \frac{1}{4g^2}(G_{\mu\nu}^a)^2 + \frac{1}{2\alpha}(D_\mu^{ab}a_\mu^b)^2 + \bar{\chi}^a(D^2)^{ab}\chi^b,$$

Here,

$$D_\mu^{ab} = \delta^{ab}\partial_\mu - \varepsilon^{abc}B_\mu^c$$

is a covariant derivative, $\bar{\chi}$ and χ are ghost fields, and $(D^2)^{ab} = D_\mu^{ac}D_\mu^{cb}$. Quantum fluctuations a_μ against the background of the gluomagnetic vacuum lead to nontrivial dynamics in the $T > T_c$ phase even if these fluctuations are taken into account in the one-loop approximation. In the following, we remove the divergent perturbative contribution from the partition function. By choosing the Feynman gauge ($\alpha = 1$) and performing integration with respect to the fields a_μ, $\bar{\chi}$, and χ, we can represent the free energy in the form

$$F_{\text{reg}}(T, B) = F_0(B) + F_g(T, B), \tag{6}$$

where

$$F_g(T, B) = \frac{1}{2}\ln(\det{}_\beta W)_{\text{reg}}, \tag{7}$$

$$W_{\mu\nu}^{ab} = -(D^2)^{ab}\delta_{\mu\nu} - 2G_{\mu\nu}^a(B)\varepsilon^{acb}. \tag{8}$$

For $T > T_c$, the nonperturbative vacuum is parametrized in terms of the gauge-invariant magnetic-type correlation functions

$$H_{ij\ldots k}(x_1\ldots x_k) = \langle \mathrm{tr}H_i(x_1)\Phi(x_1, x_2)H_j(x_2)\ldots\Phi(x_{k-1}, x_k)H_k(x_k)\Phi(x_k, x_1)\rangle, \tag{9}$$

where

$$H_i = \frac{1}{2}\varepsilon_{inm}t^aG_{nm}^a, \quad \mathrm{tr}t^at^b = \frac{1}{2}\delta^{ab},$$

and

$$\Phi(x, y) = \mathrm{P}\exp\left\{i\int_y^x B_\mu(z)dz_\mu\right\}$$

is the parallel transporter.

A bilocal correlation function of the form [7]

$$\begin{aligned} &\langle \mathrm{tr}H_i(x)\Phi(x, y)H_j(y)\Phi(y, x)\rangle \\ &= \frac{1}{2}\delta_{ij}\langle (H_k^a)^2\rangle D^H(x-y) + O(D_1) \end{aligned} \tag{10}$$

is an important ingredient of our analysis. For the function D^H, an expression that is consistent with lattice data from [9] is taken in the form[1]

$$D^H(x-y) = e^{-|x-y|/\lambda}. \tag{11}$$

At $T = 0$, we have $\langle (E_n^a)^2\rangle = \langle (H_n^a)^2\rangle$ in the vacuum; considering that the electric condensate component virtually vanishes in the deconfined phase, we then arrive at

$$H^2 = \langle (H_i^a)^2\rangle = \frac{1}{2}\langle (G_{nm}^a)^2\rangle = \frac{1}{4}\langle G^2\rangle, \tag{12}$$

where $\langle G^2\rangle \equiv \langle (G_{\mu\nu}^a)^2\rangle$ is the gluon condensate at $T = 0$.

3. A nonperturbative field is characterized by two dimensional quantities, an amplitude H and a scale λ at which it changes sizably (correlation length). At the

[1] In the literature, it is common practice to introduce the notation T_g instead of λ. Here, we employ the symbol λ in order to avoid confusion with temperature T.

same time, the character of the particle (gluon) trajectory in a field is determined by the radius of curvature of this trajectory; in a magnetic field, this is the Larmor radius $R = 1/\sqrt{H}$. Thus, there arises the dimensionless parameter $\xi = (\sqrt{H}\lambda)^{-1}$, which can be used to study the properties of the system in various extreme cases.

In the case of $\xi \gg 1$, which corresponds to $\lambda \longrightarrow 0$ ($\langle G^2 \rangle$ = const), it follows from (10) and (11) that the fields $H_i^a(x)$ are uncorrelated—that is, the vacuum represents a quantum ensemble of stochastic fields. In the large-N_c limit of gluodynamics, nonperturbative effects in the stochastic vacuum of the deconfined phase were studied by Dosch *et al.* [10].

For $\xi \ll 1$, the free energy can be computed by the OPE method. In the case of $R \ll \lambda$, even a sharply varying field H can be treated as a uniform one, provided that we are interested in distances commensurate with the characteristic scale of the particle trajectory, $R = 1/\sqrt{H}$. Within the conventional OPE, this corresponds to extremely high characteristic momenta Q [$(Q^2 \sim H = 1/(\xi\lambda)^2 \longrightarrow \infty$]. For a Gaussian parametrization of the function $D^H(x)$, $D^H(x) = \exp\{-x^2/\lambda^2\}$ (it is important that D^H be a decreasing function at a scale of λ), a power-series expansion in terms of Matsubara frequencies $\omega_n = 2\pi nT$ has the form

$$D^H(T, r) = \frac{\lambda T}{\sqrt{2}} D^H(r) \sum_{n=-\infty}^{+\infty} \exp\left\{-\frac{n^2}{\xi^2}\left(\frac{\pi T}{\sqrt{H}}\right)^2\right\}. \quad (13)$$

Thus, we can see that, for $T > T_c$ {in *SU*(2) gluodynamics, we have $T_c \simeq 0.29$ GeV [11]} and $\xi \ll 1$ (the condition that ensures the applicability of the OPE), the main contribution to the correlation function (10) comes from the zero-frequency component ($\omega_0 = 0$)—that is, the nonperturbative field can be treated as a constant field. Therefore, the limit of a constant uniform magnetic condensate appears to be the zero-order approximation of the OPE for thermodynamic quantities in the deconfined phase.

In accordance with (10), all the directions of the field H_i^a are equiprobable both in coordinate and in color space; taking this into account, we choose the vector potential in the form $B_\mu^a = \delta^{a3}\delta_{\mu_1} H x_2$, which corresponds to the magnetic field H_z^3. The state that arises in the lowest order of the OPE is described by the magnetic field $H_z^3 = H$ and the gluons $a_\mu^\pm = a_\mu^1 \pm i a_\mu^2$ interacting with it. In a magnetic field H, a charged massless vector particle has the spectrum (Landau levels)

$$\omega_s^2(q_z^2, n, \sigma, H) = q_z^2 + H(2n + 1 + 2\sigma), \quad (14)$$

where $n = 0, 1, \ldots$ is the orbital quantum number, while $\sigma = \pm 1$ is the spin projection onto the z axis. Technically, a transition for the free energy $F_g = (1/2)\mathrm{Tr}\ln(q_4^2 + \omega_0^2(\mathbf{q}))$ from the vacuum case ($H = 0$, $T = 0$) to the case of $H \neq 0$ and $T \neq 0$ is straightforward. Omitting the details of the calculations, we note that, eventually, this transition reduces to the substitutions $q_4 \longrightarrow \omega_k = 2\pi kT$ ($k = 0, \pm 1, \ldots$); $\omega_0^2 = \mathbf{q}^2 \longrightarrow \omega_s^2$; and

$$\mathrm{Tr} \longrightarrow \frac{HT}{2\pi} \sum_{n=0}^{\infty} \sum_{\sigma=\pm 1} \sum_{k=-\infty}^{+\infty} \int_{-\infty}^{+\infty} \frac{dq_z}{2\pi}, \quad (15)$$

where the degeneracy multiplicity of $H/2\pi$ has been taken into account for the Landau levels. Performing summation over Matsubara frequencies, we obtain

$$F_g(T, H) = \frac{HT}{\pi^2} \sum_{n=0}^{\infty} \sum_{\sigma=\pm 1} \int_0^{\infty} dq_z \ln(1 - e^{-\omega_s/T}) + O(\xi), \quad (16)$$

where $O(\xi)$ stands for higher order OPE terms in ξ. The term for the regularized T-independent part $F_0(H)$ of the free energy reduces to the one-loop expression for the density of the magnetic-condensate energy; for the thermodynamics of the system being considered, this term is immaterial.

As is well known, a massless vector particle in a magnetic field has a tachyon mode corresponding to the level $\omega_s^2(q_z = 0, n = 0, \sigma = -1) = -H$. This mode is due exclusively to the effect of a uniform field. Within the model used here, the magnetic condensate is obviously nonuniform at a scale of about λ, so that no tachyon arises in the physical spectrum.

4. A quantum-mechanical analysis of the motion of a particle in a magnetic field H reveals that the distribution of the probability density with respect to the transverse radius ρ (distance from the z axis) peaks at $\rho = \bar{\rho} = R\sqrt{2n+1}$. In the case of $n \gg 1$, we have $\Delta\rho \equiv \sqrt{\overline{\rho^2} - \bar{\rho}^2} \simeq R/\sqrt{2} \ll \bar{\rho}$. Thus, the region where a particle can be found with a sizable probability represents a narrow ring of radius R and width about R. In the sum over n in (16), we can therefore retain only the lowest Landau levels. From the point of view of thermodynamics, the contribution to the free energy from Landau levels characterized by large values of the orbital quantum number n is suppressed by the factor $\exp\{-\sqrt{2nH}/T\}$. A numerical calculation shows that, in the interval $T_c < T < 2T_c$, the main contribution to the free energy comes from the ($n = 0$, $\sigma = 1$), ($n = 1$, $\sigma = -1$), and ($n = 2$, $\sigma = -1$) levels. Since the condensate is nonuniform, integration with respect to x must be performed

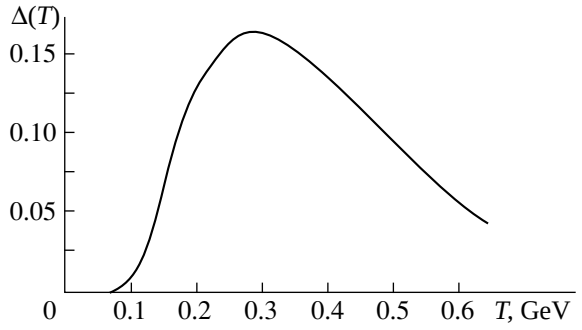

Nonideality $\Delta(T)$ at $\langle G^2\rangle = 4.3$ GeV^4.

up to ξ [the integral in (16) is cut off at $q_z = 1/\lambda$, where the field H begins to change significantly]. Taking all the above into account, we can recast the free energy into the form

$$F_g(T, H) \tag{17}$$
$$= \frac{H^{3/2}T}{\pi^2}\left[\int_0^\xi dx f(1+x^2) + 2\sum_{n=0}^{\infty}\int_0^\xi dx\, f(x^2+2n+3)\right],$$
$$f(x) = \ln[1 - \exp(-(\sqrt{H}/T)\sqrt{x})].$$

Eventually, physical quantities must be averaged over nonperturbative fields. As a matter of fact, this is averaging over the quantum statistical ensemble of the fields H_i^a. In that order of the expansion in ξ which is considered here, the averaging over the ensemble amounts to multiplying the averaged quantity by the statistical weight, which is equal to the number of available quantum states of the field H_i^a. Considering that different directions of this field are equiprobable both in coordinate and in color space, we find that the statistical weight is $\int [DB_\mu]\eta(B) = \left(\prod_{i=x,y,z} 1\right)\left(\prod_{a=1,2,3} 1\right) = 9$. It is canceled by the identical normalization factor N appearing in the denominator on the right-hand side of (2). It should be noted that this is so only in the lowest order of the OPE—higher order terms of the expansion in ξ, which are denoted by $O(\xi)$ in (15), do not obey this simple rule.

Knowing the free energy—or, what is the same, the pressure (which is given by $p = -F$)—as a function of T, we can find the nonideality $\Delta = (\varepsilon - 3p)/T^4$, where the energy density is $\varepsilon = Tdp/dT - p$. Lattice calculations show that, for $T > T_c$, gluons do not obey the ideal-gas equations $p = p_{SB} = 2(N_c^2 - 1)\pi^2T^4/90$, $\varepsilon = 3p$, and $\Delta = 0$; in the interval $T_c < T < (2\text{–}3)T_c$, they behave as a strongly nonideal system with $\Delta \neq 0$. Setting $\langle G^2\rangle = 4.3$ GeV^4 [12], we have calculated numerically the nonideality $\Delta(T)$ within the proposed model. The results are shown in the figure. It can be seen that Δ peaks at $T_* \simeq 300$ MeV. According to lattice calculations, the critical temperature is $T_c \simeq 290$ MeV [11]. For $\varepsilon(T_c)/T_c^4$, the lattice data from [11] at $T_c = 0.29$ GeV yield 0.256 ± 0.023. Our analysis of nonperturbative $SU(2)$ gluodynamics within the OPE leads to $\varepsilon(T_*)/T_*^4 = 0.42$.

5. Thus, the model proposed here for $SU(2)$ gluodynamics provides a correct physical pattern of the nonideality of thermal gluons above the deconfinement temperature. Moreover, not only does this approach enable us to describe qualitatively the behavior of the nonperturbative vacuum with increasing T, but it also furnishes quantitative information about the thermodynamics of the system. The method developed here features the dimensional parameter H, which specifies the scale of thermodynamic quantities and the dimensionless parameter $\xi = (\lambda\sqrt{H})^{-1}$ of the OPE. The thermodynamic functions resulting from the numerical calculations change only slightly with the condensate value $\langle G^2\rangle$. In principle, thermodynamic potentials may change more sizably upon taking into account higher order terms of the OPE.

Lattice data from [12] yield the values of $\lambda \simeq 0.2$ fm and $\langle G^2\rangle \simeq 4.3$ GeV^4, whence we obtain $\xi \simeq 1$. At the same time, the OPE approach is valid for $\xi \ll 1$. In this connection, it should be emphasized that, for a nonperturbative vacuum, we have constructed a physical model that provides a correct description of the deconfined phase near the boundary of the OPE applicability range. In using QCD sum rules, which follow from the OPE of correlation functions for physical currents, the situation is similar: relations found at high momentum transfers ($Q^2 \gg 1$ GeV^2) are applied down to values of $Q^2 \sim (0.7\text{–}0.9)^2$ GeV, and the resulting description of hadronic resonances is quite reasonable.

ACKNOWLEDGMENTS

I am grateful to Yu. A. Simonov for interest in this study, enlightening comments, and discussion of the results presented here.

REFERENCES

1. A. Di Giacomo, hep-lat/9912016.
2. F. Karsch, hep-lat/9909006.
3. M. A. Shifman, A. I. Vainshtein, and V. I. Zakharov, Nucl. Phys. B **147**, 385, 448, 519 (1979).
4. H. G. Dosch, Phys. Lett. B **190**, 177 (1987); H. G. Dosch and Yu. A. Simonov, Phys. Lett. B **205**, 339 (1988); Yu. A. Simonov, Nucl. Phys. B **324**, 67 (1989).

5. Yu. A. Simonov, Pis'ma Zh. Éksp. Teor. Fiz. **55**, 605 (1992) [JETP Lett. **55**, 627 (1992)].
6. Yu. A. Simonov, Yad. Fiz. **58**, 357 (1995) [Phys. At. Nucl. **58**, 309 (1995)].
7. Yu. A. Simonov, Hot Nonperturbative QCD, in *Lectures at the Enrico Fermi International School in Physics*, Varena, 1995.
8. E. Manousakis and J. Polonyi, Phys. Rev. Lett. **58**, 847 (1987); G. S. Bali, J. Fingberg, U. M. Heller, *et al.*, Phys. Rev. Lett. **71**, 3059 (1993).
9. A. Di Giacomo, E. Meggiolaro, and H. Panagopoulos, hep-lat/960301; Nucl. Phys. B **483**, 371 (1997).
10. H. G. Dosch, H. J. Pirner, and Yu. A. Simonov, Phys. Lett. B **349**, 335 (1995).
11. J. Engels, F. Karsch, and K. Redlich, Nucl. Phys. B **435**, 295 (1995).
12. M. Campostrini, A. Di Giacomo, and G. Mussardo, Z. Phys. C **25**, 173 (1984).

Translated by A. Isaakyan

JETP Letters, Vol. 71, No. 2, 2000, pp. 48–52. Translated from Pis'ma v Zhurnal Éksperimental'noĭ i Teoreticheskoĭ Fiziki, Vol. 71, No. 2, 2000, pp. 71–77.

A New Representation of the Interaction between an Atom and an Intense Elliptically Polarized Electromagnetic Field

L. P. Rapoport and A. S. Kornev*

Voronezh State University, Voronezh, 394693 Russia
**e-mail: kornev@tooth.vsu.ru*

Received December 8, 1999

Abstract—A new representation of the interaction between a laser field and an atom is obtained. The Fourier component of the interaction is represented as a multipole expansion dependent on the force parameter of the field, $a_0 = F/\omega^2$, and the degree of its ellipticity, η. This representation provides the analytical separation of the angles in the time-dependent Schrödinger equation. The stationary spherically symmetric part of the potential $V_0(r, a_0, \eta)$ of a "field-dressed" atom is singled out. The application of the new representation to the calculation of nonlinear effects and electron scattering by an atom in a field are discussed.© *2000 MAIK "Nauka/Interperiodica".*

PACS numbers: 32.80.-t; 42.65.-k

Recently, the interaction between an atom and a superintense monochromatic electromagnetic field described by the time-dependent vector–potential $\mathbf{A}(t)$ (the dipole approximation) has been considered with the invocation of the Kramers method [1]. The method is based on the unitary time-dependent transformation of the Hamiltonian of an atom in a coordinate system oscillating with the field frequency. Introducing the vector $\mathbf{a}(t)$ related to $\mathbf{A}(t)$ as

$$\mathbf{a}(t) = c^{-1}\int^{t}\mathbf{A}(t')dt',$$

we can see that this transformation reduces to the change of the coordinate $\mathbf{r}$ of an electron in the laboratory coordinate system for the coordinate $(\mathbf{r} - \mathbf{a}(t))$. In the atomic system of units ($\hbar = e = m = 1$), the Hamiltonian of a hydrogen-like atom with the nucleus charge Z takes the form

$$\hat{H}_{vib} = -\frac{1}{2}\nabla^2 - \frac{Z}{|\mathbf{r} - \mathbf{a}(t)|}. \quad (1)$$

In general, the field polarization in $\mathbf{a}(t)$ can be of any type, and therefore the variables of the time-dependent Schrödinger equation with Hamiltonian (1) cannot be separated. For a linearly polarized radiation, this equation is usually integrated numerically without separation of the variables [2]. An intense field with an arbitrary elliptical polarization has not been studied as yet. In the particular case of the circular polarization, we have

$$\mathbf{a}(t) = \frac{a_0}{\sqrt{2}}(\mathbf{e}_x\cos\omega t - \eta\mathbf{e}_y\sin\omega t), \quad (2)$$

where $a_0 = F/\omega^2$, F is the field amplitude, ω is the field frequency, and $\eta = \pm 1$ for the left (right) wave polarization. It was shown [3] that the potential in equation (1) with $\mathbf{a}(t)$ in form (2) can be written as a multipole expansion. Indeed, one can see from (2) that $|\mathbf{a}(t)| = a_0/\sqrt{2}$ and $\cos(\hat{\mathbf{r}}, \hat{\mathbf{a}}(t)) = \cos(\varphi + \eta\omega t)$ (hereafter, we use the notation $\hat{\boldsymbol{\alpha}} \equiv \boldsymbol{\alpha}/|\boldsymbol{\alpha}|$). Taking into account that the potential in (1) is a generating function for Legendre polynomials, we obtain its expansion in terms of the spherical functions $Y_{LM}(\hat{\mathbf{r}})$ and $Y_{LM}(\mathbf{e}_x)$:

$$|\mathbf{r} - \mathbf{a}(t)|^{-1} = \sum_{L=0}^{\infty}\sum_{M=-L}^{L}\frac{4\pi}{2L+1} \times \xi_L(r, a_0)Y_{LM}(\hat{\mathbf{r}})Y^*_{LM}(\mathbf{e}_x)e^{i\eta M\omega t}, \quad (3)$$

where $\xi_L(r, a_0) = r_<^L/r_>^{L+1}$, $r_< = \min(r, a_0/\sqrt{2})$, and $r_> = \max(r, a_0/\sqrt{2})$.

Considering the nonstationary Schrödinger equation with potential (3),

$$i\frac{\partial\Psi(\mathbf{r}, t)}{\partial t} = \left\{-\frac{1}{2}\nabla^2 - \frac{Z}{|\mathbf{r} - \mathbf{a}(t)|}\right\}\Psi(\mathbf{r}, t),$$

one can separate the angular parts by projecting the potential onto $Y_{LM}(\hat{\mathbf{r}})$ and then reducing it to the one-dimensional system of equations for quasienergies. The application of (3) to the problem of electron scattering in a field was considered in [4]. However, the multipole expansion (3) can be obtained by this method only for a circularly polarized field, because, in the general case

of the elliptically polarized field, $|\mathbf{a}(t)|$ is time-dependent.

In the present study, we aimed to obtain the multipole expansion for an elliptically polarized field.

Below, we use the multipole expansion $|\mathbf{r}_1 - \mathbf{r}_2|^{-1}$, in which r_1 and r_2 are used not as $r_<^L / r_>^{L+1}$, but in the symmetrized form [5]:

$$|\mathbf{r}_1 - \mathbf{r}_2|^{-1} = \sum_{L=0}^{\infty} \sum_{M=-L}^{L} \frac{4\pi}{2L+1} f_L(r_1, r_2) Y_{LM}(\hat{\mathbf{r}}_1) Y_{LM}^*(\hat{\mathbf{r}}_2), \quad (4)$$

where

$$f_L(r_1, r_2) = \frac{(r_1 r_2)^L}{(r_1^2 + r_2^2)^{L+1/2}} \times {}_2F_1\left(\frac{L}{2} + \frac{1}{4}, \frac{L}{2} + \frac{3}{4}; L + \frac{3}{2}; \left(\frac{2r_1 r_2}{r_1^2 + r_2^2}\right)^2\right), \quad (5)$$

and ${}_2F_1$ is the hypergeometric function. In this case, we can put $\mathbf{r}_1 \equiv \mathbf{r}$ and $\mathbf{r}_2 \equiv \mathbf{a}(t)$. Introduce into consideration the wave vector of photons, $\mathbf{k} = \mathbf{n}\omega/c$, and align the z-axis in the direction of $\mathbf{k}$, i.e., assume that $\mathbf{e}_z = \mathbf{n}$.

In the general case of an elliptically polarized field, we have

$$\mathbf{a}(t) = \frac{a_0}{\sqrt{1+\eta^2}} (\mathbf{e}_x \cos\omega t - \eta \mathbf{e}_y \sin\omega t); \quad -1 \le \eta \le 1. \quad (6)$$

The parameter η determines the degree of the linear, $l = (1 - \eta^2)/(1 + \eta^2)$, and circular, $A_C = 2\eta/(1 + \eta^2)$, polarizations. It is seen from (6) that the amplitudes obey the inequality $|a_{x0}| \neq |a_{y0}|$. Rotating the coordinate axes with the aid of $D_{MM'}^{(L)}$, using the Wigner (α, β, γ)-functions, and choosing the angle of rotation β about the axis $\mathbf{e}_y = \mathbf{e}'_y$ in such a way that the amplitudes would obey the relationship $|a'_{x0}| = |a'_{y0}|$ in the new coordinates, we arrive at a new coordinate system $(\mathbf{e}'_x, \mathbf{e}'_y, \mathbf{e}'_z)$. Assuming that $\beta = \arcsin(1 - \eta^2)^{1/2}$ for $0 \le \beta \le \pi/2$, we can transform (4) and (6) to the new coordinate system. Taking into account that the scalar product of the spherical functions in (4) is not changed, we obtain

$$\sum_M Y_{LM}(\hat{\mathbf{r}}) Y_{LM}^*(\hat{\mathbf{a}}(t)) = \sum_M Y_{LM}(\hat{\mathbf{r}}') Y_{LM}^*(\hat{\mathbf{a}}'(t)).$$

The transformation

$$a'_{m'}(t) = \sum_m D_{mm'}^{(1)}(0, \beta, 0) a_m(t),$$

where $m, m' = 0, \pm 1$, and $a_m(t)$ and $a'_{m'}(t)$ are the cyclic components of the $\mathbf{a}(t)$ vector in the initial and the rotated coordinate systems, respectively, yields

$$a(t) = \frac{a_0}{\sqrt{1+\eta^2}} \times \left\{ (\sqrt{1-\eta^2}\,\mathbf{e}'_z + |\eta|\,\mathbf{e}'_x)\cos\omega t - \eta \mathbf{e}'_y \sin\omega t \right\};$$

$$Y_{LM}^*(\hat{\mathbf{a}}'(t)) = Y_{LM}^*(\theta'_a, \varphi'_a) = \sqrt{\frac{2L+1}{4\pi}\frac{(L-M)!}{(L+M)!}} P_L^M(\cos\theta'_a) e^{iM\varphi'_a},$$

where $P_L^M(x)$ is the associated Legendre polynomial;

$$\cos\theta'_a = \frac{\sqrt{1-\eta^2}\cos\omega t}{\sqrt{\eta^2 + (1-\eta^2)\cos^2\omega t}}; \quad \varphi'_a = \operatorname{sign}\eta\, \omega t'; \quad a^2(t) = \frac{a_0^2}{1+\eta^2}[\eta^2 + (1-\eta^2)\cos^2\omega t]. \quad (7)$$

In the new coordinate system, expansion (4) takes the form

$$|\mathbf{r} - \mathbf{a}(t)|^{-1} = \sum_{L=0}^{\infty} \sum_{M=-L}^{L} \sqrt{\frac{4\pi}{2L+1}} \mathcal{F}_{LM}(r, a_0, \eta, \omega t) \times Y_{LM}(\hat{\mathbf{r}}') e^{i \operatorname{sign}\eta M \omega t},$$

where

$$\mathcal{F}_{LM}(r, a_0, \eta, \omega t) = F(\cos^2\omega t) \times P_L^M\left(\frac{\sqrt{1-\eta^2}\cos\omega t}{\sqrt{\eta^2 + (1-\eta^2)\cos^2\omega t}}\right);$$

$$F(\cos^2\omega t) \equiv \sqrt{\frac{(L-M)!}{(L+M)!}} f_L(r, a(t)).$$

Now, expand $\mathcal{F}_{LM}(r, a_0, \eta, \omega t)$ into a Fourier series

$$\mathcal{F}_{LM}(r, a_0, \eta, \omega t) e^{i \operatorname{sign}\eta M \omega t} = \sum_{N=-\infty}^{\infty} \tilde{f}_N(LM; r, a_0, \eta) e^{i(N + \operatorname{sign}\eta M)\omega t}.$$

The coefficients of this expansion are

$$\tilde{f}_N(LM; r, a_0, \eta) = \frac{1}{2\pi} \int_0^{2\pi} \mathcal{F}_{LM}(r, a_0, \eta, \alpha) e^{-iN\alpha} d\alpha.$$

Representing $\cos N\alpha$ in the form

$$\cos N\alpha = \sum_{k=|N| \bmod 2}^{|N|}{}' b_k^{(|N|)} \cos^k \alpha,$$

where

$$b_k^{(n)} = \begin{cases} 2^{k-1}\dfrac{2n}{n-k}(-1)^{(n-k)/2}\dbinom{\frac{n+k}{2}-1}{\frac{n-k}{2}-1}, & k<n; \\ 2^{n-1}(1+\delta_{n0}), & k=n \end{cases}$$

(see formula (1.331.3) in [6]) and taking into account that the prime at the symbol Σ indicates the summation either over even or over odd k (depending on N), we arrive at the Nth Fourier component, $\tilde{f}_N$, in the form

$$\tilde{f}_N(LM; r, a_0, \eta) = \frac{1}{2\pi}\sum_{k=|N|\bmod 2}^{|N|} b_k^{(|N|)}\int_0^{2\pi} F(\cos^2\alpha) \times P_L^M\left(\frac{\sqrt{1-\eta^2}\cos\alpha}{\sqrt{\eta^2+(1-\eta^2)\cos^2\alpha}}\right)\cos^k\alpha\, d\alpha. \quad (8)$$

Formula (8) can be reduced to

$$\tilde{f}_N(LM; r, a_0, \eta) = \begin{cases} \sum\limits_{k=|N|\bmod 2}^{|N|}{}' b_k^{(|N|)} G_{LM}(k, \eta), & \text{if } L+M+N \text{ is even} \\ 0, & \text{if } L+M+N \text{ is odd,} \end{cases}$$

where

$$G_{LM}(k, \eta) = \frac{2}{\pi}\int_0^1 F(x^2) P_L^M\left(\frac{\sqrt{1-\eta^2}x}{\sqrt{\eta^2+(1-\eta^2)x^2}}\right)\frac{x^k dx}{\sqrt{1-x^2}}.$$

One can show that

$$\int_0^{2\pi}(\ldots)\sin(N\alpha)\, d\alpha = 0.$$

Finally, we obtain the following Fourier multipole expansion for $|\mathbf{r}-\mathbf{a}(t)|^{-1}$:

$$|\mathbf{r}-\mathbf{a}(t)|^{-1} = \sum_{N=-\infty}^{\infty}\sum_{L=0}^{\infty}\sum_{M=-L}^{L}\sqrt{\frac{4\pi}{2L+1}}\tilde{f}_N(LM; r, a_0, \eta) \times Y_{LM}(\hat{\mathbf{r}}')e^{i(N+\operatorname{sign}\eta M)\omega t}. \quad (9)$$

In the particular cases, we obtain the following relationships.

(1) For the linear polarization ($\eta = 0$):

$$\sqrt{\frac{2L+1}{4\pi}\frac{(L-M)!}{(L+M)!}}P_L^M(+1) = \delta_{M,0}\sqrt{\frac{2L+1}{4\pi}};$$

$$P_L^M(-1) = (-1)^L P_L^M(+1).$$

Thus, the terms with $M \neq 0$ in (9) are eliminated.

(2) For the circular polarization ($\eta = \pm 1$):

$$\sqrt{\frac{2L+1}{4\pi}\frac{(L-M)!}{(L+M)!}}P_L^M(0) = Y_{LM}(\mathbf{e}_x);$$

and $|\mathbf{a}(t)| = a_0/\sqrt{2}$ is time-independent. In this case, the terms with $N \neq 0$ in (9) are eliminated, and $f_L(r, a(t)) = r_<^L/r_>^{L+1}$; i.e., it coincides with (3).

If $N = 0$, the potential is time-independent (a field-dressed atom). If one also assumes that $L = M = 0$, it becomes possible to single out the spherically symmetric part of the potential of a field-dressed atom. In this case, one can write ${}_2F_1$ in (5) in terms of the elementary function (see formula (15.1.14) in [7]) as

$${}_2F_1\left(\frac{1}{4}, \frac{3}{4}; \frac{3}{2}; z\right) = \left(\frac{2}{1+\sqrt{1-z}}\right)^{1/2}.$$

Then, using the above form of ${}_2F_1$ at

$$z = \left(\frac{2ra(t)}{r^2+a^2(t)}\right)^2,$$

where $a(t)$ is given by (7), we can calculate $f_0(r, a(t))$. In order to determine the Fourier transform of $\tilde{f}_0$, one has to integrate $f_0(r, a(t))$ with respect to time. This results in the division of the analytical dependence of $\tilde{f}_0$ on r into three domains:

$$\text{(i)}\ \ r < \frac{|\eta|a_0}{\sqrt{1+\eta^2}};\ \ \text{(ii)}\ \ \frac{|\eta|a_0}{\sqrt{1+\eta^2}} < r < \frac{a_0}{\sqrt{1+\eta^2}};$$

$$\text{(iii)}\ \ r > \frac{a_0}{\sqrt{1+\eta^2}}.$$

Then,

$$V_0^{(e)}(r, a_0, \eta) = -Z\begin{cases} 2\sqrt{1+\eta^2}K(\sqrt{1-\eta^2})/(\pi a_0) & \text{for domain (i),} \\ 2g(r, a_0, \eta)/\pi & \text{for domain (ii),} \\ 1/r & \text{for domain (iii),} \end{cases} \quad (10)$$

where

$$g(r, a_0, \eta) = \frac{1}{r}\arcsin\sqrt{\frac{(1+\eta^2)r^2-\eta^2a_0^2}{a_0^2(1-\eta^2)}} + \frac{1}{a_0}\sqrt{1+\eta^2}F\left(\arccos\sqrt{\frac{(1+\eta^2)r^2-\eta^2a_0^2}{a_0^2(1-\eta^2)}}, \sqrt{1-\eta^2}\right);$$

and $K(m)$ and $F(\alpha, m)$ are the complete and the partial first-order elliptic integrals.

It is seen from (10) that the asymptotic behavior of $V_0^{(e)}(r \longrightarrow \infty, a_0, \eta)$ is of the Coulomb nature. In the

particular cases of the linear and circular polarizations, expressions (10) take the following forms.

(1) For the linear polarization ($\eta = 0$):

$$V_0^{(l)}(r, a_0) = -Z\begin{cases}\dfrac{2}{\pi}\dfrac{1}{r}\arcsin\left(\dfrac{r}{a_0}\right) + \dfrac{2}{\pi}\dfrac{1}{a_0}\ln\dfrac{a_0 + \sqrt{a_0^2 - r^2}}{a_0 - \sqrt{a_0^2 - r^2}}, & r < a_0; \\ 1/r, & r > a_0.\end{cases}$$

At $r \longrightarrow 0$, we arrive at the logarithmic singularity.

(2) For the circular polarization ($\eta = \pm 1$):

$$V_0^{(c)}(r, a_0) = -Z\begin{cases}\sqrt{2}/a_0, & r < a_0/\sqrt{2}; \\ 1/r, & r > a_0/\sqrt{2}.\end{cases}$$

The potential V_0 for different polarizations with $|\eta| = 0$, 0.5, 1 is shown in the figure.

In order to apply the above theory to the complex N-electron atoms, we use the following expression instead of the Hamiltonian:

$$\hat{H}_0^{(N)} = \sum_{k=1}^{N}\left\{-\frac{1}{2}\nabla_k^2 - V_{0k}^{(e)}(r, a_0, \eta)\right\} + \frac{1}{2}\sum_{k \neq q = 1}^{N}\frac{1}{|\mathbf{r}_k - \mathbf{r}_q|}.$$

The potential of the Coulomb interaction between the electrons for the Kramers transformation [1] is not changed and therefore can be constructed with the aid of $V_{0k}^{(e)}(r, a_0, \eta)$. This part of the Hamiltonian can be used to construct the Hartree–Fock equations, whose solutions determine the electron energy $\varepsilon_k(a_0, \eta)$ in a field-dressed atom and the one-particle wave function $\varphi_k(r, a_0, \eta)$. The complete time-dependent Hamiltonian also includes the part of (9) expanded into multipoles, in which one has to omit the terms with $N = L = M = 0$ (they are included into $V_{0k}^{(e)}$), i.e., to take $V_{Nk}^{(e)}(LM; r, a_0, \eta)$ with $|N| \geq 0$, $L > 0$, and $|M| \geq 0$. Using the basis Hartree–Fock functions of a field-dressed atom and assuming that $V_N^{(e)}$ is a "seeding" vertex, one can construct the equations for the effective vertex in the random-phase approximation with exchange (RPAE) and analytically separate the angular variables, as was made for the RPAE in a circularly polarized field in [3].

The problem of electron scattering by the Coulomb potential (in the general case, by an atom) in a strong elliptically polarized field by the method of strong channel coupling can be reduced to the one-dimensional system of coupled equations similar to those for the circularly polarized field considered in [4]. The solution of the Schrödinger equation in a vibrating coordinate system is sought in the form

$$\Psi(\mathbf{r}, t) = \sum_{nl'm'}\frac{1}{r}R_{nl'm'}(r)Y_{l'm'}(\hat{\mathbf{r}})e^{-i(E - n\omega)t}.$$

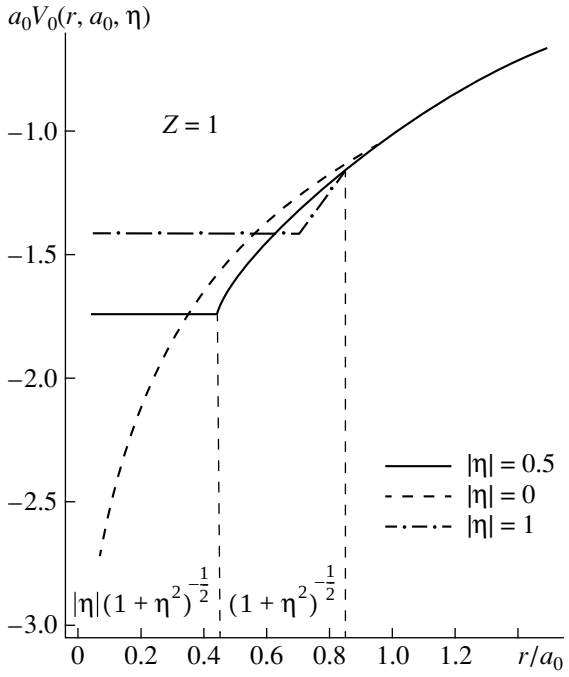

Stationary spherically symmetric part of the potential $V_0(r, a_0, \eta)$ as a function of r/a_0 for elliptically ($|\eta| = 0.5$), linearly ($\eta = 0$), and circularly polarized field ($|\eta| = 1$). At $r > a_0(1 + \eta^2)^{-1/2}$, the potential is of the Coulomb nature.

Projecting the Shrödinger equation onto the state $Y_{lm}(\hat{\mathbf{r}})$ and equating the terms with equal factors $e^{in\omega t}$, we obtain

$$\left\{\frac{d^2}{dr^2} - \frac{l(l+1)}{r^2} - 2V_0^{(e)}(r, a_0, \eta) + k_n^2\right\}R_{nlm}(r) = 2\sum_{n'l'm'}V_{nlm}^{n'l'm'}(r, a_0, \eta)R_{n'l'm'}(r),$$

where

$$V_{nlm}^{n'l'm'}(r, a_0, \eta) = -Z\sum_{N=-\infty}^{\infty}\sum_{L=1}^{\infty}\tilde{f}_N(L, m - m'; r, a_0, \eta) \times (-1)^m[(2l+1)(2l'+1)]^{1/2}\begin{pmatrix} l' & L & l \\ 0 & 0 & 0\end{pmatrix} \times \begin{pmatrix} l' & L & l \\ m' & m - m' & m\end{pmatrix}\delta_{n',\, n + (m - m')\mathrm{sign}\eta + N};$$

$$k_n^2 = 2(E - n\omega).$$

Obviously, the corresponding differential cross sections depend on $\mathrm{sgn}\eta$, i.e., on the photon helicity (elliptic dichroism). Elliptic dichroism in a field weak in terms of the perturbation theory was considered in [8].

ACKNOWLEDGMENTS

This study was supported by the Russian Foundation for Basic Research, project no. 00-02-1656.

REFERENCES

1. H. A. Kramers, *Quantum Mechanics* (North Holland, Amsterdam, 1956).
2. *Super-Intense Laser-Atom Physics IV (1995)*, Eds. by H.G. Müller and M.V. Fedorov (Kluwer Acad., Dordrecht, 1996).
3. L. P. Rapoport, Pis'ma Zh. Éksp. Teor. Fiz. **68**, 189 (1998) [JETP Lett. **68**, 198 (1998)].
4. L. P. Rapoport and A. S. Kornev, Zh. Éksp. Teor. Fiz. **116**, 1241 (1999) [JETP **89**, 664 (1999)].
5. R. A. Sack, J. Math. Phys. **37**, 215 (1957).
6. I. S. Gradshteĭn and I. M. Ryzhik, *Tables of Integrals, Sums, Series, and Products* (Nauka, Moscow, 1971).
7. M. Abramowitz and I. A. Stegun, *Handbook of Mathematical Functions* (Dover, New York, 1965).
8. N. L. Manakov, A. Maquet, S. I. Marmo, *et al.*, J. Phys. B **32**, 3747 (1999).

Translated by L. Man

JETP Letters, Vol. 71, No. 2, 2000, pp. 53–57. Translated from Pis'ma v Zhurnal Éksperimental'noĭ i Teoreticheskoĭ Fiziki, Vol. 71, No. 2, 2000, pp. 78–84.

PLASMA, GASES

Current Sheets in Magnetic Configurations with Singular X-Lines

S. Yu. Bogdanov, N. P. Kyrie, V. S. Markov, and A. G. Frank*

Institute of General Physics, Russian Academy of Sciences, ul. Vavilova 38, Moscow, 117942 Russia
**e-mail: annfrank@fpl.gpi.ru*

Received December 21, 1999

Abstract—The possibility of the formation of current sheets in 3D magnetic configurations with singular X-lines was studied experimentally. It is shown that a sheet can be formed in the presence of the longitudinal magnetic-field component directed along the X-line, in which case the longitudinal component can exceed the transverse component everywhere inside the plasma. Characteristic of the CS formation in 3D magnetic configurations with X-lines are an increase in the longitudinal magnetic-field component inside the sheet and a decrease in the plasma compression ratio as compared to 2D configurations with null-lines. If the longitudinal component exceeds a certain critical value, a sheet cannot be formed: instead of a sheet, there appear two sheaths separated by a cavity with a local minimum in the electron density. *© 2000 MAIK "Nauka/Interperiodica".*

PACS numbers: 52.30.-q

1. One of key points in the problem of magnetic reconnection is to answer the question of whether the formation of a current sheet (CS) is possible in one or another magnetic configuration. Indeed, magnetic reconnection can only occur in spatial regions such that magnetic field lines with different (in particular, opposite) directions approach each other. These regions are characterized by a high current density and small spatial scales. Thus, the effect of dissipation becomes significant even when the plasma conductivity is high, so that the condition for the magnetic field to be frozen in the plasma can be violated. The regions with a high electric-current density, which separate the magnetic fields of different orientation and accumulate an excessive magnetic energy, usually take the form of current sheets [1]. In two-dimensional (2D) magnetic configurations with null-lines, the formation of current sheets was predicted theoretically (see [1] and the literature cited therein) and then was realized experimentally in a wide range of parameters [2]. In the last years, particular attention has been drawn to three-dimensional (3D) magnetic configurations. Until recently, the formation of CSs in such magnetic configurations has been associated with the presence of magnetic null-points [3–5]. However, it was shown experimentally that CSs can form not only in the vicinities of magnetic null-points [6] but also far away from the region of zero magnetic field and even in nonuniform magnetic fields that contain no null-points inside the plasma [7].

Among 3D magnetic configurations, configurations with singular X-lines are of particular interest. The reason is that they occur frequently in nature and laboratory experiments (in active regions in the solar corona, closed magnetic confinement systems, etc.) and are of fundamental importance for plasma physics. The magnetic field in the vicinity of a simplest X-line can be written in the form

$$\mathbf{B} = \{hx; -hy; B_\parallel\}. \quad (1)$$

Here, the z-axis coincides with the singular line, and the magnetic field in the (x, y) plane is a 2D field with $\mathbf{B} = 0$ at $x = 0$ and $y = 0$ and the radial gradient h. In contrast to [6, 7], here we restrict ourselves to a situation when all the parameters are uniform along the singular line, in particular,

$$\partial B_\parallel/\partial z \longrightarrow 0. \quad (2)$$

Compared with a null-line and null-point, a singular line of the X-type can be classified as a more general structural element of the magnetic field, because the null-line is the X-line with zero longitudinal component $B_\parallel = 0$ and also, in configurations with null-points, the singular X-line is present both in the region of zero magnetic field and far away from this region. According to theoretical predictions, in the vicinity of a singular X-line, cumulative effects, as well as magnetic reconnection, can occur in a plasma [1, 8].

In this work, the possibility of CS formation in magnetic fields (1) with singular X-lines was studied experimentally for the first time. Main attention was focused, first, on searching the range of initial conditions, in particular, quantitative characteristics of initial magnetic configurations in which CSs can be formed, and, second, on determining how the CS parameters depend on the structure of the initial magnetic configuration.

2. Figure 1 shows a schematic of the CS-3D experimental device. The magnetic configuration with an X-line (1) is created using a superposition of two fields: a 2D field $\mathbf{B}_\perp$ with a null-line and radial gradi-

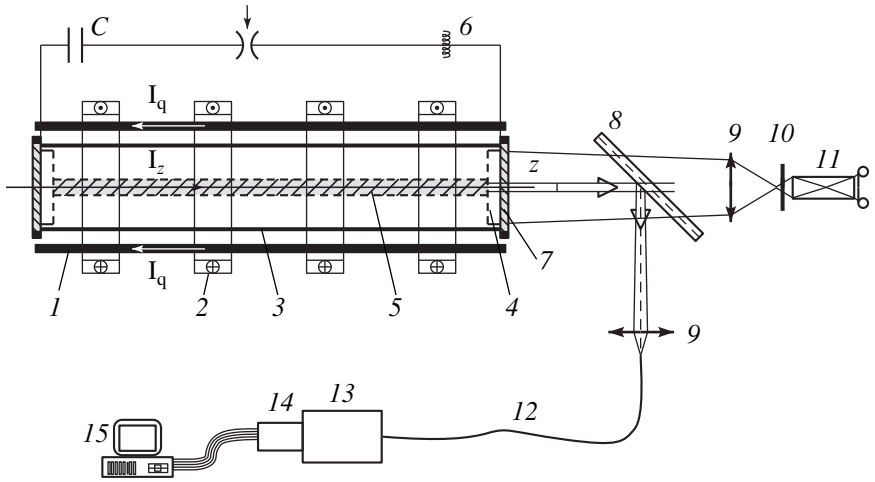

Fig. 1. Schematic of the CS-3D experimental device and diagnostic equipment: (*1*) straight current conductors producing a 2D magnetic field configuration with a null-line on the *z*-axis, (*2*) coils producing a uniform axially symmetric magnetic field B_z, (*3*) quartz cylindrical vacuum chamber 18 cm in diameter and 100 cm long, (*4*) grid electrodes, (*5*) current sheet, (*6*) Rogowski coil, (*7*) quartz windows, (*8*) mirror with a transmittance of 50%, (*9*) lenses, (*10*) interference filter, (*11*) image intensifier for recording plasma images, (*12*) quartz fiber 400 μm in diameter and 10 m long, (*13*) MDR-3 monochromator, (*14*) MORS-3 multichannel optical recorder, and (*15*) PC-486.

ent $h \le 600$ G/cm and a uniform field $B_{\|} \le 6$ kG directed along the null-line. The magnetic fields are produced by individual electrotechnical systems, so that we could independently change the parameters of each field, thus forming the configurations with different ratios between the longitudinal and transverse field components. Both magnetic fields were quasisteady with respect to the processes occurring in the plasma. An evacuated vacuum chamber was filled with helium at a pressure of 300 mtorr. An initial plasma with a density of $N_e \le 10^{16}$ cm^{-3} was produced through an auxiliary Θ-discharge with strong preionization. A subsequent generation of the electric current I_z directed along the X-line initiated the plasma motion in the magnetic field, which, in principle, could result in the formation of a current sheet. The half-period of the plasma current was equal to $T/2 = 5$ μs, and its maximum value was varied within the range $I_z^{\max} = 40$–100 kA.

Qualitatively, the features of the plasma structure at various instants can be derived from 2D distributions of plasma emission in the (x, y) plane for different spectral lines (see Fig. 2). These distributions (integral in the *z* direction) were recorded by an image intensifier in combination with a narrow-band ($\Delta\lambda_{1/2} \approx 1.1$ nm) interference filters [9]. The electron density in different plasma regions was deduced from an analysis of profiles of the HeII 468.6- and HeI 587.6-nm spectral lines. The emission from the central region of the vacuum chamber (1.2–1.5 cm in diameter and 60 cm long) was recorded using an MDR-3 monochromator and a multichannel MORS-3 recorder consisting of an MCP image intensifier and a multichannel CCD array [10]. The plasma emission spectra were recorded and averaged over a time interval of ≅0.6–0.7 μs. The experimental spectral-line profiles were approximated by theoretical profiles as convolutions of the dispersion (Lorentzian) and Gaussian profiles. It was found that the Doppler broadening was small compared with the instrumental function, and the mechanism responsible for the broadening of the HeII and HeI lines was associated with the electron impact broadening, which allowed us to determine the electron density under different conditions (see Fig. 3). The configuration of the plasma electric current was determined using magnetic probes placed outside the vacuum chamber [11].

3. The generation of the plasma electric current I_z results in a significant deformation of the initial spatial distribution of the plasma produced in the magnetic field, giving rise to a new current–plasma structure. 2D images of the emitting plasma demonstrate the dependence of these structures on the parameters of the magnetic configurations (see Fig. 2). The images can be divided into two groups: one group corresponds to the formation of a current sheet (frames *1*, *2*, *5*, *6*) and the other corresponds to the formation of a sheet-like double-piece structure consisting of two sheaths separated by a slopping split, the emission from which in both HeII and HeI lines is absent (frames *3*, *4*, *7*, *8*). The images from the first group are relatively thin strips extended along the *x*-axis (the width is $2\Delta x \ge 16$ cm and the thickness is $2\Delta y \le 1$ cm), which are identical to those observed when the current sheet was formed in a 2D magnetic field with a null-line (Fig. 2, frame *5*) (see also [9]). The images have almost the same shape in the HeII and HeI spectral lines (Fig. 2, frames *1*, *2*), except for a characteristic minimum in the intensity of the HeI line in the sheet midplane, where the intensity of the HeII line is maximum. This peculiarity is typical for the current sheets produced in 2D fields with null-lines

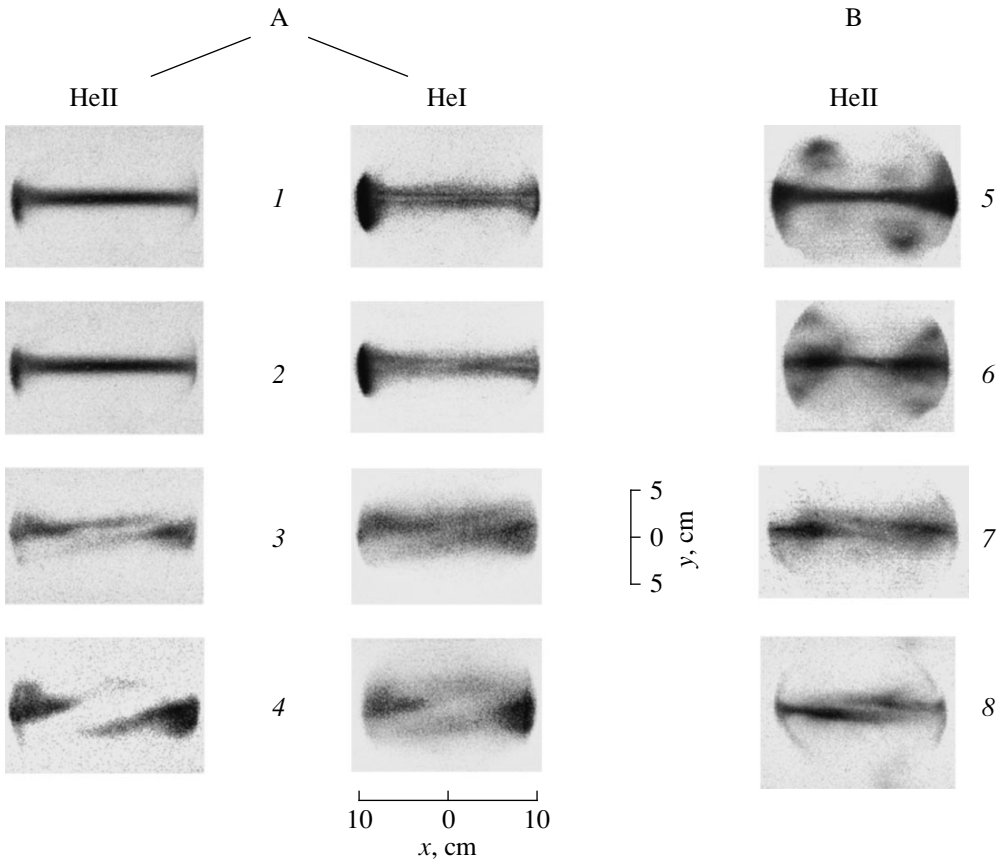

Fig. 2. Plasma images in HeII 486.6- and HeI 587.6-nm spectral lines under different conditions. (A) Plasma images for $B_z = 4.3$ kG, $I_z^{max} \cong 100$ kA, $t \cong 2.5$ μs, and different values of the gradient h of the 2D magnetic field: h = (*1*) 570, (*2*) 420, (*3*) 280, and (*4*) 200 G/cm. (B) Plasma images for $h = 200$ G/cm, $I_z^{max} \cong 40$ kA, $t \sim 2$ μs, and different magnitudes of the magnetic field: B_z = (*5*) 0, (*6*) 1.4, (*7*) 2.9, and (*8*) 5.7 kG.

when the electron temperature T_e and/or the plasma density N_e are maximum at the sheet midplane and cause rapid ionization of helium atoms and, consequently, depletion of the HeI spectral lines.

Magnetic measurements allow us to draw the following conclusion about the formation of a planar sheet in which the plasma electric current is concentrated: the width (the size in the x direction) of the current sheet significantly exceeds its thickness (the size along the y-axis), and the current width can attain a size close to the vacuum-chamber diameter.

Hence, the analysis of the emitting-plasma images and the results of magnetic measurements show that a planar current sheet, in which the plasma is concentrated, can actually be formed in magnetic configurations with an X-line, i.e., in the presence of a sufficiently strong longitudinal component directed along the X-line. In this case, the longitudinal component can exceed the transverse one throughout the most part of or even the entire vacuum volume: $B_\| \geq |\mathbf{B}_\perp| = h^*|\mathbf{r}|$ for $|\mathbf{r}| \leq R_k$.

4. Although the 2D plasma images in the presence of a longitudinal magnetic-field component were similar to those obtained in the absence of this component, the effect of $B_\|$ clearly manifested itself in variations of the electron density (Fig. 3). The sheet formation in the 2D field with a null-line ($B_\| = 0$) was accompanied by an efficient compression of the plasma: the maximum density in the sheet midplane ($y \longrightarrow 0$) reached $N_e \cong (4–5) \times 10^{16}$ cm^{-3}, exceeding the initial gas-atom density by a factor of ~5 (Fig. 3, curve *1*). At the periphery of the sheet ($|y| \cong 0.2–0.4$ mm), the electron density was equal to $N_e \cong (2–3) \times 10^{16}$ cm^{-3} (curve *2*) (see also [2, 9, 10]). However, in the presence of the longitudinal component, the maximum electron density was markedly lower: $N_e \cong 2 \times 10^{16}$ cm^{-3} for $B_\| = 4.3$ kG, and the broadening of both the HeI and HeII lines gave almost the same value of N_e (curves *3*, *4*).

Thus, when the sheet was formed in the magnetic field with an X-line (i.e., in the presence of the longitudinal component $B_\|$), the efficiency of the plasma compression into the sheet was lower than that for the sheet

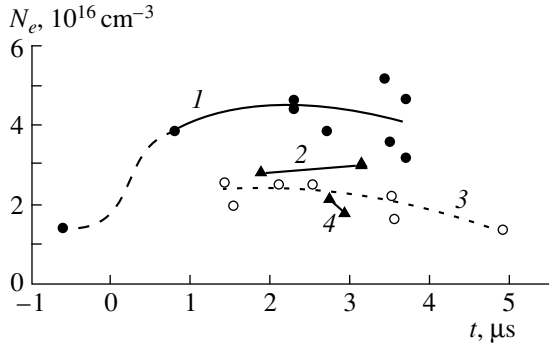

Fig. 3. Time dependence of the electron density inferred from the broadening of (*1*, *3*) HeII 468.6- and (*2*, *4*) HeI 587.6-nm spectral lines for h = 570 G/cm, $I_z^{\max} \cong 100$ kA, and B_z = (*1*, *2*) 0 and (*3*, *4*) 4.3 kG.

formed in the 2D field ($B_\parallel = 0$). This effect is apparently related to an enhancement of $B_\parallel$ in the sheet itself due to the transport of this component by the plasma in the stage of the sheet formation.

As is known [1], the longitudinal component can produce an additional pressure similar to the plasma thermal pressure, thus increasing the total pressure inside the sheet. Let us write the transverse-balance condition for the current sheet in the magnetic field,

$$8\pi N_e(T_e + T_i/\bar{Z}_i) + (\delta B_\parallel)^2 = B_x^2, \qquad (3)$$

where T_e and T_i are the electron and ion temperatures in the sheet, Z_i is the effective ion charge, $\delta B_\parallel$ is the excess in the longitudinal component inside the sheet over its value outside the sheet, and B_x is the transverse field component tangential to the sheet surface. Near the middle of the sheet (at $x \longrightarrow 0$), the following relation is usually valid (see [1, 2, 9]):

$$B_x \cong \sqrt{0.4 I_z h}. \qquad (4)$$

Then, for $N_e \cong 5 \times 10^{16}$ cm^{-3}, h = 570 G/cm, I_z = 100 kA, and $B_\parallel = 0$, we have B_x = 4.8 kG and $T_e + T_i/\bar{Z}_i \cong 11$ eV. Under these conditions, the characteristic time of equalizing the electron and ion temperatures is less than 0.1 μs and $\bar{Z}_i \cong 1$. Hence, for time intervals of interest, it is reasonable to assume that $T_e \cong T_i \cong$ 5–6 eV. The plasma temperature in the current sheet formed in the presence of the longitudinal component $B_\parallel$ = 4.3 kG, presumably, is close to this value. Actually, the fact that the HeI spectral line is depleted and, simultaneously, the high intensity is observed in the HeII line (Fig. 2, frames *1*, *2*) indicates that 5 eV $\le T_e \ll$ 15 eV and $\bar{Z}_i \cong 1$. The time of the T_e and T_i equalization for $N_e \cong 2 \times 10^{16}$ cm^{-3} is less than 0.2 μs, so we assume $T_e \cong T_i$. Then, from condition (3), we can calculate the change in the longitudinal magnetic-field component in the sheet: $\delta B_\parallel \cong 3.7$ kG, which comprises ≈80–90% of the initial $B_\parallel$ value. Therefore, the total longitudinal field inside the sheet attains $B_\parallel^{sh} \simeq 8$ kG.

Hence, characteristic of CS formation in 3D magnetic fields with X-lines are an enhancement of the longitudinal magnetic-field component inside the sheet and a less efficient plasma compression compared with 2D fields with null-lines.

5. Let us examine the parameters of initial magnetic configurations (1) in which the formation of a planar current sheets is possible. When the longitudinal component is kept constant and equal to $B_\parallel$ = 4.3 kG, the sheet formation becomes no longer possible for the values of the transverse gradient $h \le 280$ G/cm, which corresponds to $B_\parallel/h \ge 15.3$ cm (Fig. 2, column A). When the gradient is kept constant, h = 200 G/cm (column B), the sheet formation becomes impossible for $B_\parallel \ge 2.9$ kG ($B_\parallel/h \ge 14.5$ cm). Hence, it follows that, for a current sheet can be formed in a magnetic configuration with an X-line, the ratio $B_\parallel/h$ should not exceed a certain critical value. In particular, for this experiment, we obtain $B_\parallel/h \sim 15$ cm, which presumably is related to geometrical factors: X-line length, electrode diameter, etc.

6. Plasma structures for $B_\parallel/h \ge 15$ cm develop in the sheet-like form, but only far away from the X-line, i.e., in the region where the transverse magnetic-field component $|\mathbf{B}_\perp| = h^*|\mathbf{r}|$ is sufficiently large. (Note, however, that the inequality $|\mathbf{B}_\perp| \le B_\parallel$ holds throughout the plasma volume.) In the central region, one can clearly see a slopping split that divides the plasma structure in two parts (Fig. 2, frames *3*, *4*); plasma emission in both HeI and HeII spectral lines is absent inside this split. It is reasonable to assume that, in this region, there is a local minimum in the plasma density, i.e., a plasma cavity shaped as a well-defined slopping split.

7. Thus, in this study, it is shown for the first time that CSs can be formed in magnetic configurations with X-lines and quantitative characteristics are determined for initial configurations in which sheets are formed. It is found that the CS can be formed in the presence of a sufficiently strong uniform magnetic field $B_\parallel$ directed along the X-line, in particular, if $B_\parallel > |\mathbf{B}_\perp|$ throughout the entire plasma volume.

It is shown that the efficiency of plasma compression into the sheet decreases as the longitudinal component of the magnetic field with an X-line increases, so that, in the presence of $B_\parallel$, the electron density in the sheet is markedly lower compared with 2D magnetic configurations with null-lines ($B_\parallel = 0$). The decrease in the electron density is due to a substantial increase in $B_\parallel$ inside the sheet itself.

It is found that, if $B_\parallel$ exceeds a certain critical value, a planar current sheet cannot be formed: instead of the sheet, there appear two sheaths separated by a cavity with a local minimum in the electron density. The critical parameter, determining the possibility of the CS formation in magnetic fields with X-lines, is the ratio

between the gradient of the 2D field, h, and the value of the $B_{\|}$ component.

ACKNOWLEDGMENTS

We thank G.M. Batanov for fruitful discussions and V.B. Burilina for assistance in experiments. This work was supported in part by the Russian Foundation for Basic Research, project no. 99-02-18353, and INTAS.

REFERENCES

1. S. I. Syrovatskiĭ, Annu. Rev. Astron. Astrophys. **19**, 163 (1981).
2. S. Yu. Bogdanov, N. P. Kyrie, and A. G. Frank, Trudy IOFAN (Proc. of Inst. of General Phys., Russ. Acad. Sci.) **51**, 5 (1996).
3. P. Rosenau, Phys. Fluids **22**, 849 (1979).
4. S. V. Bulanov and M. A. Ol'shanetskiĭ, Fiz. Plazmy **11**, 727 (1985) [Sov. J. Plasma Phys. **11**, 425 (1985)].
5. J. Greene, Phys. Fluids B **5**, 2355 (1993).
6. S. Yu. Bogdanov, V. B. Burilina, V. S. Markov, and A. G. Frank, Pis'ma Zh. Éksp. Teor. Fiz. **59**, 510 (1994) [JETP Lett. **59**, 537 (1994)].
7. A. G. Frank, Plasma Phys. Controlled Fusion **41** (3A), A687 (1999).
8. B. B. Kadomtsev, Usp. Fiz. Nauk **151**, 3 (1987) [Rep. Prog. Phys. **50**, 115 (1987)].
9. S. Yu. Bogdanov, V. B. Burilina, and A. G. Frank, Zh. Éksp. Teor. Fiz. **114**, 1202 (1998) [JETP **87**, 655 (1998)].
10. S. Büscher, N. P. Kyrie, H.-J. Kunze, and A. G. Frank, Fiz. Plazmy **25**, 185 (1999) [Plasma Phys. Rep. **25**, 164 (1999)].
11. V. B. Burilina, V. S. Markov, and A. G. Frank, Fiz. Plazmy **21**, 36 (1995) [Plasma Phys. Rep. **21**, 33 (1995)].

Translated by N. Larionova

JETP Letters, Vol. 71, No. 2, 2000, pp. 58–61. Translated from Pis'ma v Zhurnal Éksperimental'noĭ i Teoreticheskoĭ Fiziki, Vol. 71, No. 2, 2000, pp. 85–90.

PLASMA, GASES

Melting of a Dust Crystal with Defects

I. V. Shveĭgert*, V. A. Shveĭgert*, A. Melzer, and A. Piel****

**Institute of Theoretical and Applied Mechanics, Novosibirsk, 630090 Russia*

***Institut für Experimentelle und Angewandte Physik, Christian-Albrechts-Universität, 24098 Kiel, Germany*

**e-mail: ischweig@site.itam.nsc.ru*

Received December 24, 1999

Abstract—The effect of defects on the melting of a two-layer dust Wigner crystal in the electrode layer of a radio-frequency gas discharge is investigated by Langevin molecular dynamics. Two types of defects have been included in the consideration: (a) point defects and dislocations and (b) particles levitating above and below a two-layer crystal (so-called *strong* defects). It is shown that local melting of a two-layer crystal found experimentally is explained by the occurrence of strong defects located *above* the crystal. © *2000 MAIK "Nauka/Interperiodica".*

PACS numbers: 52.25.Zb; 6470-p

The melting of two-dimensional (2D) crystals of classical particles is a fundamental problem that has been attracting experimental and theoretical studies for the last 25 years [1, 2]. The phase transition of melting was observed in electronic crystals at the surface of liquid helium [3], in colloidal suspensions [4], and in plasma dust crystals [5–7], which represent a new experimental system for studying 2D crystal structures. As a rule, dust crystals in a laboratory gas-discharge plasma consist of similar, negatively charged particles of micrometer sizes and are retained in the electrode layer by the electric and gravitational fields.

The following unusual properties of the dust crystal were revealed in a number of experiments [8–11]. If particles form a conventional hexagonal lattice in the horizontal plane parallel to the electrode, they are arranged one beneath another in the vertical direction, aligning in vertical chains. This crystal structure signifies that the Debye–Hückel model is inapplicable to the description of charged particles interacting in plasma with an ion flux.

In addition, the experiments [5, 6] demonstrated that a decrease in gas pressure in the gas-discharge chamber leads to a significant rise in the vibrational kinetic energy of particles and to melting of the crystal. The temperature of the surrounding gas and the charge of particles remain virtually unchanged in this process. This surprising phenomenon is observed only in experiments with a dust crystal in an electrode layer. It is known that a change in the viscosity of the environment does not change the statistical properties of the system in the case of 2D and 3D crystals. The phenomenon of particle alignment into chains in an ion flux was considered in [12–15]. It was shown that the ion flux is focused by negatively charged particles, which results in the formation of regions with an elevated ion concentration immediately beyond particles. In addition, it was shown in theoretical investigations [14–16] and in more recent experiments [17, 18] that electrostatic interaction in the system is asymmetric. Each ion cloud interacts with all particles except for its own particle with which it forms a dipole configuration. An investigation of the mechanism of heating of a two-layer defect-free crystal in an electrode layer [7, 14, 15, 19] showed that melting is a two-step process. Initially, as friction decreases, instability develops, and the crystal passes into a hot crystalline state with developed oscillations of particles. Subsequently, as pressure decreases, the two-layer crystal melts. Asymmetry in the screening of particles and the nonpotential character of interaction are the major reasons for the development of instability. The calculated average kinetic energy of particles agrees with experimental data by order of magnitude; however, the qualitative pattern of crystal melting in the experiment essentially differs from the calculated one. In a real crystal, the formation of hot spots occurs initially, and next liquid regions are formed along with crystalline fragments. As the gas pressure further decreases, the system entirely passes into a liquid state [5]. The average energy of particles measured in experiment gradually increases in a wide pressure range, whereas the temperature of particles sharply increases in calculations when the gas pressure attains a critical value.

In experiments, a dust crystal always has point and extended defects in lattices and additional particles above and below the basic lattices. In this work, the melting of a two-layer crystal with defects is studied by Langevin molecular dynamics based on the model proposed in [14, 15]. It is suggested that (a) particles move in a plane parallel to the electrode (which follows from experiment) and (b) particles are asymmetrically screened by ions. With these assumptions, the real ion distribution is replaced by a symmetric distribution and

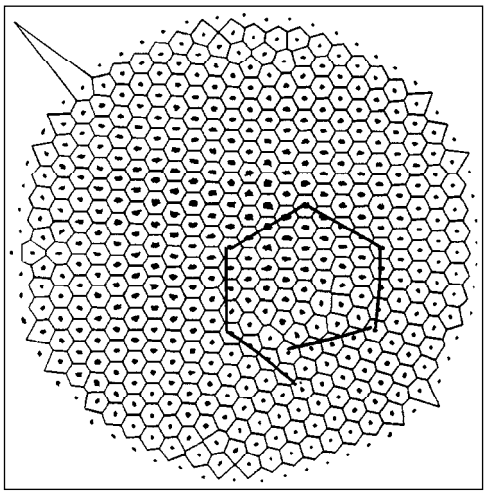

Fig. 1. Trajectories of particles in the upper lattice of a two-layer dust crystal with defects at $\nu = 0.0721\omega_{pd}$ before melting. The Burgers vector of uncorrelated dislocations equals 2.

an effective point charge located below the particle and rigidly bound to it. This simplification is justified, because any displacement of a particle immediately generates redistribution of ion density around it [14, 15]. First, we consider a large two-layer cluster (996 particles) in which dislocations with the Burgers vector equal to 2 formed upon numerically cooling the system from a high-temperature liquid state, see Fig. 1. In addition, a set of point defects is formed in the vicinity of the cluster border, because a hexagonal structure can be inscribed into a circle only with a certain number of point defects.

Particles interact through a screened Coulomb potential $V(\mathbf{r}_i, \mathbf{r}_j) = (C/|\mathbf{r}_i - \mathbf{r}_j|)\exp(-\kappa|\mathbf{r}_i - \mathbf{r}_j|)$ with each other ($C = Z^2$) and with positive effective charges ($C = ZZ_c$); here, $\mathbf{r}_i$ is the coordinate of the ith particle, $1/\kappa$ is the screening length, and $\kappa = 2/a$, where a is the average interparticle distance. The external potential restricting the system in the radial plane is chosen in such a way that the calculated particle density coincide with the experimental particle density. The following parameters were taken from the experiment [5]: dust particle radius $R = 4.7$ μm, particle mass $M = 6.73 \times 10^{-13}$ kg, and particle charge $Z = 16000e$; distance between particles $a = 450$ μm; and distance between layers $d = 0.8a$. In calculations, the positive charge was taken $Z_c = 0.5Z$ with the vertical distance $d_c = 0.6a$ [15]. The characteristic vibration frequency in the crystal for our experimental conditions equals $\omega_{pd} = \sqrt{Z^2e^2/\epsilon_0 Ma^3} = 110\ \text{s}^{-1}$. The transition from the solid state to liquid in experiment is observed in the case when pressure is decreased from 120 to 40 Pa, which corresponds to the change of the friction coefficient of the particle in the gas phase from $\nu = 32$ to $10\ \text{s}^{-1}$ [20].

The dynamics of particle motion is studied under conditions when the friction coefficient decreases. The average kinetic energy of particles in the upper layer is presented in Fig. 2a as a function of the friction coefficient. At a high gas pressure, the system has a crystalline structure, and the kinetic energy of particles approximately coincides with the gas temperature. A progressive decrease of friction down to the critical value ν_{in} only slightly changes the state of the system in spite of the occurrence of defects (Fig. 2a, regime I). At the critical point ν_{in}, the kinetic energy rapidly increases, and the system passes into a hot crystalline state, which is characterized by developed vibrations of particles (regime II). In the subsequent range of the friction coefficient $\nu_* < \nu < \nu_{in}$, the two-layer crystal passes through a sequence of hot stationary crystalline states. Figure 1 displays trajectories of particles immediately before melting. The occurrence of a dislocation does not reveal itself in the figure, and it may be con-

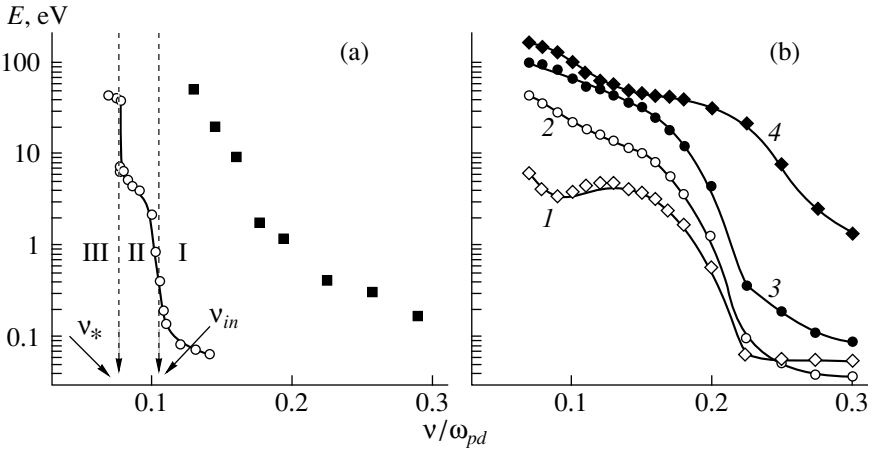

Fig. 2. Average kinetic energy of dust particles as a function of the friction coefficient in a two-layer crystal (a) with point defects and dislocations (calculation, solid circles; experiment [5], solid squares) and (b) with strong defects (*1* upper incomplete layer, *2* upper lattice, *3* lower lattice, and *4* lower incomplete layer).

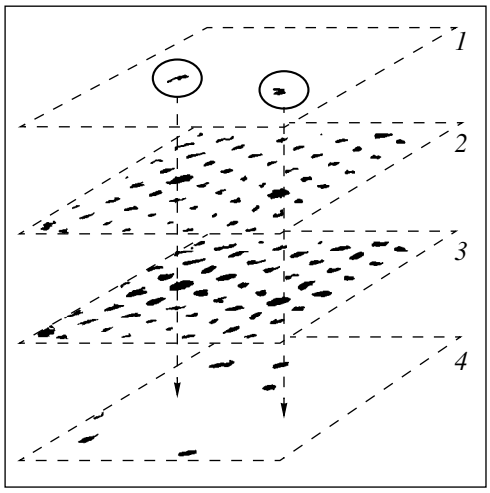

Fig. 3. Fragment of a two-layer crystal with strong defects: *1* upper incomplete layer, *2* upper lattice, *3* lower lattice, and *4* lower incomplete layer. Circles designate the position of upper strong defects.

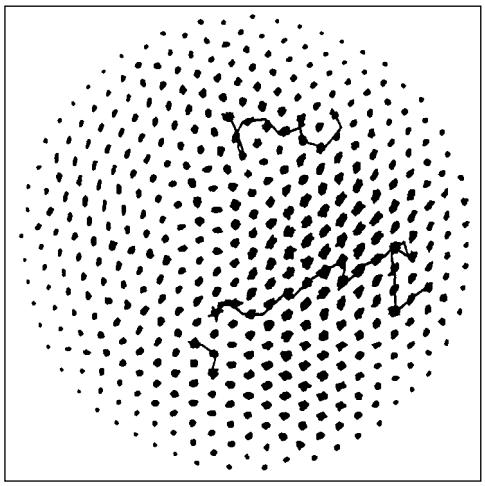

Fig. 4. Trajectories of particles in the lower lattice of a two-layer crystal at $\nu = 0.12\omega_{pd}$. More extended trajectories correspond to three lower strong defects.

cluded that point and extended defects insignificantly increase the crystal temperature.

As friction decreases further, the formation of thermally induced defects is observed at the second critical point, and the system passes into isotropic liquid (regime III). As a whole, the process of melting of a two-layer crystal with point and extended defects turned out to be similar to the melting of a defect-free crystal [7, 19].

Let us next consider the effect of additional particles located above and below the crystal (see Fig. 3) on the process of melting. The number of particles over the crystal is 20, and that beneath the crystal is 25, which corresponds to 5% total number of particles. The distance between the additional layers and lattices equals the distance between lattices.

As in the preceding case, the structure with additional particles has a crystalline order at high pressure. However, the occurrence of strong defects leads to a significant increase in the average kinetic energy of particles (see Fig. 2b). Each layer has a different temperature, and the temperature increases with passing from the upper layers to lower ones. The energy of the lower strong defects is considerably higher than the energy of the other particles even at high pressure. As the pressure decreases, instability in the crystal with strong defects develops considerably earlier, and motion in some regions is especially intense. We found that the most effectively heated particles are located in vertical chains with strong defects, see Fig. 3. The reason for the dominant role of the upper additional particles is the fact that, because of ion flux focusing, each particle forms a dipole particle, and the lower dipoles follow the motion of the upper particles.

In order to understand the role of additional particles located below the crystal, consider the melting of a two-layer crystal with three lower particles. Trajectories of particles in the lower lattice and trajectories of three strong defects located below the crystal at $\nu = 0.12\omega_{pd}$ are displayed in Fig. 4. Particles located below the crystal have a large kinetic energy, which virtually coincides with the energy of strong defects located below the crystal, Fig. 2b. Because of scattering by the nearest lattice due to Coulomb interaction, particles located below the crystal pass their momentum to particles in the lattice. It is evident in Fig. 4 that the part of the crystal located over an extended trajectory of a lower particle has a higher temperature. The lower additional particles, in spite of their high energy, move over electric potential minimums located under the particles of the lower lattice.

It is interesting to note that, according to our calculations, individual high-energy particles observed experimentally under the crystal and generating Mach cones in crystalline structures [21] are formed because of the development of instability in the system.

Note in conclusion that the inclusion of strong defects in the system qualitatively changes the pattern of melting and significantly increases the heating temperature of a two-layer dust crystal. The calculated average kinetic energy of particles monotonically increases with decreasing pressure because of the local heating of the crystal under the upper particles and coincides with experimental data to a good accuracy. In the given case, the melting of the two-layer crystal is caused by both global heating due to the development of instability and local heating through strong defects. The upper additional particles are more important for heating than the lower ones because particles are asymmetrically screened in the ion flux.

ACKNOWLEDGMENTS

This work was supported by INTAS and the Russian Foundation for Basic Research, joint project no. IR-97-775 and by Deutsche Forschungsgemeinschaft, project no. 436 RUS 113/183/1,2.

REFERENCES

1. M. A. Glaser and N. A. Clark, in *Advances in Chemical Physics*, Ed. by I. Prigogine and S. A. Rice (Wiley, New York, 1993).
2. K. J. Strandburg, Rev. Mod. Phys. **60**, 161 (1988).
3. C. C. Grimes and G. Adams, Phys. Rev. Lett. **42**, 795 (1979).
4. K. Zahn, J. M. Méndez-Alcaraz, and G. Maret, Phys. Rev. Lett. **79**, 175 (1997).
5. A. Melzer, A. Homann, and A. Piel, Phys. Rev. E **53**, 2757 (1996).
6. H. Thomas and G. E. Morfill, Nature **379**, 806 (1996).
7. V. A. Schweigert, I. V. Schweigert, A. Melzer, *et al.*, Phys. Rev. Lett. **80**, 5345 (1998).
8. J. H. Chu and Lin I, Phys. Rev. Lett. **72**, 4009 (1994).
9. H. M. Thomas, G. E. Morfill, G. V. Demmel, *et al.*, Phys. Rev. Lett. **73**, 652 (1994).
10. Y. Hayashi and K. Tachibana, Jpn. J. Appl. Phys. **33**, L804 (1994).
11. A. Melzer, T. Trottenberg, and A. Piel, Phys. Lett. A **191**, 301 (1994).
12. S. V. Vladimirov and M. Nambu, Phys. Rev. E **52**, R2172 (1995).
13. F. Melandsö and J. Goree, Phys. Rev. E **52**, 5312 (1995).
14. A. Melzer, V. A. Schweigert, I. V. Schweigert, *et al.*, Phys. Rev. E **54**, R46 (1996).
15. V. A. Schweigert, I. V. Schweigert, A. Melzer, *et al.*, Phys. Rev. E **54**, 4155 (1996).
16. V. A. Schweigert, V. M. Bedanov, I. V. Schweigert, *et al.*, Zh. Éksp. Teor. Fiz. **115**, 877 (1999) [JETP **88**, 482 (1999)].
17. A. Melzer, V. A. Schweigert, and A. Piel, Phys. Rev. Lett. **83**, 3194 (1999).
18. K. Takahashi, T. Oishi, K. Shimomai, *et al.*, Phys. Rev. E **58**, 7805 (1998).
19. I. V. Schweigert, V. A. Schweigert, V. M. Bedanov, *et al.*, Zh. Éksp. Teor. Fiz. **114**, 1 (1998) [JETP **87**, 905 (1998)].
20. P. S. Epstein, Phys. Rev. **23**, 710 (1924).
21. D. Samsonov, J. Goree, Z. W. Ma, *et al.*, Phys. Rev. Lett. **83**, 3649 (1999).

Translated by A. Bagatur'yants

JETP Letters, Vol. 71, No. 2, 2000, pp. 62–64. Translated from Pis'ma v Zhurnal Éksperimental'noĭ i Teoreticheskoĭ Fiziki, Vol. 71, No. 2, 2000, pp. 91–94.

CONDENSED MATTER

Low-Frequency Dispersion of the Effective Transverse Conductivity in Inhomogeneous Media in Strong Magnetic Field

Yu. A. Gurvich*, A. P. Mel'nikov*, L. S. Al'perovich, and I. A. Chaĭkovskiĭ*****

** Moscow State Pedagogical University, Moscow, 119891 Russia*
e-mail: gurvich@rpl.mpgu.msk.su
*** Tel-Aviv University, Ramat-Aviv, 69978 Israel*
**** Ben-Gurion University of the Negev, Beer-Sheva, 84105 Israel*

Received December 9, 1999

Abstract—On crystalline silicon specimens with a nonuniform carrier concentration distribution produced by an optical method, a dispersion of the effective transverse conductivity $\sigma_\perp^{\text{eff}}(\omega)$ is observed near the frequency $\omega \approx \omega_c = \tau_\perp^{-1} \equiv \varepsilon/4\pi\sigma_\perp^{\text{eff}}$. At $\omega < \omega_c$, an anomalous transverse effective conductivity is observed: $\sigma_\perp^{\text{eff}}(\omega)$ is greater than the transverse conductivity of a homogeneous specimen $\sigma_\perp^h(\omega)$ (in the frequency range studied in the experiment, $\sigma_\perp^h(\omega) = \text{const}$). Near $\omega \approx \omega_c$, the conductivity $\sigma_\perp^{\text{eff}}$ decreases, and, at $\omega > \omega_c$, it coincides with $\sigma_\perp^h$.

PACS numbers: 72.20My; 72.80.Cw

1. In homogeneous conductors, a dispersion of the conductivity σ occurs at frequencies of the order of the inverse momentum relaxation time τ_p^{-1}. In an inhomogeneous conductor, an external electric field gives rise to local charge bunches. Near the inhomogeneities, local electric fields and gradients of the charge carrier concentration are formed, and they tend to dissipate the bunches. The characteristic time of such a bunch dissipation is the Maxwell relaxation time $\tau_M = \varepsilon/4\pi\sigma$ (ε is the dielectric constant of the material). At low frequencies, $\omega\tau_M \ll 1$ (ω is the frequency of the electric field), the effective conductivity σ^{eff} determined from the relation

$$\langle j \rangle = \sigma^{\text{eff}}(\omega)\langle E \rangle \tag{1}$$

(where $\langle j \rangle$ and $\langle E \rangle$ are the volume average values of the current density and field) is less than the average static conductivity: $\sigma^{\text{eff}}(\omega) \approx \sigma^{\text{eff}}(0) < \langle\sigma(0)\rangle$. At high frequencies, $\omega\tau_M \gg 1$ (but $\omega\tau_p \ll 1$; we assume that $\tau_M \gg \tau_p$, which is the usual case for semiconductors), a bunch has no time to form. In this case, $\sigma^{\text{eff}}(\omega) \approx \langle\sigma(0)\rangle$. For $\omega \sim \tau_M^{-1}$, a dispersion of conductivity (a low-frequency dispersion) was observed in the experiment described in [1]. The theory of this effect was developed in [2, 3].

2. In strong magnetic fields H: $\beta \equiv \mu H/c \gg 1$ (μ is the mobility and c is the velocity of light), the conductivity of a homogeneous specimen becomes highly anisotropic:

$$\sigma_{xx} \equiv \sigma_\perp \ll \sigma_{zz} \equiv \sigma_\parallel (\mathbf{H} \parallel 0z). \tag{2}$$

The Maxwell relaxation time also becomes anisotropic: $\tau_\perp = \varepsilon/4\pi\sigma_\perp \gg \tau_\parallel = \varepsilon/4\pi\sigma_\parallel$.

The dispersion of $\sigma_\perp^{\text{eff}}(\omega)$ was considered in [4] within the first approximation in the degree of inhomogeneity ξ (ξ is the ratio of the mean square fluctuation of the concentration to the mean concentration squared). A closer analysis [5] shows that at $\beta \gg 1$ the dispersion $\sigma_\perp^{\text{eff}}(\omega)$ should be observed at the frequencies

$$\omega \approx \omega_\perp = \tau_\perp^{-1} = \frac{4\pi\sigma_\perp^{\text{eff}}}{\varepsilon}, \qquad \omega \approx \omega_\parallel = \tau_\parallel^{-1} = \frac{4\pi\sigma_\parallel^{\text{eff}}}{\varepsilon} \tag{3}$$

($\omega_\perp \ll \omega_\parallel$). We note that $\sigma_\parallel^{\text{eff}} \approx \langle\sigma\rangle_{H=0}$.

3. As far as we know, so far no attempts had been made to experimentally observe the dispersion of $\sigma_\perp^{\text{eff}}(\omega)$. Presumably, this is related to two kinds of difficulties. First, it is difficult to fabricate an inhomogeneous structure of the "good semiconductor—bad semiconductor" type (see [6]). Second, the experiment requires ac measurements in a strong magnetic field in the closed Hall circuit regime, which is also quite complicated.

Meanwhile, such an experiment is of interest for the following reason. It is well known that, in a homoge-

neous specimen, the transverse conductivity $\sigma_\perp$ decreases with increasing magnetic field H (according to the elementary theory, $\sigma_\perp \sim \beta^{-2}$). In an inhomogeneous specimen, $\sigma_\perp^{\text{eff}}$ should decrease slower with H, namely: $\sigma_\perp^{\text{eff}} \sim \xi^{2/3}\beta^{-4/3}$ for three-dimensional inhomogeneities and $\sigma_\perp^{\text{eff}} \sim \xi\beta^{-1}$ for two-dimensional ones. This means that even for small values of ξ, in sufficiently strong magnetic fields H, the conductivity $\sigma_\perp^{\text{eff}}$ becomes greater than $\langle\sigma_\perp\rangle$, i.e., an anomalous transverse conductivity takes place (see [7] and references given there). This effect was first observed in the experiment described in [6]. An observation of the dispersion at the frequency $\omega \approx \omega_\perp$ would not only demonstrate the insignificance of inhomogeneities at high frequencies but also provide independent supporting evidence for the existence of the anomalous transverse conductivity.

4. The purpose of our experiments is to reveal the low-frequency dispersion of the effective transverse conductivity $\sigma_\perp^{\text{eff}}(\omega)$ of an inhomogeneous specimen in a strong magnetic field H. Below, we denote the transverse conductivity of a homogeneous specimen by $\sigma_\perp^h(\omega)$.

The measurements were carried out at a temperature of 4.2 K on Si : B crystalline specimens with the boron concentration $N \approx 6 \times 10^{15}$ cm^{-3} and mobility $\mu \approx 5 \times 10^4$ cm^2/V s. To obtain the closed Hall circuit regime, we used specimens in the form of a Corbino disk. A nonuniform distribution of the charge carrier concentration over the disk was formed by photoexcitation by an inhomogeneous radiation flux. A detailed description of the specimen and the method of photoexcitation can be found in [6].

The value of $\sigma_\perp$ at $\omega = 0$ and $H = 40$ kOe ($\beta \approx 20$) was about 10^{-10} Ω^{-1} cm^{-1}, which corresponds to $\tau_\perp \sim 10^{-2}$ s. Hence, the measurements were performed in the frequency band $20\ \text{s}^{-1} \le \omega \le 1000\ \text{s}^{-1}$.

5. Figure 1 presents the equivalent circuit of the measuring setup. The ac voltage from the oscillator was supplied to the specimen (R_S, C_S). A load R_L was connected in series with the specimen. The voltage across the load, which was proportional to the current, was measured by a phase-sensitive voltmeter (PAR-124a). The parameters of the circuit are as follows: for the specimen, $R_S = f(H)$ and, at $H = 40$ kOe, $R_S \approx 3 \times 10^{10}$ Ω; $C_S \approx 0.4$ pF; for the load, $R_L = 10^5$ Ω; for the voltmeter, $R_V \gg R_L$; and the total capacitance is $C_V \approx 70$ pF. The low resistance of the oscillator (≈ 50 Ω) shunts the capacitance of the lead to earth. The capacitance C_V is shunted by the resistance R_L (in the range of measurement $R_L \ll (\omega C_V)^{-1}$). The current through the specimen may be considerably affected only by the stray capacitance of the leads to each other, C_p. The main problem was to make the capacitance of C_p as small as possible. The value of C_p was determined from the experiment.

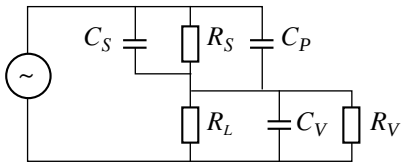

Fig. 1. Equivalent circuit of the measuring setup.

We measured the current through the load as a function of frequency, $I(\omega)$, for different cases: in the absence of the specimen in the circuit ((I_0), in the presence of a homogeneous specimen (I_h), and in the presence of an inhomogeneous one (I_{nh}). For each case, the measurements were performed twice: one measurement with the phase shifter angle of the voltmeter $\phi = 90$ ($I^{(1)}$) and the other measurement with $\phi = 0$ ($I^{(2)}$), which provided the measurements of the reactive and resistive current components, respectively. From these measurements, we obtained the following results.

(i) The angle $\phi = 90$: the reactive currents in the absence of the specimen $I_0^{(1)}$, in the presence of a homogeneous specimen $I_h^{(1)}$, and in the presence of an inhomogeneous one $I_{nh}^{(1)}$; the stray capacitance of the circuit C_p (≈ 0.6 pF), the capacitance of the circuit with a specimen, and the capacitance of the specimen C_S (≈ 0.4 pF). This agrees well with the calculated value.

(ii) The angle $\phi = 0$: the currents $I_0^{(2)}$, $I_h^{(2)}$, and $I_{nh}^{(2)}$. At $\phi = 0$, the reactive current is not completely suppressed by the voltmeter. From the measurements, we determined the reactive component rejection ratio for the instrument: $k(\omega) = I_0^{(1)}(\omega)/I_0^{(2)}(\omega) \approx 20$.

Figure 2a shows the experimental dependences $I_h^{(2)}(\omega)$ and $I_{nh}^{(2)}(\omega)$. One can see that the difference between the currents vanishes with increasing ω. The increase in the currents at higher ω is unrelated to the conductivity dispersion. It is a consequence of the incomplete suppression of the reactive component. By introducing the corrections for the rejection ratio, we obtained the true active currents through the specimen, $I_h^{(a)}(\omega)$ and $I_{nh}^{(a)}(\omega)$. They are shown in Fig. 2b.

6. Proceeding to the discussion, we note the following facts. The voltage amplitude is independent of frequency. The currents $I_h^{(a)}(\omega)$ and $I_{nh}^{(a)}(\omega)$ are proportional to $\sigma_\perp^h$ and $\sigma_\perp^{\text{eff}}(\omega)$, respectively. The ratio of these currents is equal to the ratio of the corresponding conductivities because the homogeneous and inhomogeneous specimens are represented by the same Corbino disk under different photoexcitation conditions. The intensity of photoexcitation was selected so as to

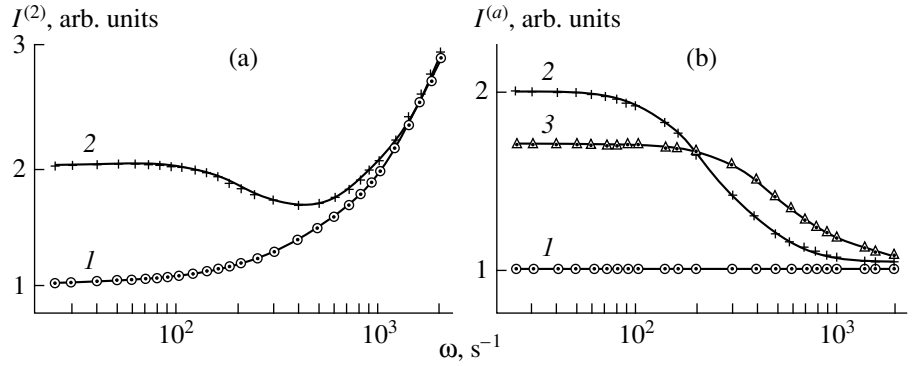

Fig. 2. (a) Frequency dependences of the currents for a homogeneous specimen (curve *1*) and an inhomogeneous one (curve *2*) at $\phi = 0$ and $H = 40$ kOe. (b) Frequency dependences of the active currents for the homogeneous (curve *1*) and inhomogeneous (curve *2*) specimens at $H = 40$ kOe. The value of $I_h^{(a)}$ at low frequencies ω is taken as the current unit. Curve *3* corresponds to $I_{nh}^{(a)}/I_h^{(a)}$ at $H = 30$ kOe.

provide the equality of these conductivities at $H = 0$ and $\omega = 0$. Therefore, the curves shown in Fig. 2b can be considered as the dependences $\sigma_\perp^{\text{eff}}(\omega)$ and $\sigma_\perp^h(\omega)$.

From Fig. 2b, one can drive the following conclusions: $\sigma_\perp^h$ does not depend on ω; $\sigma_\perp^{\text{eff}}$ experiences a dispersion near $\omega = \omega_c \approx 200$ s^{-1}; at $\omega < \omega_c$, the ratio of the conductivities is $\sigma_\perp^{\text{eff}}(\omega)/\sigma_\perp^h(\omega) = 2$, and the anomalous transverse conductivity [6] is observed; at $\omega > \omega_c$, the aforementioned ratio is equal to unity; i.e., the anomalous transverse conductivity vanishes at high frequencies, as was predicted in [4, 5].

The measured value of $\sigma_\perp^{\text{eff}}(0)$ is equal to 2.2×10^{-10} Ω^{-1} cm^{-1}. The frequency ω_c is close to the value of $\omega_\perp$ from formula (3) in accordance with the results obtained in [5].

As noted above, the theory [5] predicts the second low-frequency dispersion at the frequency $\omega_\parallel$ (see formula (3)). This frequency lies beyond the limits of our measurements. Besides, the question as to whether this kind of dispersion should be observed in the case of homogeneity along *H*, which was studied in our experiment, requires special consideration.

Up to this point, we discussed the results of the measurements at $H = 40$ kOe ($\beta \approx 20$). Figure 2b also shows the curve (curve *3*) obtained for $H = 30$ kOe ($\beta = 15$). It is seen that the anomalous transverse conductivity decreases and the frequency ω_c increases with decreasing *H*. The conductivity $\sigma_\perp^{\text{eff}}$ observed for $\omega \ll \omega_c$ increases almost proportionally to the frequency ω_c.

In closing, we note one more fact. In the literature, it was repeatedly noted that, with increasing β, the transverse conductivity $\sigma_\perp$ decreases slower than predicted by the theory: $\sigma_\perp^h \sim \beta^{-2}$. This fact is confirmed by our experiments. This discrepancy may be possibly explained by the assumption that the specimen possesses its own inhomogeneities that weaken the $\sigma(H)$ dependence. The study of the frequency dependences should also verify this assumption. Curve *1* in Fig. 2b demonstrates that $\sigma_\perp^h(\omega) = \text{const}$. Therefore, the weakening of the $\sigma_\perp^h(H)$ dependence is not related to the presence of inhomogeneities.

ACKNOWLEDGMENTS

The work of the authors from Russia was supported by the Russian Foundation for Basic Research, project no. 98-02-116898.

REFERENCES

1. A. N. Vystavkin, Yu. S. Gal'pern, and V. N. Gubankov, Fiz. Tekh. Poluprovodn. **2**, 1651 (1968) [Sov. Phys. Semicond. **2**, 1373 (1968)].
2. Yu. S. Gal'pern and A. L. Éfros, Fiz. Tverd. Tela **11**, 2301 (1969) [Sov. Phys. Solid State **11**, 1858 (1969)].
3. I. A. Chaikovskiĭ, G. M. Shmelev, and A. I. German, Phys. Status Solidi B **129**, 393 (1985).
4. Yu. M. Gal'perin and B. D. Laĭkhtman, Fiz. Tverd. Tela **13**, 2102 (1971) [Sov. Phys. Solid State **13**, 1760 (1971)].
5. I. A. Chaikovskiĭ and A. I. German, Phys. Status Solidi B **152**, 593 (1989).
6. L. S. Al'perovich, S. A. Grachev, Yu. A. Gurvich, *et al.*, Pis'ma Zh. Éksp. Teor. Fiz. **65**, 207 (1997) [JETP Lett. **65**, 224 (1997)].
7. O. E. Kvyatkovskiĭ, Zh. Éksp. Teor. Fiz. **85**, 202 (1983) [Sov. Phys. JETP **58**, 120 (1983)].

Translated by E. Golyamina

JETP Letters, Vol. 71, No. 2, 2000, pp. 65–68. Translated from Pis'ma v Zhurnal Éksperimental'noĭ i Teoreticheskoĭ Fiziki, Vol. 71, No. 2, 2000, pp. 95–99.

CONDENSED MATTER

Multichannel Hall Effects in 2D Electron Systems

V. B. Shikin* and Yu. V. Shikina**

** Institute of Solid State Physics, Russian Academy of Sciences, Chernogolovka, Moscow oblast, 142432 Russia*

*** Institute of Microelectronic Technology and Ultrahigh-Purity Materials, Russian Academy of Sciences, Chernogolovka, Moscow oblast, 142432 Russia*

Received December 9, 1999

Abstract—A description of available experimental data on the linear electrooptical effect in 2D electron systems exhibiting the quantum Hall effect is proposed. Allowance for the contact effects accompanying preparation of the Corbino discs and the Hall samples provides consistent description of the phenomena observed in the equilibrium state and in a state involving transport current. The contact potentials appear to have a rather large characteristic magnitude that is considerably greater than the cyclotron energy in the experiments being considered. Under these conditions, a large number of the so-called incompressible channels inevitably appear in the samples. The proposed phenomenological description of this "band" state is in qualitative agreement with available experiments. © *2000 MAIK "Nauka/Interperiodica".*

PACS numbers: 73.40.Hm

Earlier [1], we have discussed the properties of an individual incompressible region in an inhomogeneous 2D electron system exposed to a magnetic field. It was supposed that the inhomogeneity is caused by the contact phenomena that occur with large probability in open 2D systems with metallic terminals. In this study, we analyze the problem further and consider an actual situation [2–4] corresponding to the appearance of numerous incompressible channels in samples. A formalism is proposed that takes this effect into account.

1. As in [1], we consider the Corbino discs that allow quasi-one-dimensional description of a 2D region owing to the condition $(R_1 - R_2)/(R_1 + R_2) \ll 1$, where R_1 and R_2 are the inner and outer radii of a 2D Corbino disc, respectively. In this case, inhomogeneous component $\delta n(x)$ of the electron density related to the presence of contact is described by the following function:

$$\delta n_0(x) = \kappa w \phi_{ab}/\pi^2 e(w^2 - x^2), \quad -w \le x \le +w. \quad (1)$$

Here $2w = R_2 - R_1$ is the width of the 2D region between metallic boundaries, the x-axis is oriented in a radial direction, the coordinate origin coincides with the middle of the 2D region, κ is the dielectric constant of the medium, and ϕ_{ab} is the so-called contact potential difference. In the limit $a_b^* \ll w$, approximation (1) is applicable far from the points $x = \pm w$, where a_b is the effective Bohr radius.

When a magnetic field normal to the 2D-system plane is applied, a new substantial parameter—the cyclotron energy $\hbar\omega_c$—appears and the character of the distribution of incompressible channels in the disc is determined primarily by the interplay of $\hbar\omega_c$ and $e\phi_{ab}$ values.

In the limit $\hbar\omega_c \ge e\phi_{ab}$, the two-dimensional region is occupied predominantly by a single channel characterized by an integer filling factor (integer-factor channel). The properties of this system were described in a general form in [5] and, in more detail, in [1]. The electrostatic potential distribution over the cross-section of the central integer-factor channel in this case is described by the following function

$$\varphi(x) \propto (a^2 - x^2)^{3/2}, \quad -a \le x \le +a; \quad (2)$$

where $2a < 2w$ is the width of the incompressible band. The maximum value of this width for the electron density described by equation (1) is determined by the relation

$$(a_{\max}/w)^3 = 3\pi\hbar\omega_c/2W, \quad W = e\phi_{ab}, \quad (3)$$

where ω_c is the cyclotron frequency. It should be noted that the band width is sensitive to the magnetic field and varies from zero, when the band arises, to the critical dimension given by (3), when the maximum of potential (2) at the channel center reaches a value of $\hbar\omega_c$ with increasing magnetic field, after which the band bifurcates (see [5] for details of this process).

In the limit $\hbar\omega_c \ll W$, a large number of incompressible strips can form, so that equations (2) and (3) become inapplicable. Adequate formalism is necessary that would allow for the presence of numerous strips and their interaction with each other. Such a description can be realized taking into account that there is the potential difference $\hbar\omega_c$ between the boundaries of each band. Therefore, a local value of the electrostatic potential for the system involving a large number of bands can be constructed in the form

$$e\varphi(x) \simeq \hbar\omega_c \nu(x), \quad \nu(x) = \pi l_H^2 n(x); \quad (4)$$

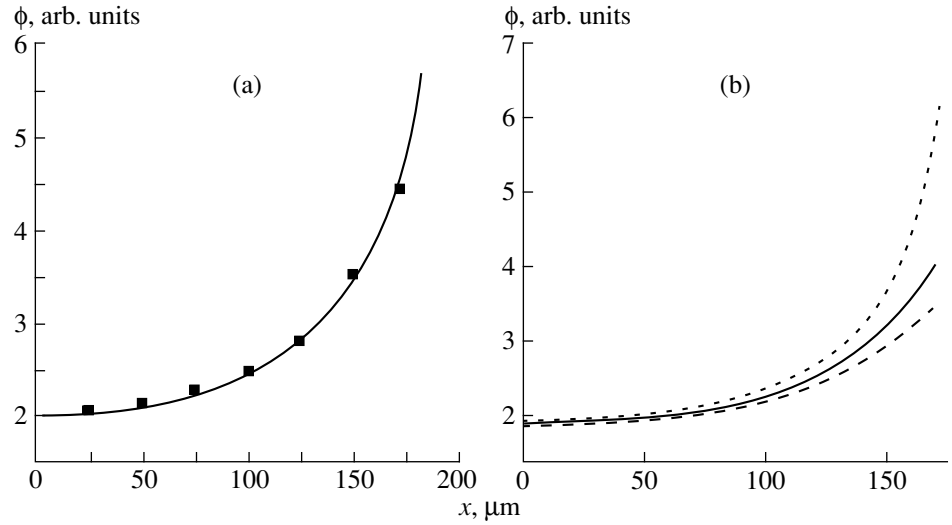

Fig. 1. The potential function according to equations (4) and (5): (a) coordinate profiles for R = 50 μm, w = 250 μm (solid curve) and the experimental data from [4] (black squares); (b) sensitivity with respect to variations of the radius R for the points with R = 75 μm (dotted curve), 50 μm (solid curve), and 5 μm (dashed curve).

where $\nu(x)$ is the local filling factor and l_H is the magnetic length.

According to relation (4), the electrostatic potential reproduces, on the average, local behavior of the electron density in the limit $\hbar\omega_c \ll W$. Formula (4), as well as expression (1), loses sense near the boundaries $\pm w$, where the excess electron density diverges.

Let us analyze, on the basis of formulas (2)–(4), the experimental data [3, 4] available on the equilibrium $\varphi(x)$ distribution in the Corbino discs and rectangular samples. The most intriguing result of these measurements is the substantial difference in behavior of the equilibrium quantity $\varphi(x)$ over the sample cross-section in the normal state and in an intermediate state, where the system includes the channels with an integer filling factor. In the normal state, as would be expected, $\varphi(x)$ = const along the 2D system under consideration. In the intermediate state, including one or more integer-factor channels, the relative $\varphi(x)$ value decreases as the center of the section is approached. It should be noted that data available on the intermediate state do not give absolute $\varphi(x)$ values and only indicate that this quantity vary in a nonmonotonic manner.

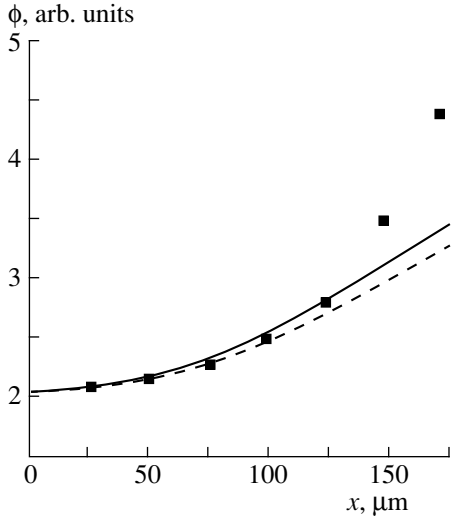

Fig. 2. The plots of $\phi(x)$ (5), (2) for R = 50 μm and a = 230 μm (solid curve), 250 μm (dashed curve).

The most interesting results presented in Fig. 9 in [3] indicated that the $\varphi(x)$ distribution over the cross-section of a Hall sample in the intermediate state is inhomogeneous. Unfortunately, the results presented in Fig. 9 in [3] were measured with uncertainties hindering their interpretation: an asymmetry is clearly observed that is apparently caused by the effect of neighboring channels; moreover, the cross-section was chosen for the convenience of experimental realization and occurred at a small, poorly determined distance from the end of the 2D system, which complicates the description of details in the $\varphi(x)$ behavior.

Information for the Corbino disc is more clear. Figures 1 and 2 show the multichannel (4) and single-channel (2) variants of the $\varphi(x)$ distribution as compared to data from [4]. Theoretical curves for the $\varphi(x)$ distribution were plotted by the algorithm

$$\phi(x) = \frac{1}{2R}\int_{x-R}^{x+R}\varphi(s)ds, \qquad (5)$$

where R is the radius of the laser beam used in experiments [3, 4]. The curves are normalized to the minimum $\phi(0)$ and fitted to the experimental points by varying R and geometric dimensions appearing in expres-

sions (2) and (4). In particular, the solid line in Fig. 1a was derived for the values $R = 50$ μm and $w = 250$ μm. Figure 1b illustrates the effect of the laser beam radius on the $\phi(x)$ behavior. Figure 2 demonstrates the same points as fitting to function (5) with $\varphi(x)$ from (2) with two different a values and $R = 50$ μm.

It should be noted that we had to scan Figs. 1 and 2 from [4] to obtain experimental points presented in Figs. 1 and 2. Then, using Fig. 9 from [3] (identical to Fig. 1 from [4]), we recalculated the data derived by scanning Fig. 2 from [4] to obtain the corresponding values for $\phi(x)$.

In summary, we conclude that $\varphi(x)$ described by equation (4) (see Fig. 1) provides better description of experimental data [4]. However, for more reliable conclusions about different variants of the $\varphi(x)$ distribution, the nonmonotonic behavior of this distribution has to be assessed that cannot be done, at least currently, based on the results of measurements under equilibrium conditions.

2. The scale of the nonmonotonic variations we are interested in, characterized by the absolute value of the electrostatic dip in Figs. 1 and 2, can be estimated in experiments involving the state with transport current. In this case, an additional energy parameter—the pulling potential V—and, along with it, new diagnostic possibilities appear that are particularly clear in the problem treating the Corbino disc.

Calculations pertaining to the electric aspect of the problem involving the presence of the transport current requires specific clarification. There are several methods of such calculations, each using its own approximation.

In the case when $\sigma_{xx} \neq 0$, the calculation starts from the condition $\mathrm{div}\mathbf{j} = 0$ that is reduced (by using the Ohm law) to an equation for the function $\varphi(x, y)$ with the boundary conditions allowing to match the potential values in the normal and integer-factor regions. Until now, the problem in this formulation has not been solved.

In the case when $\sigma_{xx} = 0$, which is reasonable for the quantum Hall effect, the condition $\mathrm{div}\mathbf{j} = 0$ degenerates and we have to search for other relations between functions $\varphi(x, y)$ and $\delta n(x)$ that can provide, along with the Poisson equation, closed formulation of the electrostatic problem. An example of such a solution independent of σ_{xx} was presented in [6]. In this study, we propose a contact approximation, which is a simple generalization of the approach proposed in [1], to the solution of the problem formulated. In this approximation, the electron density distribution over the cross-section of a 2D system including the contact with electrodes takes into account the effects of both the contact potential difference and the pulling potential. Using this distribution, it is easy to obtain the $\varphi(x)$ distribution by using formula (4), provided the condition $eV \gg \hbar\omega_c$ is fulfilled.

By definition,

$$\delta n(x) = \frac{1}{4\pi e^2}\left(\frac{\partial\psi}{\partial z}\bigg|_{+0} - \frac{\partial\psi}{\partial z}\bigg|_{-0}\right), \tag{6}$$

$$\psi(x, z)|_{z\to 0} = \begin{cases} 0, & -\infty \le x \le -w \\ W, & -w \le x \le +w \\ eV, & +w \le x \le +\infty, \end{cases} \tag{7}$$

where $W \equiv e\phi_{ab}$. Using the known solution to the Dirichlet problem (7) and calculating the derivatives entering into (6), we obtain the expression

$$\delta n(x) = \frac{w(2W - eV) - eVx}{2\pi^2 e^2 (w^2 - x^2)}. \tag{8}$$

In the limit $V \longrightarrow 0$, expression (8) transforms into equation (1). Expression (8) has a characteristic maximum at the point x_m that is determined from the relation

$$\frac{|x_m|}{w} = \left(\frac{2W}{|eV|} - 1\right) - \sqrt{\left(\frac{2W}{eV} - 1\right)^2 - 1}. \tag{9}$$

This relation rewritten in terms of $W/|eV|$ acquires the form

$$(2W/|eV| - 1) = (\xi_m^2 + 1)/2\xi_m, \quad \xi_m = x_m/w. \tag{9a}$$

Taking into account that $\xi_m \le 1$, it is easy to see that formulas (9) and (9a) are applicable only in the region $(2W/|eV| - 1) \ge 1$. This artificial restriction is due to the divergence of (8) near the points $\pm w$.

The maximum in the $\varphi(x)$ distribution was observed in the experiment. Data [3] demonstrate that $x_m/w \simeq 0.8$ at $eV \simeq 0.3$ eV. In this case, relation (9a) yields $W \simeq |eV|$. The $\hbar\omega_c$ value is of the order of 100 K and, therefore, the condition $W \gg \hbar\omega_c$ is undoubtedly fulfilled that makes it possible to use local relation (4) between density (8) and the electrostatic potential observed.

Thus, we propose a method for the description of inhomogeneous 2D electron systems which, being exposed to a magnetic field, contain a large number of integer-factor channels. Averaged description of this system leads to the conclusion that the observed electrostatic potential is proportional to the inhomogeneous sample density (see formula (4)). In cases when the transport current is present, the model explains the observed position of maximum of the electrostatic potential inside the 2D sample.

ACKNOWLEDGMENTS

This work was supported in part by the Russian Foundation for Basic Research, project no. 98-02-16640.

REFERENCES

1. V. B. Shikin and N. I. Shikina, Pis'ma Zh. Éksp. Teor. Fiz. **62**, 879 (1995) [JETP Lett. **62**, 894 (1995)].
2. P. F. Fontein, P. Hendriks, F. A. P. Bloom, *et al.*, Surf. Sci. **263**, 91 (1992).
3. R. Knott, W. Dietsche, K. von Klitzing, *et al.*, Semicond. Sci. Technol. **10**, 117 (1995).
4. W. Dietsche, K. von Klitzing, and K. Ploog, Surf. Sci. **361/362**, 289 (1996).
5. D. B. Chklovskiĭ, B. I. Schklovskiĭ, and L. I. Glazman, Phys. Rev. B **46**, 4026 (1992); D. B. Chklovskii, K. F. Matveev, and B. I. Schklovskiĭ, Phys. Rev. B **47**, 12605 (1993).
6. A. H. MacDonald, T. M. Rice, and W. F. Brinkman, Phys. Rev. B **28**, 3648 (1983).

Translated by R. Tyapaev

JETP Letters, Vol. 71, No. 2, 2000, pp. 69–71. Translated from Pis'ma v Zhurnal Éksperimental'noĭ i Teoreticheskoĭ Fiziki, Vol. 71, No. 2, 2000, pp. 100–103.

CONDENSED MATTER

Phononless Thermal Conduction in Glasses at Ultralow Temperatures

Yu. Kagan, L. A. Maksimov, and I. Ya. Polishchuk

Russian Research Center Kurchatov Institute, pl. Kurchatova 1, Moscow, 123182 Russia

Received December 10, 1999

Abstract—It is shown that the thermal conduction in dielectric glasses at ultralow temperatures is provided by energy transfer over the infinite cluster of resonance pairs of two-level systems. Expressions for the phononless thermal conductivity coefficient ($\sim T^{4/3}$) and for the temperature of crossover between the phonon and phononless mechanisms of thermal conduction are obtained. The possibility of experimental corroboration of the results obtained is discussed. © *2000 MAIK "Nauka/Interperiodica".*

PACS numbers: 66.70.+f; 61.43.Fs

1. It is known that the anomalous properties of dielectric glasses in the region of temperatures below 1 K can be quite reasonably described within the model of tunneling two-level systems (TLSs) [1]. It is essential that TLSs were considered in [1] to be noninteracting with each other. Experimental results in the region of temperatures down to 100 mK were quite reasonably explained using this model of the dielectric glass [2]. However, taking into account the interaction of TLSs with phonons is already necessary for an understanding of, for example, sound relaxation. This interaction is necessarily gives rise to an indirect interaction between TLSs depending on the distance as R^{-3} [3]. The R^{-3} character of this interaction and spectral diffusion associated with this law make it possible to explain the quadratic temperature dependence experimentally observed for the transverse relaxation rate of TLSs $\tau_2^{-1} \sim T^2$ [2]. It has been long believed that spectral diffusion is the only manifestation of the interaction between TLSs. However, in recent years, it has been shown both experimentally [4] and theoretically [5, 6] that this interaction leads to the formation of a new branch of collective low-energy excitations. Therefore, along with one-phonon relaxation, a TLS can relax as a component of the collective mode mentioned above.

In fact, the scenario of this relaxation appears as follows: The dipole–dipole character of the interaction gives rise to the formation of strongly bound pairs of TLSs. At low temperatures, when phonons are virtually frozen out, the bound state of a pair represents a coherent formation with its own excitation spectrum for a long period of time. This excitation spectrum contains a low-energy (as compared with the temperature of the system) mode. The bound pairs, in their turn, also interact with each other by the R^{-3} law. Therewith, low-energy excitation can be transferred among pairs of TLSs [5, 6]. Taking into account this relaxation channel revealed peculiar features of the behavior of dielectric glasses at ultralow temperatures (linear temperature dependence of the coefficient of internal friction [5], phase-memory loss rate [6], and nuclear relaxation rate [7]).

This work is devoted to calculating the thermal conductivity associated with the phononless mechanism of the transport of elementary excitations at ultralow temperatures described above.

2. An isolated TLS is described by the standard pseudospin Hamiltonian

$$h = -\Delta S^z - \Delta_0 S^x. \tag{1}$$

In this case, the distribution function $P(\Delta, \Delta_0)$ of the level mismatch Δ and the tunneling transition amplitude Δ_0 is commonly described by the equation [1]

$$P(\Delta, \Delta_0) = \frac{\bar{P}}{\Delta_0}. \tag{2}$$

Relaxation in glasses within the temperature range 0.1–1 K is mainly associated with thermal TLSs, for which

$$\Delta \simeq \Delta_0 \simeq T, \tag{3}$$

and the excitation energy $E = \sqrt{\Delta_0^2 + \Delta^2} \simeq T$. The concentration c_T of such TLSs equals

$$c_T = (\bar{P}/T). \tag{4}$$

The one-phonon relaxation rate of such TLSs (the reciprocal of the lifetime) is given by the equation [2]

$$\tau_{ph}^{-1} = U_0/\hbar(T/\hbar v)^3, \tag{5}$$

and

$$U_0 = \gamma^2/\rho v^2, \tag{6}$$

where γ is the constant of deformation interaction between a TLS and a phonon, ρ and v are respectively

0021-3640/00/7102-0069$20.00

the sound density and velocity in the glass. The indirect interaction between TLSs (caused by their interaction with phonons) can be written as [3]

$$\hat{V} \simeq U(R_{ij})S_i^z S_j^z, \quad U(R_{ij}) \simeq U_0(a/R_{ij})^3, \tag{7}$$

where a is the average distance between TLSs. It is found empirically for dielectric glasses that $\bar{P}U_0$ is a small parameter.

3. Any pair of TLSs located at a distance of R from each other can, generally speaking, occur in one of the four states (+ –), (– +), (+ +), and (– –). The signs + and – correspond to the excited and ground states of a TLS. The transition probability amplitude between the states of the flip–flop configuration (+ –) and (– +) is given by the expression [5]

$$\Delta_{0p}(R) \approx U_0/R^3 \frac{\Delta_0\Delta_0'}{EE'}. \tag{8}$$

Because the existence of the flip–flop configuration is associated with the occurrence of an excited TLS, it is evident that such pairs are mainly composed of thermal TLSs (see (3)). Note in addition that the transition amplitude (8) attains its maximum value U_0/R^3 (at a given distance), because $\Delta_0 \sim E \sim T$ for such pairs. In [5, 6], it is shown that the transition amplitude that links the states of the flip–flop configurations of two thermal TLSs with any of the remaining two states (+ +) and (– –) is small if

$$\Delta_{0p}(R) \simeq U_0/R^3 \ll T. \tag{9}$$

Therefore, if condition (9) is fulfilled, only transitions between the states of the flip–flop configuration should be considered. Thus, such a pair of TLSs is in essence a two-level system of a new type described by the Hamiltonian of the type (1). The level mismatch is $\Delta_p = |E - E'|$, the tunneling amplitude Δ_{0p} is determined by expression (8), and the transition energy in the pair is $E_p = \sqrt{\Delta_p^2 + \Delta_{0p}^2}$. It is essential that, as distinct from the standard model, the parameters of pairs are distributed by the law [5]

$$P^{(2)}(\Delta_p, \Delta_{0p}) \simeq (\bar{P}T)(\bar{P}U_0)/\Delta_{0p}^2. \tag{10}$$

From quantum mechanics, it is known that the probability of a quantum-mechanical (reversible) transition in a two-level system is a maximum if the level mismatch is of the order of the tunneling amplitude (such a two-level system is named resonance system). As applied to pairs of TLSs, this means that $\Delta_p \sim \Delta_{0p} \sim E_p$. The density of such resonance pairs with a characteristic value of tunneling parameters distributed in the band $E_p(1 - \zeta)$–$E_p(1 + \zeta)$ (where a certain dimensionless parameter $\zeta \leq 1$) up to a factor of $\ln \zeta$ equals [5]

$$n_* \simeq (\bar{P}T)(\bar{P}U_0) \tag{11}$$

and does not depend on the band, that is, on the chosen value of E_p. This parameter determines the average distance $R_* \simeq n_*^{-1/3}$ between pairs of the band under consideration and, hence, the characteristic interaction energy $E_* = U/r_*^3 = Un_*$. Of two resonance pairs that belong to a certain band E_p, a new formation can be composed in its turn (actually, containing of four TLSs), and the notion of flip–flop configuration can be introduced for this formation. This, in particular, allows two resonance pairs to be considered as a two-level system with the level mismatch of order E_p and the tunneling amplitude E_*. Similar to the TLS and the resonance pair, the quantum-mechanical transition amplitude in the last case is not small when two resonance pairs are in resonance with each other, that is, when $E_p \sim E_*$. By the order of magnitude, the rate of quantum-mechanical oscillations in this case equals $E_*/\hbar$. At the same time, the resonance pairs under consideration with the same energy E_* interact with a macroscopic number of pairs of the same energy band E_*. Therefore, in fact, relaxation occurs rather than quantum-mechanical oscillations. Relaxation in this case is associated with irreversible exchange by excitations of order E_* between two resonance pairs at the rate $\tau^{-1} \simeq E_*/\hbar$. Note that this process takes place only in the case when the one-phonon relaxation determined by equation (5) is not more efficient. It is shown in [5] that the one-phonon relaxation of TLSs is suppressed if

$$T < T_0 = (\bar{P}U_0)\sqrt{\hbar^3 v^3/U_0}, \tag{12}$$

and the effects considered in this work can take place only at a temperature $T < T_0$.

4. In the case of the relaxation under consideration, excitation transfer among resonance pairs proceeds for a distance R_* in a time τ_*. Therefore, this process can be related to diffusion with the coefficient equal to $D_* = R_*^2\tau_*^{-1}$.

The energy density associated with the diffusing excitations under consideration is $\varepsilon_* = E_*n_*$. Correspondingly, the thermal conductivity is $c_* \simeq 2(PT)(\bar{P}U_0)^3$. From here, the thermal conductivity coefficient associated with the relaxation mechanism considered above can be estimated as follows:

$$\kappa_* \approx \frac{2T}{3\hbar}(\bar{P}T)^{1/3}(\bar{P}U_0)^{13/3}. \tag{13}$$

Compare this expression with the coefficient of phonon thermal conductivity, which is conditioned by the scattering of phonons by thermal TLSs [2]

$$\kappa_{ph} = \frac{v}{2\pi(\bar{P}U_0)a^2}\left(\frac{T}{\Theta_D}\right)^2. \tag{14}$$

At low temperatures, the proposed mechanism of thermal conduction described by expression (13) is charac-

terized by a weaker temperature dependence and, therefore, may turn out more efficient.

Crossover, that is, a change in the mechanism of thermal conduction, takes place under the condition $\kappa_* = \kappa_{ph}$ and must be observed at the temperature

$$T_* = \Theta_D(2\pi)^{3/2}(\bar{P}a_0^3\Theta_D)^{1/2}(\bar{P}U_0)^8. \quad (15)$$

Note that the restriction on the temperature connected with condition (12) is unimportant for the observation of relationship (13), because the condition $T_* < T_0$ is always fulfilled.

Thus, the phononless mechanism of thermal conduction can be observed only if the factor $(\bar{P}U_0)$ is not too small. In dielectric glasses such as, for example, Suprasil, this parameter is so small ($\sim 10^{-3}$) that T_* turns out to be considerably lower than 1 mK. At the same time, we demonstrated [8] that thermodynamic and relaxation properties of Fermi glasses (Anderson dielectrics) can be described within the model of interacting two-level systems. Therefore, all the results obtained for dielectric glasses are applicable to Fermi glasses. Note that the parameter $(\bar{P}U_0)$ can become relatively large in the vicinity of the dielectric–metal transition point, and the crossover temperature will shift toward the region of temperatures that can be reached experimentally.

ACKNOWLEDGMENTS

This work was supported by the Russian Foundation for Basic Research, project no. 98-02-1629, the Ministry of Education of the Russian Federation within the program of support for basic research in natural science, project no. 97-0-14.0-80, and the INTAS program, project no. IR-97-1066.

REFERENCES

1. P. W. Anderson, B. I. Halperin, and C. M. Varma, Philos. Mag. **25**, 1 (1972); W. A. Phillips, J. Low Temp. Phys. **7**, 351 (1972).
2. S. Hunklinger and A. K. Raychaudhari, Prog. Low Temp. Phys. **9**, 267 (1986).
3. J. Joffrin and A. Levelut, J. Physique **36**, 811 (1975).
4. D. Osheroff, S. Rogge, and D. Natelson, Czech. J. Phys. **46** (S6), 3295 (1996).
5. A. L. Burin and Yu. Kagan, Zh. Éksp. Teor. Fiz. **107**, 633 (1995) [JETP **80**, 761 (1995)].
6. A. L. Burin, Yu. Kagan, L. A. Maksimov, and I. Ya. Polishchuk, Phys. Rev. Lett. **80**, 2945 (1998).
7. Yu. Kagan, L. A. Maksimov, and I. Ya. Polishchuk, Zh. Éksp. Teor. Fiz. **115**, 1 (1999) [JETP **88**, 1236 (1999)].
8. Yu. Kagan, L. A. Maksimov, and I. Ya. Polishchuk, Physica B, 2000 (in press).

Translated by A. Bagatur'yants

JETP Letters, Vol. 71, No. 2, 2000, pp. 72–75. Translated from Pis'ma v Zhurnal Éksperimental'noĭ i Teoreticheskoĭ Fiziki, Vol. 71, No. 2, 2000, pp. 104–109.

CONDENSED MATTER

Heating of Vibrational States of Adatoms by the Current of a Scanning Tunneling Microscope

M. V. Grishin, F. I. Dalidchik, S. A. Kovalevskiĭ, and N. N. Kolchenko

Semenov Institute of Chemical Physics, Russian Academy of Sciences, ul. Kosygina 4, Moscow, 117977 Russia

Received December 14, 1999

Abstract—Effects associated with the vibrational heating of adatoms by the current of inelastically tunneling electrons were detected in spectroscopic experiments with a scanning tunneling microscope. A relation between the envelope curves of autoemission resonances and the vibrational distribution of particles located under the tip was ascertained. © *2000 MAIK "Nauka/Interperiodica".*

PACS numbers: 61.16.Ch; 7320-r

Unimolecular chemical reactions both in a gas phase and on a solid surface often proceed through the mechanism of activated overbarrier transition [1]. Rate constants k of such processes essentially depend on the particle distribution over the vibrational levels of the selected bond in the vicinity of the activation barrier

$$k \sim f(v_a). \quad (1)$$

Here, $f(v)$ is the vibrational distribution, v is the vibrational quantum number, $E(v_a) \approx E_a$, $E(v)$ is the vibrational energy, and E_a is the activation barrier.

The IR dissociation of molecules, photodesorption, and many other activated unimolecular processes are well understood at present. Nonequilibrium distributions of macroscopic ensembles of particles participating in these processes are commonly determined by direct spectroscopic methods (for example, optical [2]). In recent years, unimolecular chemical transformations have come to be studied at a level of single events with a spatial resolution of several angstroms using scanning tunneling microscopy (STM). It was found that the probabilities of the desorption [3] and dissociation [4] of adsorbed particles and their transfer between the surface and the tip [5] depend nonlinearly on the tunneling currents

$$k_{\mathrm{STM}} \sim J^n, \quad n = n(V) > 1 \quad (2)$$

where J is the current, and V is the voltage across the tunneling contact.

Relationships (2) evidently indicate that the activation of vibrational degrees of freedom of adatoms by the current of inelastically tunneling electrons is of significant importance. Correspondingly,

$$k_{\mathrm{STM}} \sim f(v_a, J, V). \quad (3)$$

In a number of works (see, for example, [6, 7]), it was shown that, with the activation and relaxation parameters properly selected, the rate models that take into account one-quantum transitions ($|\delta v| = 1$) reproduce experimental dependences of k_{STM} on J and V; that is, the distribution $f(v, J, V)$ can be indirectly evaluated by fitting the rate model. However, direct methods of reconstructing these distributions that will be similar to methods of probing macroscopically large ensembles of particles [2] are not available at present. In spectroscopic experiments with a scanning tunneling microscope, the heating of vibrational degrees of freedom of adsorbed particles has not been observed yet.

The goal of this communication is to justify and test the possibility of determining nonequilibrium distributions of adatoms located under a tip by the envelope curves of vibrational spectra measured with a scanning tunneling microscope operating in the autoemission mode. We will present the results of experiments that revealed spectroscopic effects associated with the heating of vibrational degrees of freedom of adsorbed particles by the current of inelastically tunneling electrons.

The experiments were performed on an ultrahigh-vacuum installation equipped with an Omicron scanning tunneling microscope, which was used for measuring $J(V)$ dependences at the Al(100) surface containing adsorbed oxygen [8, 9]. The procedure of spectroscopic measurements performed at selected points of the surface was described previously [10, 11]. The procedure of surface preparation involved cycles of ionic etching (Ar^+, 500 eV) and prolonged heating in a vacuum ($P \le 10^{-9}$ Torr, $T = 650$ K). After purification, the $J(V)$ dependences had the form of typical autoemission curves

$$J(V) \sim \exp(-C/V), \quad C \approx 100 \text{ V} \quad (4)$$

at almost all points of the surface. (Below, the tip polarity is always negative).

Dosed adsorption of oxygen resulted in significant changes in the J–V curves. Already at an exposure of ~10–20 L, some J–V curves exhibited long series of

equidistant maximums, as exemplified in Figs. 1–3. In some cases, the number of maximums in the available range of measuring V (up to 10 V) reached several dozens. In the majority of cases, the distances δ between the neighboring maximums corresponded to the energy $\delta E_1 = e\delta V_1 = 0.11$–$0.12$ eV. Spectra with $\delta E_2 = 0.07$–0.08 eV occurred more rarely. Spectra with the same value of δE can differ in the shape of the envelope curve. Figures 1–3 display examples of three characteristic types of the envelope curves: bell-shaped (Fig. 1), monotonically growing (Fig. 2), and ascending with oscillations (Fig. 3). The number of groups of resonance lines in the spectra of the third type varied (spectra with two, three, and more groups of lines occurred).

As the exposure increased, the spectral features exhibited significant changes. At an exposure of ~ 50 L, spectra with $\delta E_3 = 0.04$ eV appeared. If the exposure was further increased, the number of points at the surface at which spectra contained lines with large values of δE decreased, and the number of spectra with $\delta E = \delta E_{2,3}$ increased. The amplitudes of resonance maximums significantly increased with increasing exposure. At large exposures (~1000 L), long series of resonances with $\delta E_3 = 0.04$ eV were observed in the J–V curves at almost all points of the scanned areas. These resonances had growing and oscillating envelope curves.

The initial stages of aluminum oxidation at room temperatures were intensively studied in recent years by the STM [12] and HREELS [13] methods. It is known presently that, at exposures of ~ 10–20 L (300 K), the adsorbed oxygen is grouped into small clusters with characteristic values of vibrational quanta $\hbar\omega_1 = 0.11$–0.12 eV, $\hbar\omega_2 = 0.07$–0.08 eV, and $\hbar\omega_3 = 0.036$ eV [13].

The agreement of δE_i (i = 1, 2, 3) with the known values of vibrational quanta for the oxygen adsorbed on Al(100) and the equidistance of a great number of resonance lines in the J–V curves suggest the conclusion that the spectra shown in Figs. 1–3 correspond to multiquantum vibrational transitions of clusters differing in activation and relaxation conditions.[1]

The mechanism of the formation of vibrational series in the J–V curves of a scanning tunneling microscope operating in the autoemission mode (that is, at voltages $eV > \phi$, ϕ is the work function of the tip) was described in [14, 15]. These features are due to the delay of tunneling electrons in the nanoscale resonator formed by the tip ($V_t < 0$) and the surface containing adsorbed particles [15].

[1] The estimate of the sticking coefficient of oxygen to the surface that can be made by the number of points with resonance lines (10% at 10–20 L) gives a value of ~ 0.005–0.01. The same values were obtained in [12] by the results of topographic measurements.

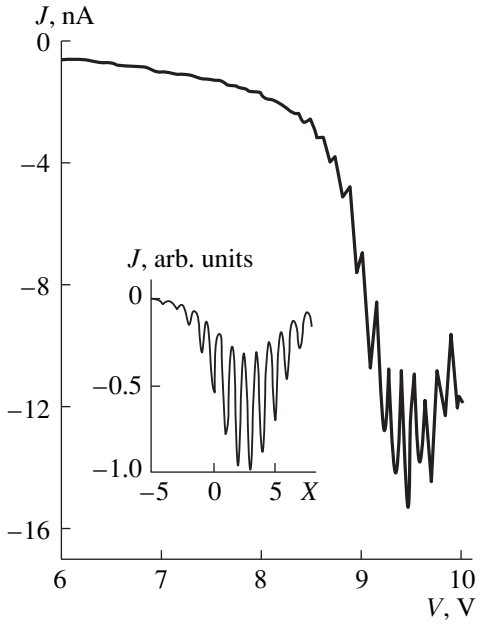

Fig. 1. Vibrational spectrum of oxygen adsorbed on Al(100), 20 L, 300 K, $\hbar\omega = 0.12$ eV. The inset shows the results of calculations of the function $J(X)$ by equations (9)–(12), $X = (eV - \delta E_0)/\hbar\omega$, $\Gamma/\hbar\omega = 0.04$; $\alpha = 2$, the distribution $f(\nu)$ is of the Boltzmann type, $\nu = 1.5$ (an example of bell-shaped envelope curves).

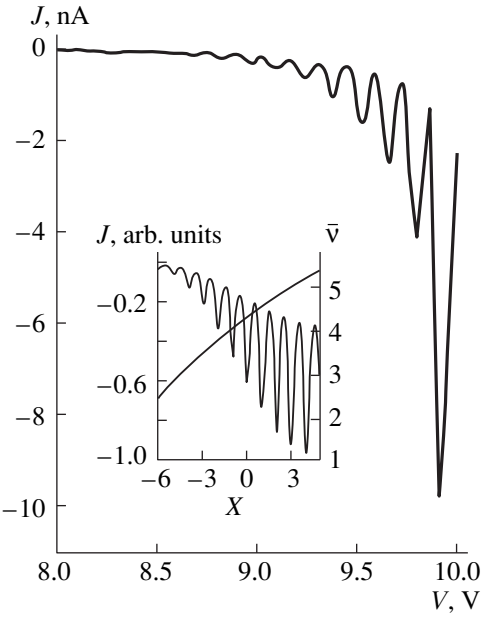

Fig. 2. The same as in Fig. 1. The inset shows the results of calculations for a linear approximation of the dependence of $\bar{\nu}$ on V (an example of monotonically growing envelope curves).

The resonator size along the normal is

$$l \sim \frac{eV - \phi}{eV} d \sim 5 \text{ Å} \qquad (5)$$

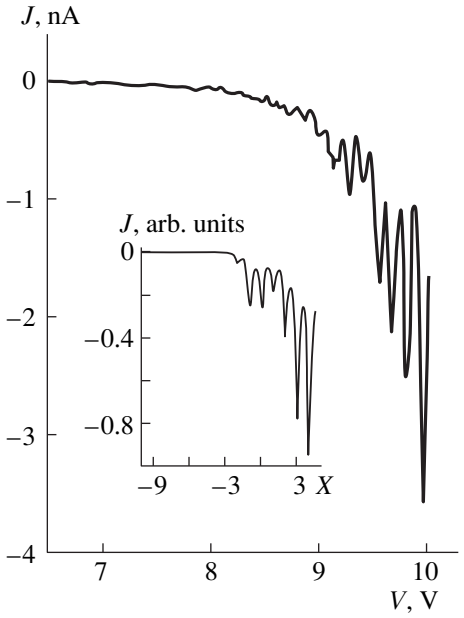

Fig. 3. The same as in Figs. 1 and 2, but with the envelope curve of the oscillating type. The inset shows the results of calculations for the distribution $f(v) = N\exp(-1.4(v-1)^2)$.

(d is the distance between the tip and the surface). The resonator volume estimated by the value of the exchange splitting observed for paramagnetic adsorbed particles makes up $\sim 10^2$ Å^3 [14].

In the case of a prolonged delay of electrons in the resonator ($\Gamma < \hbar\omega$, $\Gamma = \hbar/\tau$, τ is the delay time), the transitions of electrons from the tip to the sample are carried out by the formation and decay of intermediate quasistationary states $|n, \tilde{v}\rangle$, whose energies are [10]

$$E_{n,\tilde{v}}(V, d) = -eV + E_n^0(V, d) + \hbar\tilde{\omega}(\tilde{v} + 1/2), \quad \tilde{v} = 0, 1, 2, \ldots \tag{6}$$

Here, E_n^0 are electron energy levels in the resonator, $\hbar\tilde{\omega}$ is the vibrational quantum of an adsorbed particle interacting with an electron captured at the nth level of the resonator.

At electron energies E close to $E_{n\tilde{v}}^0(V, d)$,

$$\left|E - E_{n\tilde{v}}^0(V, d)\right| < \Gamma \le \hbar\omega, \tag{7}$$

the tunneling contact becomes more transparent: the probabilities of transitions, including inelastic ones, increase exponentially [16]. This results (because of the dependence of $E_{n\tilde{v}}$ on V) in the formation of series of equidistantly separated features. These features for tips with the electron density

$$\rho(E) \approx \rho_0 \frac{\gamma^2}{(E - E_t)^2 + \gamma^2}, \quad E_t < E_F \tag{8}$$

(E_F is the Fermi level) take the form of resonance maximums [14, 15]. At $\alpha\delta\omega < \Gamma$ (α is the vibronic coupling parameter), which corresponds to experimental results, the series of resonance maximums in the J–V curves are adequately described within the harmonic model of vibrations by the equations

$$J(V) = J_0 \sum_k \Omega_k(V, J) F_k(V). \tag{9}$$

Here,

$$J_0(V) = J_0 \exp\left(-\frac{4\sqrt{2}\phi^{3/2} d}{3V}\right), \quad J_0 = \text{const}, \quad e = \hbar = m = 1; \tag{10}$$

$$F_k(V) = ((\delta E_0 + \omega k - V)^2 + \Gamma^2)^{-1}, \quad k = 0, \pm 1, \ldots, \quad \delta E_0 = E_n^0(V, d) - E_t \approx \text{const}; \tag{11}$$

$$\Omega_k(V, J) = \sum_v f(v, V, J) \langle v | v + k \rangle^2 \tag{12}$$

is the envelope curve of resonance lines located at voltages

$$V_k = \delta E_0 + \omega k, \quad e = \hbar = m = 1, \tag{13}$$

which contains information on the distribution $f(v, V, J)$. (To derive equations (9)–(12), it is sufficient to take into account the contributions of excited states in equation (6) of [15] and to pass from the summation over v to the summation over $n = \tilde{v} - v$).

An analysis of equation (12) and the results of numerical calculations indicate that three types of distributions $f(v, V, d)$ correspond to three various types of envelope curves observed in the experiments (see Figs. 1–3). For distributions of the Boltzmann type

$$f(v, V, J) = N \exp\left(-\frac{v}{\bar{v}(V, J)}\right), \quad N^{-1} = \bar{v}, \quad \bar{v} > 1, \tag{14}$$

$$\Omega_n = (2\sigma(V, J))^{-1/2} \exp\left(-\frac{(n - \alpha)^2}{2\sigma^2(V, J)}\right), \tag{15}$$

$$\sigma^2(V, J) = 2\alpha\bar{v}(V, J). \tag{16}$$

According to (15), the envelopes at $\sigma = \text{const}$ take the form of symmetric bell-shaped curves, exemplified in Fig. 1. The dependence of $\sigma_n(V, J)$ on V ($\partial\sigma/\partial V > 0$, $J = J(V)$, $d = \text{const}$) is manifested by an extension of the wing of the envelope curve corresponding to lower values of V. If the J–V relationships are measured within a restricted voltage range, the envelope curves appear to be monotonically growing.

For strongly nonequilibrium distributions $f(v, V, J)$,

for example, for

$$f(v, V, J) = N\exp\left(-\frac{(v - v_0(V, J))^2}{\Delta}\right), \quad (17)$$

$$\Omega_n \sim |\langle v_0(V, J)|n\rangle|^2. \quad (18)$$

In this case, the envelope curves oscillate and single out groups of resonance maximums in the *J–V* curves (see Fig. 3). At v_0 = const, $\alpha > 1$, the number of such groups equals $v_0 + 1$.

The direct observation of the nonequilibrium vibrational heating of adatoms in the STM experiments and the relation between the envelope curves of resonance spectra and the distributions $f(v, V, J)$ ascertained above open up fresh opportunities for studying mechanisms of fundamental heterogeneous processes (dissociation, desorption, chemical reactions, vibrational relaxation, etc.) with nanoscale and subnanoscale spatial resolution. Direct spectroscopic measurements like those underlying the kinetic spectroscopy of molecular hot bands [17] become available now.

ACKNOWLEDGMENTS

This work was supported by the Russian Foundation for Basic Research, project no. 99-03-32098a.

REFERENCES

1. P. J. Robinson and K. A. Holbrook, *Unimolecular Reactions* (Wiley-Interscience, London, 1972).
2. *Laser Spectroscopy of Vibrationally Excited Molecules*, Ed. by V. A. Letokhov (Nauka, Moscow, 1990).
3. I.-W. Lyo and Ph. Avouris, J. Chem. Phys. **93**, 4479 (1990).
4. B. Stipe, M. Rezaei, W. Ho, *et al.*, Phys. Rev. Lett. **78**, 4410 (1997).
5. D. Eigler, C. Lutz, and W. Runge, Nature **352**, 600 (1991).
6. S. Gao, M. Persson, and B. Lundqvist, Phys. Rev. B **55**, 4825 (1997).
7. G. Salam, M. Persson, and R. Palmer, Phys. Rev. B **49**, 10655 (1994).
8. S. A. Kovalevskiĭ, F. I. Dalidchick, M. V. Grishin, and B. R. Shub, in *Book of Abstracts of Ninth International Symposium on Small Particles and Inorganic Clusters, Lausanne, Switzerland, 1998*, p. 11.
9. S. A. Kovalevskiĭ, F. I. Dalidchick, M. V. Grishin, *et al.*, in *Preliminary Proceedings of STM'99, Seoul, Korea, 1999*, p. 673.
10. F. I. Dalidchik, M. V. Grishin, S. A. Kovalevskiĭ, and N. N. Kolchenko, Pis'ma Zh. Éksp. Teor. Fiz. **65**, 306 (1997) [JETP Lett. **65**, 325 (1997)].
11. S. A. Kovalevskiĭ, F. I. Dalidchick, M. V. Grishin, *et al.*, Appl. Phys. A **66**, 51 (1998).
12. H. Brune, J. Wintterlin, J. Trost, *et al.*, J. Chem. Phys. **99**, 2128 (1993).
13. C. Astaldi, P. Geng, and K. Jakoby, J. Electron Spectrosc. Relat. Phenom. **44**, 175 (1987).
14. S. A. Kovalevskiĭ and F. I. Dalidchik, Pis'ma Zh. Éksp. Teor. Fiz. **67**, 916 (1998) [JETP Lett. **67**, 965 (1998)].
15. M. V. Grishin, F. I. Dalidchick, N. N. Kolchencko, and S. A. Kovalevskiĭ, Ultramicroscopy **79**, 203 (1999).
16. F. I. Dalidchik, Zh. Éksp. Teor. Fiz. **87**, 1384 (1984) [Sov. Phys. JETP **60**, 795 (1984)].
17. F. Dalidchik, I. Zaslonko, L. Marnasheva, and Y. Mukoseev, Chem. Phys. Lett. **143**, 55 (1988).

Translated by A. Bagatur'yants

JETP Letters, Vol. 71, No. 2, 2000, pp. 76–79. Translated from Pis'ma v Zhurnal Éksperimental'noĭ i Teoreticheskoĭ Fiziki, Vol. 71, No. 2, 2000, pp. 110–115.

CONDENSED MATTER

Direct Measurement of the Delay Time for a Neutron in a Crystal in the Case of the Laue Diffraction

V. V. Voronin, E. G. Lapin, S. Yu. Semenikhin, and V. V. Fedorov*

St. Petersburg Institute of Nuclear Physics, Russian Academy of Sciences, Gatchina, Leningrad oblast, 188350 Russia

**e-mail: vfedorov@hep486.pnpi.spb.ru*

Received December 15, 1999

Abstract—The dynamical Laue diffraction has been studied for a direct beam diffracted from a thin (~3.5 cm) α-quartz crystal at the Bragg angles close to 90°. It is shown that diffraction occurs at Bragg angles up to 87°. The time-of-flight method is used to measure the time of the neutron presence in the crystal under the diffraction conditions. The time delay for a scattered neutron inside the crystal predicted earlier for the Bragg angles close to 90° is confirmed experimentally. The effective velocity of the neutron propagation in a crystal measured at the incident-neutron velocity of 810 m/s and the diffraction angle of 87° equals (43 ± 1) m/s. The result obtained confirms the possibility of increasing, by an order of magnitude, the sensitivity of the diffraction method of determining the dipole moment of a neutron at Bragg angles close to 90° predicted earlier theoretically. © *2000 MAIK "Nauka/Interperiodica".*

PACS numbers: 61.12.Ld; 61.12Bt

1. Earlier [1–3], it was shown that a neutron propagating in a noncentrosymmetric crystal is subjected to the action of the internal crystal field with an intensity dependent on the direction of the neutron propagation and attaining the maximum value (~10^8 V/cm) for certain sets of crystallographic planes satisfying the Bragg condition. This internal field was measured experimentally from the change in the phase of the Pendellösung fringes caused by the spin flip [2, 3] for the dynamical diffraction of polarized neutrons by the {110} planes of an α-quartz crystal. The experimentally measured field intensity, $E_{(110)} = (2.10 \pm 0.12) \times 10^8$ V/cm, is in good agreement with its theoretically calculated value.

It was shown [4–6] that the fields of such intensities can be used for measuring electric dipole moments (EDM) of neutrons in the case of the Laue diffraction by a noncentrosymmetric crystal. The polarization method for determining EDM was suggested in [6–8].

It was also shown [4–6] that, at diffraction angles close to π/2, the sensitivity of the method to a neutron EDM increases by more than an order of magnitude and, in principle, can become comparable with the sensitivity of the widespread magnetic-resonance method using ultracold neutrons (the so-called UCN method) [9, 10].

Consider the physics underlying the method suggested in this study. The propagation of a neutron along directions close to those satisfying the Bragg condition for a certain set of crystallographic planes in a crystal can be described by two types of Bloch waves, $\psi^{(1)}$ and $\psi^{(2)}$ (see, e.g., [11]), formed as a result of the interaction between the neutron and the periodic nuclear potential,

$$V_g^N(\mathbf{r}) = 2V_g^N \cos(\mathbf{gr}) \tag{1}$$

of this set of planes [8], namely, by

$$\begin{aligned}\psi^{(1)} &= \frac{1}{\sqrt{2}}[\exp\{i\mathbf{k}^{(1)}\mathbf{r}\} + \exp\{i(\mathbf{k}^{(1)} + \mathbf{g})\mathbf{r}\}] \\ &= \sqrt{2}\cos(\mathbf{gr}/2)\exp[i(\mathbf{k}^{(1)} + \mathbf{g}/2)\mathbf{r}],\end{aligned} \tag{2}$$

$$\begin{aligned}\psi^{(2)} &= \frac{1}{\sqrt{2}}[\exp\{i\mathbf{k}^{(2)}\mathbf{r}\} - \exp\{i(\mathbf{k}^{(2)} + \mathbf{g})\mathbf{r}\}] \\ &= -i\sqrt{2}\sin(\mathbf{gr}/2)\exp[i(\mathbf{k}^{(2)} + \mathbf{g}/2)\mathbf{r}].\end{aligned} \tag{3}$$

Here, **g** is the reciprocal-lattice vector characterizing the given set of the crystallographic planes, $|\mathbf{g}| = 2\pi/d$, and d is the interplanar spacing.

In fact, expressions (2) and (3) describe standing waves along **g** (normal to the planes) propagating along the direction $\mathbf{k}_\parallel^{(1,2)} = k^{(1,2)} + \mathbf{g}/2$ (parallel to these planes). The small difference in the wave-vector magnitudes, $k^{(1)}$ and $k^{(2)}$, is explained by the fact that neutrons in the state $\psi^{(1)}$ are concentrated in the vicinity of the potential maximum (in the planes), whereas neutrons in the state $\psi^{(2)}$, in the vicinity of the potential minimum (between the planes)

$$k^{(1,2)^2} = K^2 \mp U_g^N,$$

where $U_g = 2mV_g^N/\hbar^2$, $K^2 = k^2 + U_0^N \equiv 2m(E + V_0^N)/\hbar^2$, and m, E, and k are the mass, energy, and the wave vec-

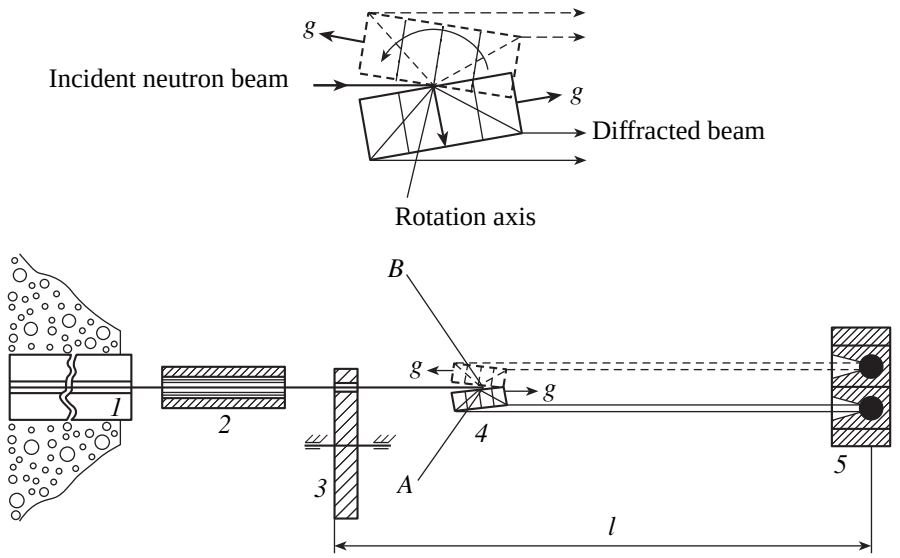

Fig. 1. Schematic of a setup for measuring time-of-flight spectra for a direct diffracted neutron beam as a function of the Bragg angle. (*1*) Interchannel neutron guide, (*2*) multislit neutron guide, (*3*) mechanical beam chopper, (*4*) $14 \times 14 \times 3.5$ cm-large α-quartz single crystal, (*5*) neutron detectors, *l* is path length, (*A*, *B*) two crystal positions corresponding to the same Bragg angle, (*g*) reciprocal-lattice vector in the (110) plane.

tor of an incident neutron, and V_0^N is the average nuclear potential of the crystal. The values of V_0^N and V_g^N are of the order of 10^{-8} eV, and therefore the thermal and the cold neutrons with the energies ranging within 10^{-1}–10^{-3} eV satisfy, with a high accuracy, the relationship $k^{(1)} \approx k^{(2)} \approx k$.[1] Thus, these waves propagate along the crystallographic planes with the velocities

$$v_{\parallel}^{(1,2)} = \hbar\left|\mathbf{k}^{(1,2)} + \mathbf{g}/2\right|/m = \hbar k^{(1,2)}\cos\Theta_B/2m \approx v\cos\Theta_B, \quad (4)$$

where $v = \hbar k/m = 2\pi\hbar/\lambda m = \pi\hbar/md\sin\Theta_B$ is the velocity of an incident neutron, Θ_B is the Bragg angle, and $\lambda = 2\pi/k$ is the wavelength of an incident neutron satisfying the Bragg conditions $\lambda = 2d\sin\Theta_B$.

It was revealed that a number of phenomena observed in the dynamical diffraction [1–13] (including the effects associated with the neutron EDM [4, 8]) are determined not by the total neutron velocity, but by its component along the crystallographic planes, $v_{\parallel} = v\cos\Theta_B$. In particular, at the diffraction angles close to $\pi/2$, the time of neutron presence within the crystal, $\tau_L = L/v\cos\Theta_B \approx L/v(\pi/2 - \Theta_B)$ (L is the crystal thickness), drastically increases. This allows one to increase the sensitivity of the diffraction method to the neutron EDM at least by an order of magnitude [4].

Thus, the study of the Laue diffraction at large Bragg angles and the answer to the question how close can be the diffraction angle to the $\pi/2$ value can provide an important information on the possibilities of the diffraction method for determining a neutron EDM.

2. Below, we describe the experimental study of the Laue case of neutron diffraction by a thick ($L \approx 3.5$ cm) crystal using the direct diffracted neutron beam. The diffraction was provided by the {110} planes of an α-quartz crystal.

The schematic of an experimental setup mounted on one of the horizontal channels of a WWR-M reactor is shown in Fig. 1. A neutron beam formed by a system of neutron guides (*1*, *2*) is diffracted from the {110} planes of an α-quartz crystal (*4*) normal to the "large crystal face" and is recorded by a detector (*5*). The absence of dispersion in the direct diffracted beam results in the fact that several reflecting planes simultaneously give their contributions to this beam. The necessary diffraction reflection can be singled-out using the time-of-flight method. A special mechanical beam chopper (*3*) placed before the crystal provided neutron pulses with a duration of ~75 μs and a frequency of 25 Hz.

A typical time-of-flight spectrum is shown in Fig. 2. One can clearly see the peaks corresponding to the reflections from the individual crystallographic planes.

Since the crystal was located between the beam chopper and the neutron detector, the total time of flight of a scattered neutron with the wavelength $\lambda = 2d\sin\Theta_B$ was equal to

$$\tau_f = \tau_l + \tau_L, \quad (5)$$

where τ_l is the time necessary for a neutron to fly for a distance l, τ_L is the time of neutron presence in a crystal

[1] We ignore the Pendellösung oscillations caused by wobbling of various waves, because, in the case under consideration, they are averaged over the Bragg angles.

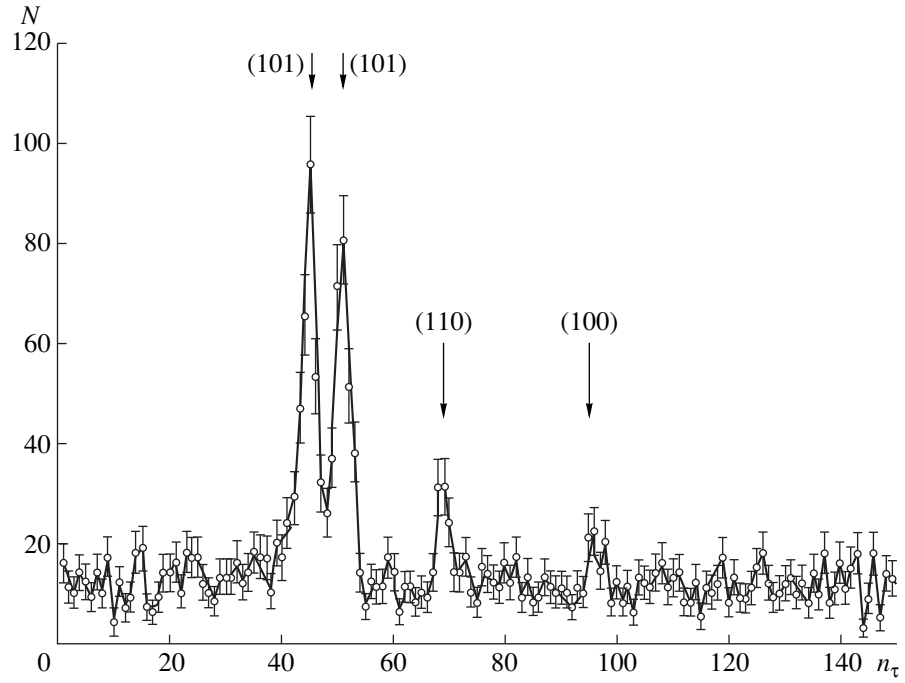

Fig. 2. Time-of-flight spectrum of neutrons scattered along the direct beam at the Bragg angle $\Theta_B = 75°$; n_τ is the ordinal number of the time channel. The width of the time channel equals ≈51.2 μs; N is the number of the events collected within five hours.

of thickness L at the diffraction angle Θ_B for the (110) plane of an α-quartz crystal, and $d = 2.4564$ Å:

$$\tau_l = \frac{l}{v} = \frac{m}{2\pi\hbar} l\lambda = \frac{dm}{\hbar\pi} l \sin\Theta_B, \quad (6)$$

$$\tau_L = \frac{L}{v\cos\Theta_B} = \frac{m}{2\pi\hbar}\frac{L\lambda}{\cos\Theta_B} = \frac{dm}{\hbar\pi} L\tan\Theta_B. \quad (7)$$

It is seen from (6) and (7) that the time τ_L of the neutron presence in the crystal depends on the Bragg angle as $\tan\Theta_B$, whereas the time of its flight τ_l depends on this angle as $\sin\Theta_B$. With an approach of the Bragg angle Θ_B to 90°, the contribution of τ_L to the total time of neutron flight, τ_f, considerably increases because $\tau_L/\tau_l \simeq L/l(\pi/2 - \Theta_B)$.

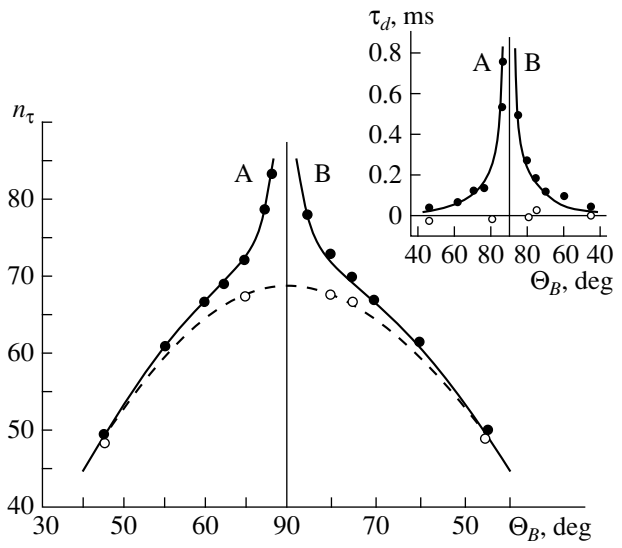

Fig. 3. Dependence of the time of flight of neutrons scattered along the direct beam as a function of the Bragg angle.

The time of flight of neutrons scattered by the (110) plane along the direct beam as a function of the Bragg angle is shown in Fig. 3. The solid line shows the theoretical dependence calculated by formula (5). The dashed line shows the dependence of τ_l on the Bragg angle [see (6)]. It is seen that the experimental values (filled circles) fit the theoretically calculated curve quite well.

To check the effect of the time delay of a neutron in a crystal, the beam chopper was placed between the crystal and the detector. In this case, the neutron delay in the crystal gives no contribution to the experimentally measured value, and the position of the line due to reflection from the (110) plane should coincide with the dashed curve (with due regard for different path lengths for two different positions of the beam chopper). This was really observed in the experiment (open circles in Fig. 2).

For a clearer representation, the inset in Fig. 3 shows the calculated and the observed dependences of τ_L on the Bragg angle.

3. Thus, it is experimentally shown that the time of the neutron presence in the crystal is determined not by the total neutron velocity v, but only by its component

$v_\parallel$ parallel to crystallographic planes and, thus, can really be increased by an order of magnitude at Bragg angles close to 90° (in particular, $\tau_L = (0.82 \pm 0.02)$ ms at $\Theta_B = 87°$, which corresponds to $v_\parallel = (43 \pm 1)$ m/s at $v = 810$ m/s).

The result obtained confirms the possibility of increasing the sensitivity of the neutron diffraction method by an order of magnitude for determining a neutron EDM at the Bragg angles close to 90°. Thus, it is possible to expect that the sensitivity of the neutron diffraction method can be made as high as that of the UCN method or even higher.

ACKNOWLEDGMENTS

The authors are grateful to V.L. Alekseev, V.L. Rumyantsev, and O.I. Sumbaev for their interest in this study and useful discussions and to the staff of the WWR-M reactor for their help in the preparation of the experiment.

The study was performed on a setup whose construction was supported by the Russian Foundation for Basic Research, project no. 96-02-18927.

REFERENCES

1. V. L. Alekseev, E. G. Lapin, and E. K. Leushkin, Preprint No. 1369, LIYaF USSR Acad. Sci. (Leningrad Inst. of Nuclear Physics, USSR Acad. Sci), 1988; Zh. Éksp. Teor. Fiz. **94**, 371 (1988) [Sov. Phys. JETP **67** (8), 1727 (1988)].
2. V. L. Alekseev, V. V. Fedorov, E. G. Lapin, *et al.*, Preprint No. 1502, LNPI USSR Acad. Sci. (Leningrad Inst. of Nuclear Physics, Academy of Sciences of USSR, 1989), p. 14; Nucl. Instrum. Methods Phys. Res. A **284**, 181 (1989).
3. V. L. Alekseev, V. V. Voronin, E. G. Lapin, *et al.*, Zh. Éksp. Teor. Fiz. **96**, 1921 (1989) [Sov. Phys. JETP **69**, 1083 (1989)].
4. V. V. Fedorov, V. V. Voronin, and E. G. Lapin, Preprint No. 1644, LNPI USSR Acad. Sci. (Leningrad Inst. of Nuclear Physics, Academy of Sciences of USSR, 1990), p. 36; J. Phys. G **18**, 1133 (1992).
5. V. V. Fedorov, in *Proceedings of the XXVI Winter School LiYAF* (1991), Part 1, p. 65.
6. V. V. Fedorov, V. V. Voronin, E. G. Lapin, and O. I. Sumbaev, Pis'ma Zh. Tekh. Fiz. **21**, 50 (1995) [Tech. Phys. Lett. **21**, 884 (1995)].
7. V. V. Fedorov, V. V. Voronin, E. G. Lapin, and O. I. Sumbaev, Physica B **234–236**, 8 (1997).
8. V. V. Fedorov and V. V. Voronin, in *Proceeding of the Jubilee XXX Winter School on Physics of Atomic Nucleus and Elementary Particles, St. Petersburg Inst. of Nuclear Physics*, Russian Academy of Sciences, 1996, Part 1, p. 123.
9. I. S. Altarev, Yu. V. Borisov, N. V. Borovikova, *et al.*, Phys. Lett. B **276**, 242 (1992); Preprint No. 2055, PIYaF RAN (St. Petersburg Inst. of Nuclear Physics, Russian Academy of Sciences, 1995).
10. D. Thompson, Nucl. Instr. Meth. A **284**, 40 (1989); K. F. Smith, N. Crampin, J. M. Pendlebury, *et al.*, Phys. Lett. B **234**, 191 (1990).
11. P. B. Hirsch, A. Howie, R. B. Nicholson, *et al. Electron Microscopy of Thin Crystals* (Butterworth, London, 1965; Mir, Moscow, 1968).
12. V. V. Fedorov, K. E. Kir'yanov, and A. I. Smirnov, Zh. Éksp. Teor. Fiz. **64**, 1452 (1973) [Sov. Phys. JETP **37**, 737 (1973)].
13. H. Rauch and D. Petrachek, in *Neutron Diffraction*, Ed. by H. Duchs (Springer, Berlin, 1978), p. 303.

Translated by L. Man

JETP Letters, Vol. 71, No. 2, 2000, pp. 80–84. Translated from Pis'ma v Zhurnal Éksperimental'noĭ i Teoreticheskoĭ Fiziki, Vol. 71, No. 2, 2000, pp. 116–122.

CONDENSED MATTER

Characteristic Fields of a $Bi_2Sr_2CaCu_2O_y$ Crystal

V. N. Zavaritskiĭ

Kapitsa Institute for Physical Problems, Russian Academy of Sciences, Moscow, 117334 Russia
H.H. Wills Physics Laboratory, University of Bristol, Bristol BS8 1TL, UK
e-mail: vlad@kapitsa.ras.ru

Received December 15, 1999

Abstract—The field dependences of the transverse resistance of a $Bi_2Sr_2CaCu_2O_y$ (BSCCO) layered superconducting single crystal with $T_{c0} \geq 92$ K are studied in a perpendicular ($H \perp (ab)$) pulsed magnetic field up to 50 T in a wide temperature range, 4.2–300 K. The temperature dependences of the characteristic fields identified with the "irreversibility curve" and the field corresponding to the nucleation of the superconducting phase are determined. The results obtained for the latter field are compared with the theoretical dependences. © *2000 MAIK "Nauka/Interperiodica".*

PACS numbers: 74.72Hs; 74.25.Fy; 74.60.Ge

A high critical temperature in combination with a small correlation length lead to considerable departure of the *H–T* diagram of cuprate high-T_c superconductors from that of ordinary superconductors. Specifically, this diagram is characterized by a new line—the so-called "irreversibility curve" $H_{irr}(T)$ (lying well away from the upper critical field), which separates the region where the vortex lattice and the persistent supercurrent exist from the wide range of fields and temperatures where the vortex liquid state with ohmic response is observed [1]. There are indications that in perfect high-T_c superconductor crystals, the vortex lattice melting occurs through a phase transition of the first kind (see, e.g., [2]). In contrast to $H_{irr}(T)$, both the value and the temperature dependence of the upper critical field in high-T_c superconductors are subjects of discussion; specifically, it is widely believed that this field does not manifest itself in the experiment because of the fluctuation effects [3]. Most estimates of the quantity $H_{c2}(0)$ are obtained in the framework of the BCS theory by extrapolating [4] the results of the fluctuation analysis of magnetoresistance and magnetization near the critical temperature [5–7] to $T \longrightarrow 0$. At the same time, the experimental dependence $H_{c2}(T)$ determined from the measurements of the magnetoresistance of a $Tl_2Ba_2Ca_0Cu_1O_y$ crystal displayed a negative curvature in an unprecedentedly wide temperature range, $10^{-3} \leq T/T_c \leq 1$ [8]. Such a behavior contradicted both the BCS theory and the tight-binding model. In the subsequent experiments, the anomalous behavior of the dependence $H_{c2}(T)$ was observed for overdoped specimens from other groups of cuprate high-T_c superconductors [9], as well as for a number of organic superconductors [10]. These results were in their turn criticized, in particular, because of the method used for the suppression of the critical temperature: this method allowed the coexistence of phases with different T_c, and such an inhomogeneity could give rise to the aforementioned kind of dependences in the framework of the BCS theory, which was shown theoretically for an idealized model [11]. This argument was *a priori* unsuitable for the interpretation of the results obtained on optimum-doped crystals [12]. However, the abundance of assumptions and the complexity of the multistage empirical extrapolation procedure used in [12] called for a more direct verification of the results. Such an attempt is made in this study. Here, based on the analysis of the transformation of the magnetoresistance of a $Bi_2Sr_2CaCu_2O_y$ (BSCCO) crystal in the course of the temperature variation from 300 K to T_c, the behavior of the magnetoresistance of the system in the normal state is determined; on this basis, the contribution of the superconducting state to the magnetoresistance at $T < T_{c0}$ is separated, and the temperature dependences of the characteristic fields, which are identified with the field of the nucleation of the superconducting phase and the irreversibility curve, are obtained.

The specimens were BSCCO crystals of rated composition with $T_{c0} > 90$ K; the "optimum" doping level was achieved by partial substitution of yttrium for calcium in the crystal lattice [13]. The methods of testing the crystals for the macroscopic homogeneity of composition and the absence of blocks, as well as the technique used for the preparation of low-ohmic contacts and the mounting of specimens, were described earlier [14]. To reduce the effects of overheating due to the currents induced by the field pulse, small-size specimens were used. The allowable values were determined experimentally on a series of specimens of different areas; a comparative analysis was performed for the field dependences of the resistance measured at low temperature in magnetic field pulses of different ampli-

tude. It was found that, as the crystal cross-section decreased from $\approx 10^4$ μm^2 to $\approx 10^3$ μm^2, the specimen overheating caused by a pulse of 55 T was reduced below the measuring ability of the experimental setup in the temperature range $T \geq 10$–15 K. The results presented in this paper were obtained on a series of crystals with the characteristic dimensions in the basal plane no greater than 30×30 μm^2. The measurements were performed with an ac bridge at a frequency of ≈77.7 kHz. The induced contribution to the useful signal was eliminated in two stages: at the first stage, in the course of the measurement, the parasitic emf induced by the field pulse was partially cancelled by the signal from the test coil placed near the specimen; then, the final separation of the contributions and the determination of the useful signal were performed by a numerical phase-sensitive detection.

The measurements were performed in a glass cryostat whose tail was placed at the center of a resistive coil; the pulsed magnetic field was generated by a capacitor discharge through this coil. The specimen was mounted at the end of a plastic cryogenic insert, and the latter was positioned in the tail of the Dewar flask so as to place the specimen at the center of the solenoid with an accuracy of 0.5 mm or better; the position of the specimen was controlled by the signal from the test coil. A tight fit of the insert in the tail of the Dewar flask was achieved by using a cotton wrapping, which served for the vibration damping and as a heat resistance allowing the measurements in the temperature range from 1.4 to 350 K. The electric wiring was manganin. The temperature was stabilized and controlled by a couple of resistance thermometers with a positive and a negative temperature coefficients; the thermometers were calibrated in the same setup and provided the temperature stabilization at a level of 10^{-4} or better in the entire temperature range. A more detailed description of the experiment and the numerical methods used for the phase-sensitive detection of the useful signal can be found in [14].

The purpose of this study is the determination of the upper critical field on the assumption that the nucleation of the superconducting phase will lead to a departure of the magnetoresistance from its behavior typical of the normal state. With allowance for the expected anomalously large width of the region of superconducting fluctuations, the characteristics of the normal state were studied in an extended temperature range: for every crystal, the field dependences of the transverse resistance were measured for a set of temperatures beginning from 300–350 K. The magnetic field was perpendicular to the basal plane of the crystal and parallel to the measuring current; the estimated accuracy of the field orientation was ≈5°. According to [14], it was established that the longitudinal magnetoresistance of the crystal is negative, and, to a first approximation, it can be represented by a linear dependence. The effect was found to be symmetric with respect to a reversal of the external field; the scatter of the experimental points allowed the approximation of the asymptotic behavior of the magnetoresistance at $H \longrightarrow 0$ by both linear and square-law dependences. A decrease in temperature was accompanied by an advanced increase in magnetoresistance as compared to the transverse resistance of the crystal in zero magnetic field $R_N(0)$. The normalized slope, $S = -R_N^{-1}(0)\partial R/\partial H$, exhibited an increase by a factor of approximately 500 as the temperature decreased from 200 to 87 K. This slope increase can be adequately described by the formula $S \propto \exp(T_0/T)$ with $T_0 \simeq 900 \pm 30$ K.

It should be noted that despite the qualitative similarity of the temperature dependences obtained for different crystals, the absolute values characterizing these dependences were noticeably different. For example, an almost fivefold scatter in the characteristic values of the normalized slope S was observed with an approximately threefold variation of the estimated resistance growth in zero magnetic field, $\Delta R_N(0)/R_N(0, 300\ \mathrm{K})$, for a temperature decrease from 300 to 50 K. Presumably, these differences reflect the microstructural features of the specimens. Taking into account that all crystals studied in the experiment had very close values of the critical temperature $T_{c0} \approx 92$–93 K, this fact can be considered as an additional evidence in support of the adequacy of assigning the quasilinear negative magnetoresistance to the properties of the normal state.

As the critical temperature was approached from above, the asymptotic behavior of the longitudinal magnetoresistance in strong fields was retained, while, in weak fields, deviations from the simple linear dependence were observed. These deviations increased with decreasing temperature, and at $T - T_{c0} \leq 2$–2.5 K, a field region appeared in which the initial part of the dependence had a positive slope, and the dependence $R(H)$ developed a maximum, R^*. With further temperature decrease below T_{c0}, the positive magnetoresistance region expanded, and a new field region with zero resistive response was observed. A typical dependence $R(H)$ for this temperature range is shown in the inset of Fig. 1.

According to [14], in the processing of the data shown in the inset of Fig. 1, the part of the dependence with the negative slope was identified with: (i) the longitudinal magnetoresistance of the crystal $R_N(H, T)$ under the conditions of a total superconductivity suppression by the field, and the value of $R_N(0)$ was determined by the linear extrapolation of the dependence to $H = 0$. The curve with the positive magnetoresistance was identified with the mixed state; (ii) the flux creep regime was attributed to the region of the formation of the resistive response with $R \propto H^{\gamma(T)}$ [14], and the data from this region were used to estimate the irreversibility field $H_{irr}(T)$; (iii) the flattening of the power-law dependence observed with further field growth at $R/R_N(0) \geq 0.05$–0.1 was identified with the transition to the viscous flux flow regime; in this region, the experi-

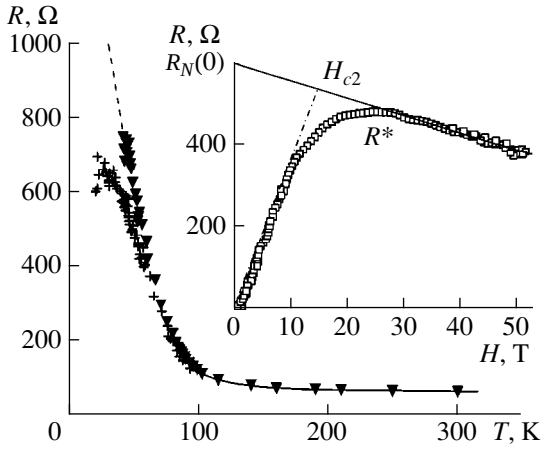

Fig. 1. Dependence $R_N(0, T)$ for a crystal in the normal state and under the conditions of the superconductivity suppression by the external magnetic field; the solid line corresponds to the dc measurements in zero magnetic field, the triangles represent $R_N(0, T)$, and the "+" symbols represent R^*. The inset shows the typical field dependence of the transverse resistance of a BSCCO crystal at $T \approx 50$ K $< T_{c0}$ and the determination of $R_N(0)$, R^*, and H_{c2}; the approximations shown are as follows: the solid line represents the magnetoresistance of a crystal in the normal state, and the dash-and-dot line corresponds to the flux flow regime.

mental curves allowed both linear, $R \propto H$, and logarithmic, $R \propto \log(H)$, approximations (the latter was proposed earlier [12] for describing the dependence $R(H)$ reconstructed from the dependences $R(T)$ of the transverse resistance measured for BSCCO in magnetic fields $H \leq 15$ T). As is shown in the inset of Fig. 1, the value of the characteristic field H^*_{c2} was estimated by the point of intersection of the extrapolated linear approximations from the regions (i) and (iii). The degree of validity of this method differs little from that of the conventional method where the "resistive" field H_{c2} is determined as the field corresponding to a certain decrease in the resistance relative to its value in the normal state.

The typical results of such a determination of H_{c2} are represented by squares in Fig. 2; this figure also shows the temperature dependence of the irreversibility field determined at a fixed level, $R(H)/R_N(0) = 10^{-2}$ for the same crystal. Although the latter curve gives only a rough estimate from above for the true H_{irr}, it adequately represents the character of the dependence: to a first approximation, the experiment demonstrated the invariable character of the dependence $H_{irr}(T)$ on condition that the resistive criterion was selected in the region of the power-law dependence of the resistance on magnetic field, i.e., for $R/R_N \leq 0.1$. In view of this fact, the quantitative and qualitative differences between the dependences shown in Fig. 2 indicate that it is inadequate to identify the "resistive" $H_{c2}(T)$ with the characteristics of the vortex ensemble; these differences unambiguously testify to the inapplicability of the conclusions [3], which identify the resistive H_{c2} with the irreversibility curve, to the case of BSCCO. Moreover, below, it will be shown that the unusual character of the dependence of the "resistive" field $H_{c2}(T)$ is retained regardless of the method used for the experimental data processing in the framework of the assumptions (i) and (iii).

It was found that the effect of temperature on the form of the dependence $R(H)$ of a BSCCO crystal is also unusual. This is illustrated by Fig. 3 representing the experimental results for different temperatures in the normalized form, $R(H)/R_N(H)$, which is used to eliminate the temperature dependences of the characteristics in the normal state. As can be seen from the figure, the effect of magnetic field on the resistance of high-T_c superconductors noticeably differs from the typical one observed for low-temperature superconductors: instead of a nearly parallel shift of curves with decreasing temperature, a decrease in their slope is observed, while the initial point is virtually unaffected.

These anomalies prove to be interrelated on the assumption that the linear positive magnetoresistance in the flux flow regime obeys the Bardeen–Stephen relation

$$R_{FF} \propto R_N H/H_{c2}. \quad (1)$$

In this case, the unusual character of the changes that occur in the dependences shown in Fig. 3 with temperature proves to be a consequence of the anomalous behavior of the dependence $H_{c2}(T)$; however, the applicability of formula (1) is at first glance is questionable, because the described measurements were performed in a formally force-free geometry, $H \parallel I \parallel c$. This inconsistency can be resolved by taking into account the layered structure of BSCCO owing to which a vortex consists of a system of Abrikosov vortices in superconducting layers connected by coreless "Josephson" segments. Since the positional correlation of vortices located in adjacent planes is easily violated, e.g., by thermal fluctuations [1], this leads to the appearance of a Josephson "string" component perpendicular to the field and subjected to the Lorentz force. As no theoretical calculations for the conditions of the experiment had been performed, these speculations give certain grounds to use formula (1), although it is evident that, in the geometry of the experiment, the resistive response essentially depends on the type of interaction between the "string" and the core component of the vortex. Nevertheless, as will be shown below, the analysis of the experimental data testifies to the applicability of relation (1).

The "×" symbols in Fig. 2 show the results of the determination of H_{c2} by relation (1) for the same crystal. For R_N, the values of $R_N(0)$ and R^* shown in Fig. 1 were used; the latter values were scaled so as to coincide numerically with $R_N(0)$ in the framework of the evident assumption that the weakening of the dependence $R^*(T)$ with decreasing temperature is caused by

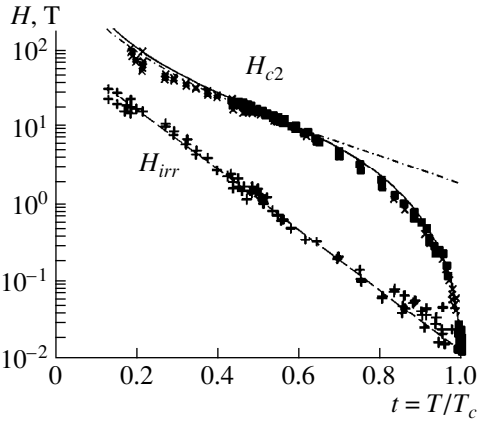

Fig. 2. Characteristic fields of a BSCCO crystal: the "+" symbols represent $H_{irr}(T)$, the squares represent H_{c2} determined by the method shown in Fig. 1, and the "×" symbols are the data obtained from relation (1). The solid line displays the fitting by the one-parameter dependence [15], and the dashed line corresponds to the "pseudo-H_{c2}" [11].

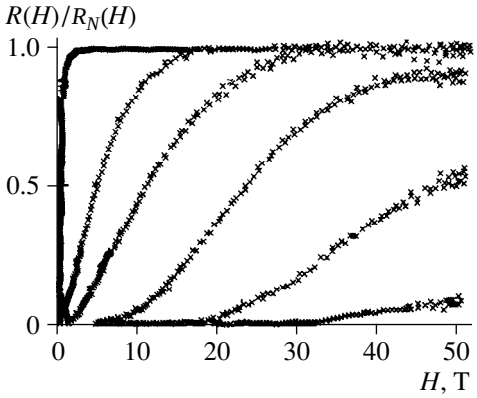

Fig. 3. Typical changes that occur with temperature variation in the field dependence of the interlayer resistance of a BSCCO crystal in the mixed state. The plot represents the normalized experimental dependences $R(H)/R_N(H)$ measured at $T \approx 16$, 20, 30, 45, 57.5, and 88.7 K.

the combined effect of $S(T)$ and $\partial R_{FF}/\partial H = f(T)$. As can be seen from Fig. 2, the results obtained by the two methods agree well with each other. The third method used for estimating H_{c2} is based on the approximation $R(H) \propto \log(H)$, which also adequately describes the results of measurements in the flux flow regime for $(0.2–0.3) \geq R/R_N \geq (0.7–0.8)$. As in the inset of Fig. 1, the value of H_{c2} was determined by the extrapolation of the logarithmic approximation to (i) $R(H)/R_N(H) = 1$ and (ii) $R(H)/R_N(0) = 1$; in the second case, for $R_N(0)$ at low temperatures, the extrapolation of the simplest empirical approximation of the data, $R_N(0) \propto \exp(-T/T_0)$, was used. It is evident that the estimate of H_{c2} obtained with this method quantitatively differs from the estimates presented above. However, it was found that these differences are easily eliminated by a simple scaling (with a temperature-independent coefficient close to 2). The result of such a scaling coincides with the dependence $H_{c2}(T)$ shown in Fig. 2 within the scatter of the experimental points.

The qualitative agreement between the results obtained by using different methods presumably testifies to the existence of a single physical mechanism that is responsible for the behavior of the magnetoresistance in the flux flow regime. The functionally different approximations of the experimental data presumable reflect the field dependence of the Josephson vortex component pinning by the Abrikosov one, but this interpretation cannot be considered as final in the absence of a theoretical calculation for this case. Although the experimental data are insufficient for a unique identification of the determined characteristic field with the upper critical field, (i) the qualitative agreement between the temperature dependences $H_{c2}(T)$ determined by different methods together with (ii) the quantitative agreement between the results obtained by one method on different crystals with close T_c but (iii) widely different characteristics of the normal state lend support to the statement that the experimental results represent the characteristics of the condensate rather than the individual features of the specimens.

From Fig. 2, one can see that the dependence $H_{c2}(T)$ has a negative curvature in the entire temperature range away from T_c, which contradicts the BCS theory; however, to a first approximation, this dependence is similar to the curves obtained earlier for other cuprate superconductors [8–10, 12]. The limited interval of fields available in the experiment made it impossible to observe this dependence at low temperatures. The extrapolation of the low-temperature asymptotics $H_{c2} = H_{c2}(0)\exp(-T/T^*)$, where $T^* = 18 \pm 2$ K, yields a rough estimate $H_{c2}(0) \approx 220 \pm 30$ T (close to the estimate of the paramagnetic limit in the BCS model) and the correlation length $\xi_{ab}(0) \approx 12$ Å, which proves to be of the order of the characteristic distance between the carriers [10]. It should be noted that these estimates fall into the interval of the cited values for the system under study, $H_{c2}(0) \approx 22–400$ T and $\xi_{ab}(0) \approx 9–38$ Å [5–7].

Figure 2 also displays the approximation of the results by some approbated model dependences. The dash-and-dot line shows the fitting by the relation for the "pseudo-H_{c2}" $\propto T^{-1}\exp(-T/T_0)$, which was obtained in the framework of a model treatment of the conductivity of a superconducting host containing a system of small-size inclusions with a higher T_c (such a model was proposed in [11] for describing the results reported in [8]). As seen from the figure, the agreement of the theory [11] with the experimental results is far from perfect, especially at high temperatures. Besides, the experimental dependences $R(T, H)$ obtained for the crystals under study had no discernible features above T_c, as might be expected in the case of the applicability

of the model described in [11]. A much better agreement between the theory and the experiment is obtained with the approximation of the experimental data by the one-parameter dependence $H_{c2} \sim (t^{-1} - t^{1/2})^{3/2}$ predicted in the framework of the bipolaron model [15] (the solid line in Fig. 2). Taking into account that in this case the parameter variation reduces to a trivial scaling of the field amplitude, the agreement achieved with this approximation can be interpreted in favor of the applicability of the model described in [15].

Thus, in this paper, the effect of a strong magnetic field on the interlayer resistance of a BSCCO crystal was studied in a wide temperature range, and a self-consistent empirical procedure was proposed for estimating the characteristic fields identified with $H_{irr}(T)$ and $H_{c2}(T)$. The latter is supported by the qualitative similarity of the dependences determined by different methods, as well as the coincidence (within the scatter of experimental points) of the dependences $H_{c2}(T)$ determined by a single method for crystals with close T_c and noticeably different characteristics of the normal state. It is established that the experimental curve is adequately described by the one-parameter dependence predicted in the boson limit [15] for the upper critical field.

ACKNOWLEDGMENTS

This work was performed under the projects supported by the Leverhulme Trust (F/182/AT), the Russian Foundation for Basic Research (no. 98-02-17485), and the Council on Superconductivity (no. 96115). The author is grateful to M. Springford, A.S. Aleksandrov, and D. Geshkenbein for valuable discussions and to the personnel of the low temperature laboratories for hospitality, encouraging support, and technical assistance.

REFERENCES

1. G. Blatter, M. V. Feigel'man, V. B. Geshkenbein, *et al.*, Rev. Mod. Phys. **66**, 1125 (1994).
2. M. Charalambous, J. Chaussy, P. Lejay, and V. Vinokur, Phys. Rev. Lett. **71**, 436 (1993).
3. J. R. Cooper, J. W. Loram, and J. M. Wade, Phys. Rev. B **51**, 6179 (1995).
4. N. R. Werthamer, E. Helfand, and P. C. Hohenberg, Phys. Rev. **147**, 295 (1966).
5. Quiang Li, K. Shibutani, M. Suenaga, *et al.*, Phys. Rev. B **48**, 9877 (1993).
6. R. Jin, A. Shilling, and H. R. Ott, Phys. Rev. B **49**, 9218 (1994).
7. A. Pomar, M. V. Ramallo, J. Mosqueira, *et al.*, Phys. Rev. B **54**, 7470 (1996).
8. A. P. Mackenzie, S. R. Julian, G. G. Lonzarich, *et al.*, Phys. Rev. Lett. **71**, 1238 (1993).
9. M. S. Osofsky, R. J. Soulen, S. A. Wolf, *et al.*, Phys. Rev. Lett. **71**, 2315 (1993); D. J. C. Walker, O. Laborde, A. P. Makenzie, *et al.*, Phys. Rev. B **51**, 9375 (1995).
10. B. Brandow, Phys. Rep. **296**, 1 (1998).
11. V. B. Geshkenbein, L. B. Ioffe, and A. J. Millis, Phys. Rev. Lett. **80**, 5778 (1998).
12. A. S. Alexandrov, V. N. Zavaritskiĭ, W. Y. Liang, *et al.*, Phys. Rev. Lett. **76**, 983 (1996).
13. N. V. Zavaritskiĭ, V. N. Zavaritskiĭ, A. P. Mackenzie, *et al.*, Pis'ma Zh. Éksp. Teor. Fiz. **60**, 188 (1994) [JETP Lett. **60**, 193 (1994)].
14. V. N. Zavaritskiĭ and M. Springford, Pis'ma Zh. Éksp. Teor. Fiz. **68**, 420 (1998) [JETP Lett. **68**, 448 (1998)]; V. N. Zavaritskiĭ, M. Springford, and A. S. Alexandrov, submitted to Phys. Rev. Lett. (1999).
15. A. S. Alexandrov, Phys. Rev. B **48**, 10571 (1993).

Translated by E. Golyamina

JETP Letters, Vol. 71, No. 2, 2000, pp. 85–88. From Pis'ma v Zhurnal Éksperimental'noĭ i Teoreticheskoĭ Fiziki, Vol. 71, No. 2, 2000, pp. 123–127.

CONDENSED MATTER

Theory of Spherulitic Domains in Cholesteric Liquid Crystals with Positive Dielectric Anisotropy[1]

A. N. Bogdanov

Max-Planck-Institute for the Physics of Complex Systems, D-01187 Dresden, Germany

Permanent address: Donetsk Institute for Physics and Technology, Donetsk, 340114 Ukraine

e-mail: bogdanov@host.dipt.donetsk.ua

Received December 15, 1999

Abstract—New localized axisymmetric nonsingular solutions minimizing the Frank functional have been found for a cholesteric layer with homeotropic anchoring. They have a continuous distribution of the director field and are characterized by a convex shape. These solutions describe the so-called spherulitic domains which have been observed in a large-pitch cholesteric near the unwinding transition. © *2000 MAIK "Nauka/Interperiodica"*.

PACS numbers: 61.30.Cz; 64.70.Md

Inhomogeneous localized structures (*topological defects or localized states*) are the focus of attention in many fields of modern physics. Since the late 1960s, soliton-like solutions of nonlinear field equations have been studied in condensed matter physics and biophysics, in particle and nuclear physics, in astrophysics, and in cosmology [1]. In particular, spontaneous pattern formation during symmetry breaking phase transitions is intensively studied in particle physics, cosmology, and many regions of condensed matter physics. The idea to model cosmological scenarios in condensed matter systems [2] has given new directions to the intradisciplinary collaboration in the physics of topological defects.

It is characteristic of liquid crystals to have a rich variety of phases and phase transitions between them [3]. Due to optical anisotropy of liquid crystals, inhomogeneous states can be observed directly with a polarizing microscope; material and external parameters can be easily varied in a wide range; as a rule, experiments are carried out at room temperature. All these advantages make liquid crystal a convenient object for the modeling and investigation of different inhomogeneous states. Recently, numerous experimental and theoretical results on pattern formation [4] and solitons [5] have been obtained for liquid crystals.

During the last decades, many experiments have been devoted to topological defects in a large-pitch cholesteric near the unwinding transition (see bibliography in [6]). In these experiments, a thin layer of a liquid crystal is sandwiched between two parallel electrodes which anchor the molecules perpendicularly to the surfaces (homeotropic anchoring). Depending on the value and frequency of an applied electric field, textures consisting of elongated domains (*fingers*), loops, spirals, and bubble-shaped objects (named *cholesteric bubbles* or *spherulitic domains*) have been observed in many samples, and their static and dynamic properties have been investigated. Spherulitic domains are generated by quenching of electrohydrodynamic turbulence and at the cholesteric-isotropic transition. They exist either as isolated localized states or form regular lattices. Up to now, several models of spherulitic domains have been proposed [7, 8]. In these contributions, the director field in spherulitics has one or more singular lines (disclinations).

The aim of this Letter is to propose a nonsingular model for spherulitic domains in cholesterics with positive dielectric anisotropy. It is shown that localized rotationally symmetric structures with a continuous distribution of the director field are among the solutions of the equations minimizing the Frank functional for the cholesteric layer with the homeotropic boundary alignment. These static solutions are stabilized by an energy contribution linear in the first order spatial derivatives of the director, which arises from enantiomorphy of cholesteric materials. The convex shape of spherulitic is due to homeotropic anchoring.

The possible distributions of the director $\mathbf{n}(\mathbf{r})$ of a bulk cholesteric in an applied electric field $\mathbf{E}$ are determined by minimizing the Frank free energy [3]

$$\Delta F = \int f\,dV = \int\left[\frac{K_1}{2}(\mathrm{div}\mathbf{n})^2 + \frac{K_2}{2}(\mathbf{n}\cdot\mathrm{rot}\mathbf{n} - q_0)^2 + \frac{K_3}{2}(\mathbf{n}\times\mathrm{rot}\mathbf{n})^2 - \frac{\varepsilon_a}{2}(\mathbf{n}\cdot\mathbf{E})^2 - f_0\right]dV, \quad (1)$$

[1] This article was submitted by the author in English.

0021-3640/00/7102-0085$20.00

where K_i and q_0 are elastic constants; ε_a is the dielectric anisotropic constant (we consider materials with $\varepsilon_a > 0$); $f_0 = K^2/2 - \varepsilon_a E^2/2$ is a free energy density for the homogeneous state with $\mathbf{n} \parallel \mathbf{E}$. At zero electric field, the ground state of a cholesteric corresponds to a helical structure with a pitch $p = 2\pi/|q_0|$. With increasing electric field perpendicular to the helix axis, the pitch gradually increases. Finally, in the critical field

$$E_0 = \frac{\pi q_0}{2}\sqrt{\frac{K_2}{\varepsilon_a}} \tag{2}$$

the system transforms into a homogeneous states with $\mathbf{n} \parallel \mathbf{E}$.

Consider a thin layer of liquid crystal placed between two parallel glass plates. Let the z axis be perpendicular to the glass plates. The layer has the thickness D and is infinite in x and y directions. The liquid crystal is constrained to be perpendicular to the boundary surfaces (homeotropic anchoring) and an electric field $\mathbf{E}$ is applied along the z direction. This model corresponds to geometry of the experiments on spherulitic domains.

For simplicity, an approximation of equal elastic constants will be used ($K_1 = K_2 = K_3 = K$). It is convenient to express the director vector in terms of spherical coordinates

$$\mathbf{n} = (\sin\theta\cos\psi, \sin\theta\sin\psi, \cos\theta),$$

and the spatial variable in cylindrical coordinates $\mathbf{r} = (\rho, \varphi, z)$. In these variables, the energy density f (1) assumes the following form:

$$f = \frac{K}{2}\left\{\left(\frac{\partial\theta}{\partial z}\right)^2 + \left(\frac{\partial\theta}{\partial\rho}\right)^2 + \frac{\sin^2\theta}{\rho^2}\left(\frac{\partial\psi}{\partial\varphi}\right)^2 + 2q_0\left[\left(\frac{\partial\theta}{\partial\rho}\right) + \frac{\sin\theta\cos\theta}{\rho}\left(\frac{\partial\psi}{\partial\varphi}\right)\right]\sin(\psi - \varphi)\right\} + \frac{\varepsilon_a E^2\sin^2\theta}{2} + \frac{\beta}{2}\sin^2\theta\,\delta(z \pm z_0). \tag{3}$$

The last term in (3) describes the interaction between the liquid crystal and the confining surfaces ($z = \pm D/2$); for homeotropic anchoring, $\beta > 0$; $\delta(x)$ is the Dirac function.

The variational problem for the energy functional (1) with (3) has rotationally symmetric solutions $\theta(\rho, z)$, $\psi(\varphi) = \varphi + \pi/2$. Substituting this solution into (3) and integrating the energy (1) with respect to φ, one obtains

$$\Delta F = \pi K\int_{-D/2}^{D/2} dz\int_0^\infty \rho\, d\rho\left\{\left(\frac{\partial\theta}{\partial z}\right)^2 + \left(\frac{\partial\theta}{\partial\rho}\right)^2 + \frac{\sin^2\theta}{\rho^2} - \frac{2q_0}{K}\left(\frac{\partial\theta}{\partial\rho} + \frac{\sin\theta\cos\theta}{\rho}\right) + \frac{\varepsilon_a E^2}{K}\sin^2\theta + \frac{\beta}{K}\sin^2\theta\,\delta(z \pm z_0)\right\}. \tag{4}$$

The Euler equation for the functional (4)

$$\frac{\partial^2\theta}{\partial z^2} + \frac{\partial^2\theta}{\partial\rho^2} + \frac{1}{\rho}\frac{\partial\theta}{\partial\rho} - \frac{\sin\theta\cos\theta}{\rho^2} - \frac{2q_0}{K}\frac{\sin^2\theta}{\rho} - \frac{\varepsilon_a E^2}{K}\sin\theta\cos\theta = 0 \tag{5}$$

with boundary conditions $\theta(0, z) = 0$, $\theta(\infty, z) = \pi$,

$$\left(\frac{\partial\theta}{\partial z} + \frac{\beta}{K}\sin\theta\cos\theta\right)_{z = \pm D/2} = 0 \tag{6}$$

describes the director field in a nonsingular localized axisymmetric structure.

If the anchoring at the surfaces disappears, ($\beta \longrightarrow 0$) (5) transforms to an ordinary equation:

$$\frac{d^2\theta}{d\rho^2} + \frac{1}{\rho}\frac{d\theta}{d\rho} - \frac{\sin\theta\cos\theta}{\rho^2} - \frac{2q_0}{K}\frac{\sin^2\theta}{\rho} - \frac{\varepsilon_a E^2}{K}\sin\theta\cos\theta = 0 \tag{7}$$

for localized structures homogeneous along the z axis. Equation (7) has the same functional form as those for localized states in noncentrosymmetric ferromagnets [9] and chiral liquid crystals [10]. Numerical integration shows that (7) has metastable localized solutions $\theta(\rho)$ for all $E > E_0$ (2). The functions $\theta(\rho)$ decay exponentially at large distances, and usually the profiles $\theta(\rho)$ have an arrow-like core that can be approximated by a linear ansatz:

$$\theta(\rho) = \pi\frac{\rho}{\rho_0} \quad (0 < \rho < \rho_0), \quad \rho_0 = \frac{4}{\pi^2 q_0}\left(\frac{E_0}{E}\right)^2. \tag{8}$$

The localized structures are compressed by increasing electric field but they do not collapse even at a high field. It is clear, however, that there should be an upper boundary field where the core size becomes of the order of the molecular length and the elastic approach cannot be applied. Near the critical field E_0, the profile has an extending core with $\theta \approx 0$ separated from the outside by a narrow domain wall. As the field goes to its critical value, the localized solution transforms to the homogeneous state by unlimited expansion of the core.

It is important to mention that solutions under discussion are stabilized by the energy contribution linear in the first spatial derivatives of the director (the "chiral" term $\mathbf{n} \cdot \mathrm{rot}\mathbf{n}$). This energy term is specific for noncentrosymmetric cholesteric phases. In contrast, two-dimensional localized states are radially unstable and collapse spontaneously in centrosymmetric materials (e.g., in nematics or regular ferromagnets). The stability of two-dimensional localized static structures in nonlinear field models has been considered from a general point of view in [11]).

Now consider the influence of the homeotropic anchoring on the two-dimensional localized states. The solutions of (5) can be treated as certain deformations of a homogeneous along the z axis profile $\theta(\rho)$ by the surface anchoring:

$$\tilde{\theta}(\rho, z) = \theta(\rho) + \sum_{n=1}^{\infty} a_n(z)\sin n\theta(\rho). \quad (9)$$

In particular, deformations of type

$$\tilde{\theta}(\rho, z) = \theta[\rho/R(z)] \quad (10)$$

describing profile compression ($R < 1$) or expansion ($R > 1$), are of importance for our problem ($R(z)$ is an arbitrary positive number and characterizes the size of the profile core). Note that the main energy contribution in (4), represented by the first three terms, does not change under the scale transformation (10). Thus, one can assume that (10) gives the main contribution to the optimal deformation of the profile under the influence of the surface anchoring. The validity of this assumption has been proved numerically.

Integrating (4) with the solution (10), with respect to ρ, results in

$$W = \int_{-D/2}^{D/2} dz\left\{\left(\frac{dR}{dz}\right)^2 + A\frac{\varepsilon_a E^2}{K}R^2 - B\frac{2q_0}{K}R + \frac{\beta}{K}AR^2\delta(z \pm z_0)\right\}, \quad (11)$$

where

$$A = I_1/I_0, \quad B = I_2/I_0, \quad (12)$$

$$I_0 = \int_0^{\infty}\left(\frac{d\theta}{d\rho}\right)^2 \rho d\rho, \quad I_1 = \int_0^{\infty}\sin^2\theta\rho d\rho,$$
$$I_2 = \int_0^{\infty}\left(\frac{d\theta}{d\rho} + \frac{\sin\theta\cos\theta}{\rho}\right)\rho d\rho. \quad (13)$$

The Euler equation for the functional (11) with the boundary conditions

$$\left(\frac{dR}{dz}\right)_{z=\pm D/2} = \mp\frac{\beta}{K}AR \quad (14)$$

has an analytical solution:

$$R(z) = R_0\left[\frac{1+\gamma\tanh(\alpha)}{1+\gamma\coth(2\alpha)} - \frac{2\gamma\sinh^2(2\alpha z/D)}{\sinh(2\alpha)+\gamma\coth(2\alpha)}\right], \quad (15)$$

where

$$R_0 = \frac{BK}{A\varepsilon_0}\frac{q_0}{E^2}, \quad \alpha = \frac{DE}{4}\sqrt{\frac{A\varepsilon_a}{K}}, \quad \gamma = \frac{\beta\sqrt{A}}{\varepsilon_a E^2}. \quad (16)$$

Equation (15) describes a convex shape of the localized structure. The parameter R_0 characterizes the profile size and the parameters α and γ describe the structure convexity. The largest size is reached in the center of the layer ($z = 0$)

$$R_{\max} = R_0\frac{1+\gamma\tanh(\alpha)}{1+\gamma\coth(2\alpha)}, \quad (17)$$

and the smallest values

$$R_{\min} = \frac{R_0}{1+\gamma\coth(2\alpha)} \quad (18)$$

correspond to the layer surfaces ($z = \pm D/2$). The profile size and convexity decrease with increasing field. At a high field, the ratio

$$R_{\max}/R_{\min} = 1 + \gamma\tanh(\alpha) \quad (19)$$

goes to unity; i.e., the structure tends to be homogeneous along the z-axis.

The angle between the tangent to the line (15) and the z-axis

$$\xi = \arctan\left[-\frac{4\alpha\gamma R_0}{D}\frac{\sinh(4\alpha z/D)}{\sinh(2\alpha)+\gamma\coth(2\alpha)}\right] \quad (20)$$

equals zero for $z = 0$ and reaches the highest value at the surface.

In the strong anchoring limit ($\beta \longrightarrow \infty$), the localized structure has zero size at the surfaces ($R_{\min} = 0$) but the angle ξ has a finite value at the surfaces

$$(\xi)_{z=\pm D/2} = \mp\arctan\left[\frac{4\alpha R_0}{D}\tanh(2\alpha)\right]. \quad (21)$$

In summary, two-dimensional axisymmetric nonsingular localized structures can exist in cholesterics with positive dielectric anisotropy above the unwinding critical field E_0 (2). In layers with homeotropic anchoring, these localized states have a convex shape. They can be used as a model for the spherulitic domains observed in cholesteric layers with positive dielectric anisotropy. It is shown that such localized structures can exist not only near the critical field E_0, but also at higher fields. Their stability is due to the chiral energy contributions of cholesteric materials.

Spherulitic domains also occur in cholesteric thin layers with negative dielectric anisotropy and strong homeotropic anchoring (see, e.g., [7, 12]). There are no localized axial structures in bulk materials for this case. The formation and stability of such spherulitics are completely determined by surface anchoring. Theory of these localized states will be presented in a separate contribution.

ACKNOWLEDGMENTS

The idea for this work arose during the Seminar on Topological defects in Non-Equilibrium Systems and Condensed Matter. I am grateful to L. Kramer for the invitation to the seminar and P. Fulde for hospitality and support. I also thank P. Cladis, M. Kléman, L. Kramer, O. Lavrentovich, and A. Shestakov for helpful discussions and D. Garanin for critically reading the manuscript.

REFERENCES

1. C. Rebbi and G. Soliani, *Solitons and Particles* (World Scientific Pub. Co., Singapore, 1984).
2. W. H. Zurek, Phys. Rep. **276**, 177 (1996).
3. P. G. de Gennes and J. Prost, *The Physics of Liquid Crystals* (Clarendon, Oxford, 1993).
4. *Pattern Formation in Liquid Crystals*, Ed. by A. Buka and L. Kramer (Springer-Verlag, New York, 1996).
5. *Solitons in Liquid Crystals*, Ed. by L. Lam and J. Prost (Springer-Verlag, New York, 1992).
6. J. Baudry, S. Pirkl, and P. Oswald, Phys. Rev. E **59**, 5562 (1999).
7. A. E. Stieb, J. Physique **41**, 961 (1980).
8. S. Hirata, T. Akahane, and T. Tako, Mol. Cryst. Liq. Cryst. **75**, 47 (1981).
9. A. N. Bogdanov and D. A. Yablonsky, Sov. Phys. JETP **68**, 101 (1989); A. Bogdanov and A. Hubert, J. Magn. Magn. Mater. **195**, 182 (1999).
10. A. N. Bogdanov and A. A. Shestakov, JETP **86**, 911 (1998).
11. A. Bogdanov, JETP Lett. **62**, 247 (1995); **68**, 317 (1998).
12. T. Nagaya, H. Hotta, H. Orihara, and Y. Ishibashi, J. Phys. Soc. Jpn. **60**, 1572 (1990).

JETP Letters, Vol. 71, No. 2, 2000, pp. 89–91. Translated from Pis'ma v Zhurnal Éksperimental'noĭ i Teoreticheskoĭ Fiziki, Vol. 71, No. 2, 2000, pp. 128–131.

CONDENSED MATTER

On Possibility of a Structural Transition in the Vicinity of the Melting Point in Liquid Copper

V. I. Lad'yanov[1] and A. L. Bel'tyukov[2]

[1] *Physicotechnical Institute, Ural Division, Russian Academy of Sciences, ul. Kirova 132, Izhevsk, 426000 Russia*
e-mail: las@fti.udmurtia.su
[2] *Udmurtia State University, Izhevsk, 426034 Russia*

Received September 24, 1999, in final form, December 20, 1999

Abstract—The temperature dependence of the kinematic viscosity of liquid copper has been studied by the method of torsional vibrations during heating and cooling within the temperature range 1080–1500°C. A reversible structural transition was discovered in the vicinity of 1170°C. This transition manifests itself in a jumpwise change of viscosity and the activation energy of viscous flow at this temperature. © *2000 MAIK "Nauka/Interperiodica".*

PACS numbers: 61.25.Mv; 6470Ja 66.20+d

In recent years, the problem of first-order "phase" transitions in liquids has been extensively investigated (see, e.g. [1, 2]). The possible occurrence of such transitions was studied theoretically, in particular, in [3] and also by the molecular-dynamics methods in [4]. Drastic changes in the short-range order structure and the thermodynamic and kinetic properties under the effect of pressure were revealed in liquid Cs [5], Ga, Bi, Sb, Se, Te [2, 6], and other chemical elements. In liquid selenium and tellurium, the semiconductor–metal transition was accompanied by the change in conductivity by three–four orders of magnitude. The structural rearrangements can also be caused by temperature variations under atmospheric pressure (see, e.g., [7, 8]). These rearrangements manifest themselves in anomalies on the temperature dependences of various properties and, to a lesser degree, in the diffraction data. The mechanisms of the temperature- and pressure-induced structural transitions are still insufficiently clear and are intensely discussed [1, 7].

As far as we know, no anomalies on the temperature dependences of the properties of liquid copper have been revealed, although, in the vicinity of the melting point, a pronounced scatter in the experimental data is often observed. At the same time, the problem of the structure of liquid copper and its temperature variations still remains to be studied. It was indicated [9] that the atomic distribution in the melt does not correspond to the fcc lattice of the initial structure. More probably, it corresponds to a tetragonal body-centered lattice with the c/a ratio less than unity. The temperature rise results in insignificant changes on the corresponding diffraction patterns. It was also indicated [10] that the copper melt can have two coexisting types of the short-range order—bcc and fcc. The quantitative ratio between these two types is temperature-dependent. Therefore, we decided to study by the precision method the temperature dependence of one of the most structure-sensitive properties of liquid copper—its viscosity—in the vicinity of the melting point.

Kinematic viscosity ν of high-purity grade (OSCh-000) liquid copper was measured in a BeO crucible by the method of damped torsional vibrations in the purified helium atmosphere in the temperature range 1080–1500°C. The temperature was varied in a stepwise manner with a step of 10–15°C and was kept constant at each step for not less than 30 minutes within an accuracy of 1°C with the aid of a high-precision regulator. The vibration parameters were measured by the optical method with the use of a ruby laser and a precision photoelectric sensor with the delay time not exceeding 100 ns. The methods used for measuring and statistical–probabilistic processing of the experimental data were described in detail elsewhere [11]. The calculated errors showed that, at the confidence probability 0.95 in the temperature range 1000–1500°C, the most probable errors in the absolute viscosity values determined in each experiment did not exceed 1%, with the total error being less than 1.5%.

The experimental temperature dependences of liquid-copper viscosity shown in Fig. 1 were analyzed with the use of the conventional Arrhenius-type relationship

$$\nu = A\exp\frac{E}{RT}, \qquad (1)$$

where E is the activation energy of viscous flow. The construction of the corresponding error bars shows that the temperature dependence of liquid-copper viscosity cannot be described using the exponential dependence of type (1) alone. In the vicinity of $t = 1170$°C, viscosity shows pronounced (of about 7%) jump considerably

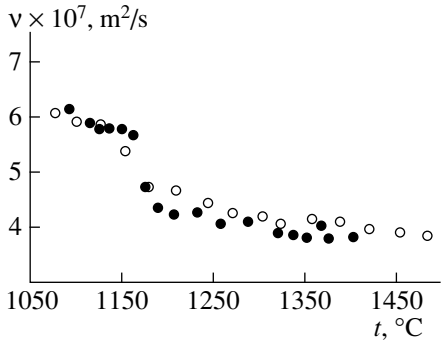

Fig. 1. Viscosity curves for liquid copper recorded during heating: ● the first and ○ the second experiments.

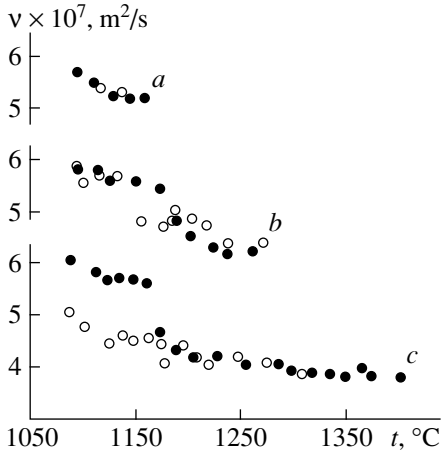

Fig. 2. Effect of the maximum heating temperature of liquid copper on the temperature dependence of its viscosity: ● during heating, ○ during cooling.

exceeding the experimental error. This jump in viscosity is also confirmed by the experimental data processed with the use of the confidence intervals and significance criteria (see table).

In order to clarify the nature of the anomaly revealed, we additionally measured viscosity ν under the following conditions. The first sample was heated to 1160°C, kept at this temperature for 30 min, and then cooled to room temperature (Fig. 2a). In this experiment, the viscosity values measured during heating and cooling were the same. The second sample was heated to 1300°C and then was cooled down (Fig. 2b). In this experiment as well, the viscosity jump was observed in the vicinity of 1170°C during heating, but, during cooling, the jump was observed at the temperature of 1150°C. The third sample was heated to 1500°C. The measurements were performed during heating and cooling (Fig. 2c), but, in this case, the viscosity jump was observed only during heating, whereas during cooling no jump was recorded at all. The absolute viscosity values measured above the anomaly temperature agree quite well with the data obtained by Samarin and Vertman [12].

The anomalous (jumpwise) change of the viscosity in the vicinity of 1170°C indicates the occurrence of a reversible structural transition in liquid copper at this temperature. As far as we know, this transition was observed in our study for the first time. As was indicated above, the mechanism of similar phenomena in metal melts is far from being clear. Earlier [8], it was shown that the manifestations of this phenomenon are analogous to the manifestations of the polymorphous transformations in the crystalline state and can be regarded as fine effects in the liquid phase. The structural transformations in the liquid state, similar to those in crystals, are accompanied by drastic variations in all the properties of the liquids and their temperature dependences at certain temperatures.

Taking into account the X-ray data [9], which indicate the formation of a tetragonal-type short-range order in liquid copper upon melting, one can assume that the structural transition observed in this study in the vicinity of 1170°C proceeds by the mechanism of the one-dimensional cluster polymorphism described in [13], where the transformation was accompanied by the drastic change in the cluster tetragonality (ordering of microregions) in copper and, as a result, by a jumpwise change in the viscosity and the activation energy of viscous flow. These structural rearrangements in liquid clusters reflect an increase in the degree of covalent bonding in these clusters provided by the change in the states of the electronic shells under the conditions of intensified thermal motion [14].

Parameters and confidence intervals for temperature dependences of viscosity for liquid copper (at $\alpha = 0.95$)

1083–1170°C	1170–1500°C
$\ln(\nu \times 10^7) = 2141/T + 0.224$	$\ln(\nu \times 10^7) = 1589/T + 0.407$
$0.071 < a_1 < 0.377$	$0.306 < a_2 < 0.508$
$1927 < b_1 < 2355$	$1441 < b_2 < 1737$
$-0.188 < a_1 - a_2 < -0.178$	
$178 < b_1 - b_2 < 926$	

Note: Parameters of approximating equation (1) are given in the semilogarithmic scale: $\ln(\nu \times 10^7) = b/T + a$.

REFERENCES

1. V. V. Brazhkin, R. N. Voloshin, A. G. Lyapin, and S. V. Popova, Usp. Fiz. Nauk **169**, 1035 (1999).
2. V. Brazhkin, S. Popova, and R. Voloshin, High-Pressure Res. **15**, 267 (1997)
3. L. D. Son and G. M. Rusakov, Rasplavy **5**, 90 (1995).
4. S. Harrington *et al.*, Phys. Rev. Lett. **78**, 2409 (1997).
5. I. N. Makarenko, V. A. Ivanov, and S. M. Stishov, Pis'ma Zh. Éksp. Teor. Fiz. **18**, 320 (1973) [JETP Lett. **18**, 187 (1973)].
6. S. M. Stishov, Zh. Éksp. Teor. Fiz. **52**, 1196 (1967) [JETP **25**, 795 (1967)].

7. B. A. Baum, *Metal Liquids* (Nauka, Moscow, 1979).
8. I. A. Novokhatskiĭ, V. Z. Kisun'ko, and V. I. Lad'yanov, Izv. Vyssh. Uchebn. Zaved., Chern. Metall. **1**, 9 (1985).
9. N. A. Vatolin and É. A. Pastukhov, *Diffraction Studies of Structures of High-Temperature Melts* (Nauka, Moscow, 1980).
10. A. G. Il'inskiĭ, Candidate's Dissertation in Phys.-Math. Sci. (Kiev, 1975).
11. S. V. Logunov and V. I. Lad'yanov, Rasplavy **3**, 63 (1996).
12. A. A. Belousov, S. G. Bakhvalov, S. N. Aleshina, *et al.*, *Physicochemical Properties of Liquid Copper and Copper-Based Alloys. Handbook* (Yekaterinburg, 1997).
13. I. A. Novokhatskiĭ, V. I. Arkharov, and V. I. Lad'yanov, Dokl. Akad. Nauk SSSR **267**, 367 (1982) [Sov. Phys. Doklady **27**, 963 (1982)].
14. V. K. Grigorovich, *Mendeleev Periodic Law and Electronic Structure of Metals* (Nauka, Moscow, 1966).

Translated by L. Man

JETP Letters, Vol. 71, No. 2, 2000, pp. 92–96. From Pis'ma v Zhurnal Éksperimental'noĭ i Teoreticheskoĭ Fiziki, Vol. 71, No. 2, 2000, pp. 132–138.

CONDENSED MATTER

c-Axis Penetration Depth in $Bi_2Sr_2CaCu_2O_{8+\delta}$ Single Crystals Measured by *ac*-Susceptibility and Cavity Perturbation Technique[1]

D. V. Shovkun, M. R. Trunin, A. A. Zhukov, Yu. A. Nefyodov, N. Bontemps*, H. Enríquez*, A. Buzdin, M. Daumens**, and T. Tamegai*****

Institute of Solid State Physics, Russian Academy of Sciences, Chernogolovka, Moscow oblast, 142432 Russia

** Laboratoire de Physique de la Matière Condensée, Ecole Normale Supérieure, 75231 Paris, France*

*** Laboratoire de Physique Théorique, Université Bordeaux I, 33405 Talence Cedex, France*

**** Department of Applied Physics, The University of Tokyo, Hongo, Bunky-ku, 113-8656 Japan*

Received December 24, 1999

Abstract—The *c*-axis penetration depth $\Delta\lambda_c$ in $Bi_2Sr_2CaCu_2O_{8+\delta}$ (BSCCO) single crystals as a function of temperature has been determined using two techniques, namely, measurements of the *ac*-susceptibility at a frequency of 100 kHz and the surface impedance at 9.4 GHz. Both techniques yield an almost linear function $\Delta\lambda_c(T) \propto T$ in the temperature range $T < 0.5T_c$. Electrodynamic analysis of the impedance anisotropy has allowed us to estimate $\lambda_c(0) \approx 50$ μm in BSCCO crystals overdoped with oxygen ($T_c \approx 84$ K) and $\lambda_c(0) \approx 150$ μm at the optimal doping level ($T_c \approx 90$ K). © *2000 MAIK "Nauka/Interperiodica".*

PACS numbers: 74.72.Hs; 74.25.Ha

Cuprate high-temperature superconductors (HTS) are layered anisotropic materials. Therefore the electrodynamic problem of the magnetic field penetration depth in HTS in the low-field limit is characterized by two length parameters, namely, λ_{ab} controlled by screening currents running in the CuO_2 planes (in-plane penetration depth) and λ_c due to currents running in the direction perpendicular to these planes (out-of-plane or *c*-axis penetration depth). The temperature dependence of the penetration depth in HTS is largely determined by the superconductivity mechanism. It is known (see, e.g., [1] and references therein) that $\Delta\lambda_{ab}(T) \propto T$ in the range $T < T_c/3$ in high-quality HTS samples at the optimal level of doping, and this observation has found the most simple interpretation in the *d*-wave model of the high-frequency response in HTS [2]. Measurements of $\Delta\lambda_c(T)$ are quoted less frequently than those of $\Delta\lambda_{ab}(T)$. Most of such data published were derived from microwave measurements of the surface impedance of HTS crystals [3–11]. There is no consensus in literature about $\Delta\lambda_c(T)$ at low temperatures. Even in reports on low-temperature properties of high-quality YBCO crystals, which are the most studied objects, one can find both linear, $\Delta\lambda_c(T) \propto T$ [4, 9], and quadratic dependences [11] in the range $T < T_c/3$. In BSCCO materials, the shape of $\Delta\lambda_c(T)$ depends on the level of oxygen doping: in samples with maximal $T_c \simeq 90$ K $\Delta\lambda_c(T) \propto T$ at low temperatures [7, 8]; at higher oxygen contents (overdoped samples) T_c is lower and the linear function $\Delta\lambda_c(T)$ transforms to a quadratic one [8]. The common feature of all microwave experiments is that the change in the ratio $\Delta\lambda_c(T)/\lambda_c(0)$ is smaller than in $\Delta\lambda_{ab}(T)/\lambda_{ab}(0)$ because in all HTS $\lambda_c(0) \gg \lambda_{ab}(0)$. The length $\lambda_c(0)$ is especially large in BSCCO crystals, $\lambda_c(0) > 10$ μm and, according to some estimates, it ranges up to ~500 μm. The large spread of $\lambda_c(0)$ is caused by two factors, namely, the poor accuracy of the techniques used in determination of $\lambda_c(0)$ and effects of local and extended defects in tested samples, whose range is of the order of 1 mm and comparable to both λ_c and total sample dimensions.

Recently, we suggested [12] a new technique for determination of $\lambda_c(0)$ based on the measurements of the surface barrier field $H_J(T) \propto 1/\lambda_c(T)$ at which Josephson vortices penetrate into the sample. The field H_J corresponds to the onset of microwave absorption in the locked state of BSCCO single crystals. This paper suggests an alternative technique based on comparison between microwave measurements of BSCCO crystals aligned differently with respect to ac magnetic field and a numerical solution of the electrodynamic problem of the magnetic field distribution in an anisotropic plate at an arbitrary temperature. Moreover, since $\lambda_c(0)$ in BSCCO single crystals is relatively large, we managed to determine $\lambda_c(T)$ from the temperature dependences of *ac*-susceptibility and compare these measurements to results of microwave experiments.

[1] This article was submitted by the authors in English.

Single crystals of BSCCO were grown by the floating-zone method [13] and shaped as rectangular platelets. This paper presents measurements of two BSCCO samples with various levels of oxygen doping. The first sample (#1), characterized by a higher critical temperature, $T_c \approx 90$ K (optimally doped), has dimensions $a \times b \times c \simeq 1.5 \times 1.5 \times 0.1$ mm^3 ($a \approx b$). The second (#2, $a \times b \times c \simeq 0.8 \times 1.8 \times 0.03$ mm^3) is slightly overdoped ($T_c \approx 84$ K).

When measuring the *ac*-susceptibility $\chi = \chi' - i\chi''$, we placed a sample inside one of two identical induction coils. The coils were connected to one another, and the out-of-phase and in-phase components of the imbalance signal were measured at a frequency of 10^5 Hz. These components are proportional to the real and imaginary parts of the sample magnetic moment M, respectively: $M = \chi v H_0$, where v is the sample volume and H_0 is the ac magnetic field amplitude, which was within 0.1 Oe in our experiments.

Figure 1 shows temperature dependences $\chi'(T)/|\chi'(0)|$ in sample #1 for three different sample alignments with respect to the ac magnetic field: the transverse (T) orientation, $\mathbf{H}_\omega \parallel \mathbf{c}$, (the inset on the left of Fig. 1), when the screening current flows in the *ab*-plane (full circles); in the longitudinal (L) orientation, $\mathbf{H}_\omega$, (the inset on the right of Fig. 1, $\mathbf{H}_\omega \perp \mathbf{c}$ is parallel to the *b*-edge of the crystal), when currents running in the directions of both CuO_2 planes and the *c*-axis are present (up triangles); in the L-orientation, $\mathbf{H}_\omega \perp \mathbf{c}$, whose difference from the previous configuration is that the sample is turned around the *c*-axis through 90° (down triangles). Figure 1 clearly shows that at $T < T_c$ $\chi'_{ab}(T)$ is notably smaller in the T-orientation than $\chi'_{ab+c}(T)$ in the L-orientation (the subscripts of χ' denote the direction of the screening current). The coincidence of $\chi'_{ab+c}(T)$ curves at $\mathbf{H}_\omega \perp \mathbf{c}$ and the small width of the superconducting transition at $\mathbf{H}_\omega \parallel \mathbf{c}$ ($\Delta T_c < 1$ K) indicate that the quality of tested sample #1 is fairly high. This is supported by precision measurements of surface impedance $Z_s(T) = R_s(T) + iX_s(T)$ of sample #1 at frequency $f = 9.4$ GHz in the T-orientation, which are plotted in Fig. 2. The measurement technique was described in detail elsewhere [1]. It applies to both surface impedance components $R_s(T)$ and $X_s(T)$:

$$R_s = \Gamma_s \Delta(1/Q), \quad X_s = -2\Gamma_s \delta f / f. \qquad (1)$$

Here, $\Gamma_s = \omega\mu_0 \int_V H_\omega^2\, dV / [\int_S H_s^2\, dS]$ is the sample geometrical factor ($\omega = 2\pi f$, $\mu_0 = 4\pi \times 10^{-7}$ H/m, V is the volume of the cavity, H_ω is the magnetic field generated in the cavity, S is the total sample surface area, and H_s is the tangential component of the microwave magnetic field on the sample surface); $\Delta(1/Q)$ is the difference between the values $1/Q$ of the cavity with the sample inside and empty cavity; and δf is the frequency shift relative to that

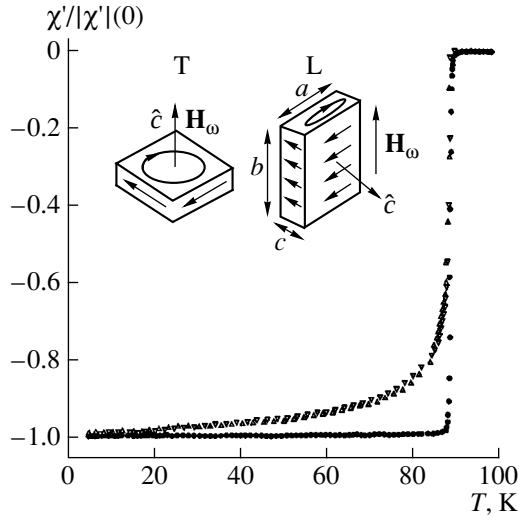

Fig. 1. Curves of the *ac*-susceptibility of sample #1 versus temperature in different orientation with respect to ac magnetic field: $\mathbf{H}_\omega \parallel \mathbf{c}$ (full circles); $\mathbf{H}_\omega \perp \mathbf{c}$, $\mathbf{H}_\omega$ is parallel to the *b*-edge of the crystal (up triangles); $\mathbf{H}_\omega \perp \mathbf{c}$, $\mathbf{H}_\omega$, is parallel to the *a*-edge of the crystal (down triangles). Left-hand inset: transverse (T) orientation, $\mathbf{H}_\omega \parallel \mathbf{c}$, the arrows on the surfaces show directions of the screening current. Right-hand inset: Longitudinal (L) orientation, $\mathbf{H}_\omega \perp \mathbf{c}$.

which would be measured for a sample with perfect screening, i.e., no penetration of the microwave fields. In the experiment, we measure the difference $\Delta f(T)$ between resonant frequency shifts with temperature of the loaded and empty cavity, which is equal to $\Delta f(T) = \delta f(T) + f_0$, where f_0 is a constant.[2] The constant f_0 includes both the perfect-conductor shift and the uncontrolled contribution caused by opening and closing the cavity. In HTS single crystals, the constant f_0 can be directly derived from measurements of the surface impedance in the normal state; in particular, in the T-orientation, f_0 can be derived from the condition that the real and imaginary parts of the impedance should be equal above T_c (normal skin-effect). In Fig. 2, $R_s(T) = X_s(T)$ at $T \geq T_c$, and its temperature dependence is adequately described by the expression $2R_s^2(T)/\omega\mu_0 = \rho(T) = \rho_0 + bT$ with $\rho_0 \approx 13$ μΩ cm and $b \approx 0.3$ μΩ cm/K. Given $R_s(T_c) = \sqrt{\omega\mu_0\rho(T_c)/2} \approx 0.12\ \Omega$, we obtain the resistivity $\rho(T_c) \approx 40$ μΩ cm. The insets to Fig. 2 show $R_s(T)$ and $\lambda(T) = X_s(T)/\omega\mu_0$ for $T < 0.7\ T_c$ plotted on a linear scale. The extrapolation of the low-temperature sections of these curves to $T = 0$ yields estimates of $\lambda_{ab}(0) \approx 2600$ Å and the residual surface resistance $R_{res} \approx 0.5\ m\Omega$. R_{res} is due to various defects in the surface layer of the superconductor and it is generally accepted that the lower the R_{res}, the better the sample quality. The above mentioned

[2] We note that $\delta f(T)$ includes the frequency shift due to the sample thermal expansion, which is essential for $T > 0.7T_c$ in the T-orientation [1].

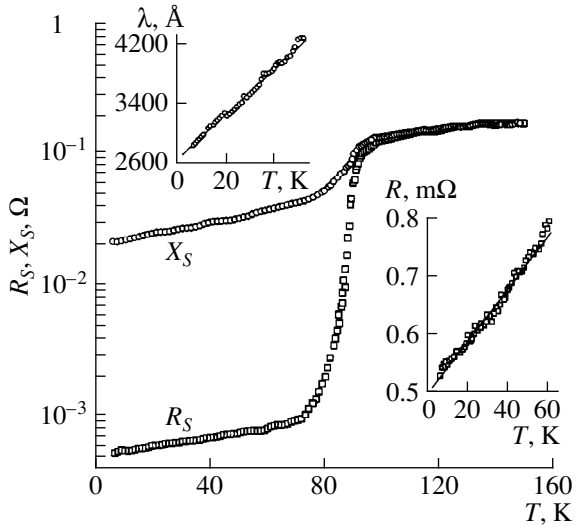

Fig. 2. Surface resistance $R_s(T)$ and reactance $X_s(T)$ in *ab*-plane (T-orientation) of sample #1 at 9.4 GHz. The insets show linear plots of $\lambda(T)$ and $R_s(T)$ at low temperatures.

parameters of sample #1 indicate that its quality is fairly high. In the T-orientation, linear functions $R_s(T)$ and $\Delta\lambda_{ab}(T)$ in the low-temperature range were previously observed in optimally doped BSCCO crystals at a frequency of about 10 GHz [7, 8, 14]. In the slightly overdoped sample #2 we also observed $\Delta\lambda_{ab}(T)$, $\Delta R_s(T) \propto T$ at low temperature, moreover, the measurement $R_{res} \approx 120\ \mu\Omega$ is, to the best of our knowledge, the lowest value ever obtained in BSCCO single crystals.

In both superconducting and normal states of HTS, the relation between electric field and current density is local: $j = \hat{\sigma}E$, where the conductivity $\hat{\sigma}$ is a tensor characterized by components σ_{ab} and σ_c. In the normal state, ac field penetrates in the direction of the *c*-axis through the skin depth $\delta_{ab} = \sqrt{2/\omega\mu_0\sigma_{ab}}$ and in the CuO_2 plane through $\delta_c = \sqrt{2/\omega\mu_0\sigma_c}$. In the superconducting state, all parameters δ_{ab}, δ_c, $\sigma_{ab} = \sigma'_{ab} - i\sigma''_{ab}$, and $\sigma_c = \sigma'_c - i\sigma''_c$ are complex. In the temperature range $T < T_c$, if $\sigma' \ll \sigma''$, the field penetration depths are given by the formulas $\lambda_{ab} = \sqrt{1/\omega\mu_0\sigma''_{ab}}$, $\lambda_c = \sqrt{1/\omega\mu_0\sigma''_c}$. In the close neighborhood of T_c, if $\sigma' \gtrsim \sigma''$, the decay of magnetic field in the superconductor is characterized by the functions $\mathrm{Re}(\delta_{ab})$ and $\mathrm{Re}(\delta_c)$, which turn to δ_{ab} and δ_c, respectively, at $T \geq T_c$.

In the L-orientation of BSCCO single crystals at $T < 0.9T_c$, the penetration depth is smaller than characteristic sample dimensions. If we neglect the anisotropy in the *ab*-plane and the contribution from *ac*-faces (see the inset to Fig. 1), which is a factor $\sim c/b$ smaller than that of the *ab*-surfaces, the effective impedance Z_s^{ab+c} in the L-orientation can be expressed in terms of Z_s^{ab} and Z_s^c averaged over the surface area [1, 5] (the superscripts of Z_s denote the direction of the screening current). Thus, given measurements of $\Delta\lambda_{ab}(T) = \Delta X_s^{ab}(T)/\omega\mu_0$ in the T-orientation and of the effective value $\Delta\lambda_{ab+c}(T) = \Delta X_s^{ab+c}(T)/\omega\mu_0$ in the L-orientation, we obtain

$$\Delta\lambda_c = [(a+c)\Delta\lambda_{ab+c} - a\Delta\lambda_{ab}]/c. \qquad (2)$$

This technique for determination of $\Delta\lambda_c(T)$ was used in microwave experiments [3–9] at low temperatures, $T < T_c$. Even so, this cannot be applied to the range of higher temperatures because the size effect plays an important role. Really, at $T > 0.9T_c$ the lengths λ_c and δ_c are comparable to the sample dimensions. In order to analyze our measurements in both superconducting and normal states of BSCCO, we used formulas [15] for field distributions in an anisotropic long strip ($b \gg a, c$) in the L-orientation. These formulas neglect the effect of *ac*-faces of the crystal, but take account of the size effect. In addition, in a sample shaped as a long strip, there is a simple relation between its surface impedance components and *ac*-susceptibility, which is expressed in terms of parameter μ introduced in [15]:

$$\Delta(1/Q) - 2i\delta f/f = i\gamma\mu v/V, \quad \chi = -1 + \mu, \qquad (3)$$

where $\gamma = VH_0^2/[\int_V H_\omega^2\, dV] = 10.6$ is a constant characterizing our cavity [1]. At an arbitrary temperature, the complex parameter $\mu = \mu' - i\mu''$ is controlled by the components $\sigma_{ab}(T)$ and $\sigma_c(T)$ of the conductivity tensor:

$$\mu = \frac{8}{\pi^2}\sum_n \frac{1}{n^2}\left\{\frac{\tan(\alpha_n)}{\alpha_n} + \frac{\tan(\beta_n)}{\beta_n}\right\}, \qquad (4)$$

where the sum is performed over odd integers $n > 0$, and

$$\alpha_n^2 = -\frac{a^2}{\delta_c^2}\left(\frac{i}{2} + \frac{\pi^2}{4}\frac{\delta_{ab}^2}{c^2}n^2\right),$$

$$\beta_n^2 = -\frac{c^2}{\delta_{ab}^2}\left(\frac{i}{2} + \frac{\pi^2}{4}\frac{\delta_c^2}{a^2}n^2\right).$$

In the superconducting state at $T < 0.9T_c$ we find that $\lambda_{ab} \ll c$ and $\lambda_c \ll a$. In this case, we derive from (4) a simple expression for the real part of μ:

$$\mu' = 1 + \chi' = \frac{2\lambda_c}{a} + \frac{2\lambda_{ab}}{c}. \qquad (5)$$

One can easily check up in the range of low temperatures, the change in $\Delta\lambda_c(T)$ prescribed by (5) is identical to (2). Figure 3 shows measurements of $\Delta\lambda_c(T)$ in sample

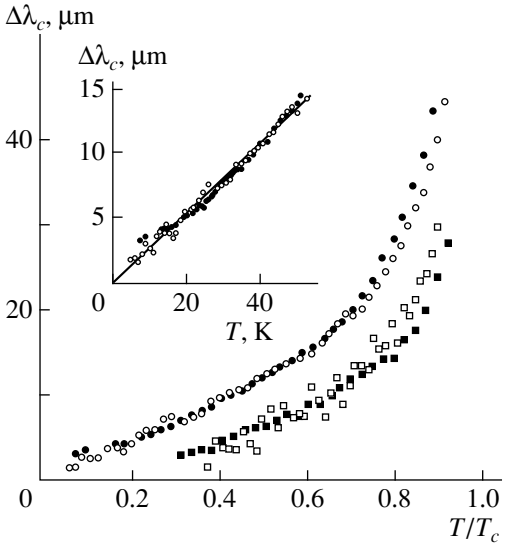

Fig. 3. Temperature dependences $\Delta\lambda_c$ in samples #1 (circles) and #2 (squares) at $T < 0.9\ T_c$. Open symbols plot low-frequency measurements, full symbols show microwave data. The inset shows low temperature sections of the $\Delta\lambda_c$ curves in sample #1.

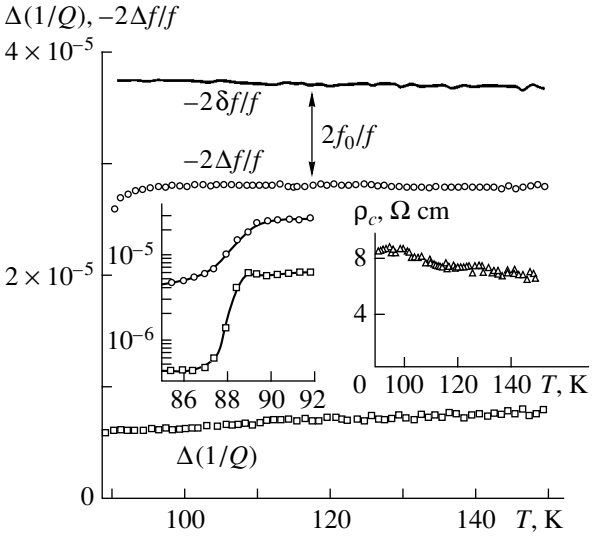

Fig. 4. Temperature dependences of $\Delta(1/Q)$ (open squares) and $-2\Delta f/f$ (open circles) in the L-orientation of sample #1 at $T > T_c$. Solid line shows the function $-2\delta f(T)/f$ deriving from (3). Left-hand inset: $\Delta(1/Q)$ and $-2\Delta f/f$ as functions of temperature in the neighborhood of T_c. Right-hand inset: $\rho_c(T)$ in sample #1 (triangles).

#1 (circles) and sample #2 (squares) at $T < 0.9T_c$. The open symbols plot low-frequency measurements obtained in accordance with (5), the full symbols plot microwave measurements processed by (2). Agreement between measurements of sample #2 (lower curve) is fairly good, but in fitting together experimental data from sample #1 (upper curve) we had to divide by a factor of 1.8 all $\Delta\lambda_c(T)$ derived from measurements of *ac*-susceptibility using (5). The cause of the difference between $\Delta\lambda_c(T)$ measured in sample #1 at different frequencies is not quite clear. We rule out a systematic experimental error that could be caused by misalignment of the sample with respect to the ac magnetic field because the curves of $\Delta\lambda_c(T)$ were accurately reproduced when square sample #1 was turned through an angle of 90° in the L-orientation. It seems more plausible that (2) and (5), which neglect the contribution of *ac*-faces, yield inaccurate results concerning sample #1: its *ac*-faces, which have a notable area (sample #1 is thick), can lose a lot of defects (for example hose of the capacitive type), and the latter can affect the character of field penetration as a function of frequency.

The curves of $\Delta\lambda_c(T)$ at $T < 0.5\ T_c$ plotted in Fig. 3 are almost linear $\Delta\lambda_c(T) \propto T$. The inset to Fig. 3 shows the low-temperature section of the curve of $\Delta\lambda_c(T)$ in sample #1. Its slope is 0.3 μm/K and equals that from [8]. Note also that changes in $\Delta\lambda_c(T)$ are smaller in the oxygen-overdoped sample #2 than in sample #1.

We can estimate $\lambda_c(0)$ by substituting in (1) $\delta f(0)$ obtained by comparing $\Delta(1/Q)$ and $\Delta f = \delta f - f_0$ measurements taken in the T- and L-orientations to numerical calculations by (3) and (4), which take into account the size effect in the high-frequency response of an anisotropic crystal. The procedure of comparison for sample #1 is illustrated by Fig. 4. Unlike the case of the T-orientation, the measured temperature dependence of $\Delta(1/Q)$ in the L-orientation deviates from $(-2\Delta f/f)$ owing to the size effect. Using the measurements of $R_s = \sqrt{\omega\mu_0/2\sigma_{ab}}$ at $T > T_c$ in the T-orientation (Fig. 2) for determination of $\sigma_{ab}(T)$, alongside the data on $\Delta(1/Q)$ in the L-orientation (open squares in Fig. 4), from (3) and (4) we obtain the curve of $\rho_c(T) = 1/\sigma_c(T)$ shown in the right-hand inset to Fig. 4. Further, using the functions $\sigma_c(T)$ and $\sigma_{ab}(T)$, we calculate $(-2\delta f/f)$ versus temperature for $T > T_c$, which is plotted by the solid line in Fig. 4. This line is approximately parallel to the experimental curve of $-2\Delta f/f$ in the L-orientation (open circles in Fig. 4). The difference $-2(\delta f - \Delta f)/f$ yields the additive constant f_0. Given f_0 and $\Delta f(T)$ measured in the range $T < T_c$, we also obtain $\delta f(T)$ in the superconducting state in the L-orientation. As a result, with due account of $\lambda_{ab}(T)$ (the inset to Fig. 2), we derive from (3) and (5) $\lambda_c(0)$, which equals approximately 150 μm in sample #1. A similar procedure performed with sample #2 yields $\lambda_c(0) \approx 50$ μm, which is in agreement with our measurements of overdoped BSCCO obtained using a different technique [12]. We also estimated $\lambda_c(0)$ on the base of absolute measurements of the susceptibility $\chi_c'(0)$ from (5), and we obtained $\lambda_c(0) \approx 210$ μm for sample #1 and $\lambda_c(0) \approx 70$ μm for sample #2. These results are in reasonable agreement with our microwave measurements if we take into

consideration the fact that the accuracy of λ_c measurements is rather poor and the error can be up to 30%.

In conclusion, we have used the *ac*-susceptibility and cavity perturbation techniques in studying anisotropic high frequency properties of BSCCO single crystals. We have observed almost linear dependences $\Delta\lambda_c(T) \propto T$, which are in fair agreement with both experimental [7, 8, 12] and theoretical [16] results by other researchers. We have also investigated a new technique for determination of $\lambda_c(0)$, which is a factor of three higher in the optimally doped BSCCO sample than in the overdoped crystal. The ratio between the slopes of curves of $\Delta\lambda_c(T)$ in the range $T \ll T_c$ is the same. These facts could be put down to dependences of $\lambda_c(0)$ and $\Delta\lambda_c(T)$ on the oxygen content in these samples. At the same time, we cannot rule out the influence of defects in the samples on $\lambda_c(0)$, even though their quality in the *ab*-plane is fairly high, according to our experiments. In order to draw ultimate conclusions concerning the nature of the transport properties along the *c*-axis in BSCCO single crystals, studies of more samples with various oxygen contents are needed.

ACKNOWLEDGMENTS

We would like to thank V.F. Gantmakher for his helpful discussions. This research was supported by grant no. 4985 of the CNRS-RAS cooperation. The work at ISSP was also supported by the Russian Foundation for Basic Research, grants nos. 97-02-16836 and 98-02-16636 and the Scientific Council on Superconductivity, project no. 96060.

REFERENCES

1. M. R. Trunin, Phys.-Usp. **41**, 843 (1998); J. Supercond. **11**, 381 (1998).
2. D. J. Scalapino, Phys. Rep. **250**, 329 (1995).
3. T. Shibauchi, H. Kitano, K. Uchinokura, *et al.*, Phys. Rev. Lett. **72**, 2263 (1994).
4. J. Mao, D. H. Wu, J. L. Peng, *et al.*, Phys. Rev. B **51**, 3316 (1995).
5. H. Kitano, T. Shibauchi, K. Uchinokura, *et al.*, Phys. Rev. B **51**, 1401 (1995).
6. D. A. Bonn, S. Kamal, K. Zhang, *et al.*, J. Phys. Chem. Solids **56**, 1941 (1995).
7. T. Jacobs, S. Sridhar, Q. Li, *et al.*, Phys. Rev. Lett. **75**, 4516 (1995).
8. T. Shibauchi, N. Katase, T. Tamegai, *et al.*, Physica C **264**, 227 (1996).
9. H. Srikanth, Z. Zhai, S. Sridhar, *et al.*, J. Phys. Chem. Solids **59**, 2105 (1998).
10. H. Kitano, T. Hanaguri, and A. Maeda, Phys. Rev. B **57**, 10946 (1998).
11. A. Hosseini, S. Kamal, D. A. Bonn, *et al.*, Phys. Rev. Lett. **81**, 1298 (1998).
12. H. Enríquez, N. Bontemps, A. A. Zhukov, *et al.*, submitted to Phys. Rev. B.
13. S. Ooi, T. Shibauchi, and T. Tamegai, Physica C **302**, 339 (1998).
14. S.-F. Lee, D. C. Morgan, R. J. Ormeno, *et al.*, Phys. Rev. Lett. **77**, 735 (1996).
15. C. E. Gough and N. J. Exon, Phys. Rev. B **50**, 488 (1994).
16. R. A. Klemm and S. H. Liu, Phys. Rev. Lett. **74**, 2343 (1995); T. Xiang and J. M. Wheatley, Phys. Rev. Lett. **76**, 134 (1996); R. J. Radtke, V. N. Kostur, and K. Levin, Phys. Rev. B **53**, R522 (1996).